Université des Sciences et Technologies de Lille

Laboratoire de Mécanique de Lille (UMR CNRS 8107)

Ecole Doctorale régionale Sciences Pour l'Ingénieur Lille Nord-de-France

Année 2009 - N° d'ordre : 40176

THESE

Pour obtenir le grade de

Docteur de l'Université des Sciences et Technologies de Lille

Discipline : Génie Civil

Présentée et soutenue publiquement par

Dawei HU

le 09 Décembre 2009

Contribution à l'étude du comportement mécanique et hydromécanique d'une roche endommagée

JURY

M. Hui ZHOU, Institut de Mécanique des Roches et des Sols, Chine	**Président**
M. Dariusz LYDZBA, Professeur, Université de technologie de Wroclaw, Pologne	**Rapporteur**
M. Dashnor HOXHA, Professeur, Université d'Orléons	**Rapporteur**
M. Qizhi ZHU, Laboratoire de Mécanique de Lille, Lille	**Invité**
M. Jianfu SHAO, Professeur, Polytech'Lille-USTL	**Directeur de Thèse**

Remerciements

Je souhaite tout d'abord à remercier monsieur le professeur Jianfu SHAO pour avoir bien voulu m'accepter d'être son thésard au sein de son équipe de recherche au Laboratoire de Mécanique de Lille et avoir me conseils très précieux qui ont été indispensables dans la réussite de ce mémoire. Sa compétence éminent et sa disponibilité sans limite m'ont encouragée permanent, tout au long de l'étude de thésard, à surmonter les obstacles.

Monsieur Hui ZHOU m'a fait l'honneur de présider mon jury. Qu'il trouve ici l'expression de toute ma gratitude. Messieurs Dariusz LYDZBA et Dashnor HOXHA ont accepté la tache ardue d'être rapporteurs de ce travail. Je les en remercie sincèrement. Je remercie tout autant Monsieur Qizhi ZHU pour avoir pris part au jury en tant qu'examinateurs.

J'adresse tous mes remerciements à tous mes collèges et amis de l'équipe ER4 du Laboratoire de Mécanique de Lille et de l'Institut de Mécanique des Roches et des sols à Wuhan pour son soutien moral et matériel qui m'a permis de mener à bien ce travail.

Ce travail a été réalisé avec l'aide financière de la fondation de science naturelle de la Chine (N° : 50579091, 10772190) et le ministère étranger de la France, je l'en remercie vivement.

Enfin, je remercie mes parents et mon épouse pour leur patience, leur aide et leur soutien sans faille qu'ils m'ont apportés tout au long de ces années de thèse. J'ai une pensée affectueuse pour eux et pour notre enfant.

Contents

Résumé

L'étude des comportements mécanique et poromécanique de grès intéresse de nombreux domaines d'activités, tel que les centrales hydrauliques, les stockages des déchets radioactifs, les forages pétroliers et les cavités minières. En premier lieu, la création des structures entraîne une décharge hydraulique et mécanique instantanée (caractérisée par une chute des pressions d'eau et de la contrainte radiale) dans le milieu géologique autour de la cavité. Le déchargement se propage pendant la phase d'exploitation autour des ouvrages maintenus ouverts et peut créer des microfissures en paroi de l'ouvrage. En revanche, le comportement poromécanique de la roche peut être influencé par les microfissures, tel qu'une variation locale de la perméabilité (Zhu and Wong, 1997a; Suzuki et al, 1998; Schulze et al, 2001; Souley et al, 2001; Bossart et al, 2002; Wang and Park, 2002; Oda et al, 2002; Shao et al, 2005) et le coefficient de Biot (Brace et al, 1968b; Dropek et al, 1978; Green and Wang, 1986; Fabre and Gustkiewicz, 1997; Hart and Wang, 2001; Lion et al, 2004; Trautwein and Huenges, 2005; Ghabezloo, 2009; just to mention a few). Notons que les microfissures se développent généralement de façon prédominante suivant une direction principale. L'anisotropie des microfissures conditionne largement les propriétés poromécaniques globales. Une littérature abondante a permis de comprendre l'évolution du développement progressif de la microfissuration et son rôle déterminant sur le comportement fragile d'une roche (Tapponier and Brace, 1976; Wong, 1982; Moore and Lockner, 1995; Wong et al, 1997; Baud et al, 1999). Cependant, ces études antérieures sont concentrées essentiellement sur le comportement mécaniques des roches. Les études sur l'anisotropie du comportement poromécanique et des propriétés de transfert des roches semi-fragiles sont très limitées. De ce fait, cette thèse est consacrée aux études expérimentales et numériques du comportement mécanique et poromécanique et de l'évolution de perméabilité du grès en prenant en compte l'anisotropie du matériau. La rédaction de ce mémoire s'organise autour de 5 chapitres dont nous introduisons ici le contenu.

Le chapitre I concerne l'étude bibliographique. En se basant des études

expérimentales réalisées par les différentes chercheurs, le comportement mécanique et poromécanique du matériau est d'abords présenté, ainsi que les méthodes expérimentales utilisées. Un intérêt particulier est mis sur l'influence de l'eau interstitielle, l'évolution de perméabilité et des coefficients de Biot du matériau. Ensuite, un résumé bibliographique sur les modèles de comportement élasto-plastique couplé à l'endommagement est exposé. L'accent est mis sur l'anisotropie du comportement et le comportement poromécanique du matériau formulation dans le cadre de théorie de Biot.

L'étude expérimentale fait l'objet du deuxième chapitre. Cette partie a pour objectif de présenter le comportement mécanique ainsi que son comportement poromécanique du grès, tel que l'évolution de coefficients de Biot et de la perméabilité. Après une analyse par microscopie électronique à balayage (MEB), l'organisation structurale de la matière est décrite au moyen d'expérience des rayons X. on remarque qu'une légère anisotropie structurelle est mise en évidence en raison de co-existence des litages parallèles et des microfissures initiales. Ensuite, les échantillons sont utilisés pour réaliser des essais de compression hydrostatique sous différentes pressions de confinement et de compression triaxiale. Sous les contraintes de compression hydrostatique, ces fissures peuvent être progressivement fermées en conduisant à une non-linéarité de la courbe de contrainte-déformation. Par contre, sous contrainte déviatorique, il y a une propagation des microfissures existantes et une nucléation des nouveaux microfissures quand le chargement dépasse un certain seuil. Les microfissures se développent de façon prédominante dans la direction parallèle à la contrainte compressive principale majeure, soit suivant la déformation axiale. Les évolutions des coefficients de Biot dans la direction radiale et axiale sont mesurées respectivement par une série de chemins de chargement sous différentes pressions de confinement. Afin d'étudier l'influence de l'état de contrainte sur l'évolution de la perméabilité, les valeurs de perméabilité sont mesurées sur des essais de compression triaxiales avec cycles de charges-décharges réalisés à différentes pressions de confinement. Une anisotropie dégradation des propriétés élastiques est mise en évidence ainsi que la variation anisotropique de coefficients de Biot et de la perméabilité intrinsèque. Au cours des essais, une transition du comportement fragile au comportement ductile et également une transition da la phase contractante à la phase dilatante est observée. Il existe quelque corrélation entre la perméabilité et les

déformations volumiques ainsi que la contrainte moyenne. Cependant, l'influence de la dilatance volumique sur l'augmentation de perméabilité n'est pas significative dans le régime de diffusion d'endommagement, soit avant le pic des courbes contraintes-déformations. Il semble que l'endommagement induit affecte la perméabilité d'une manière significative seulement après la coalescence des microfissures. Ce phénomène devrait être vérifié par les futures études.

Dans le troisième chapitre, en se basant sur les études antérieures et en tenant compte des données expérimentales, nous proposons une approche thermodynamique discrète pour les modèles elasto-plastiques couplés à l'endommagement. L'idée de base est d'étendre la formulation largement utilisée pour la modélisation du couplage de la plasticité et l'endommagement isotrope au cas de l'anisotropie induite. La déformation plastique totale est considérée comme la conséquence du glissement le long des surfaces des plans de faiblesse, qui sont distribués aléatoirement dans la matrice solide élastique. Les propriétés élastiques effectives du matériau endommagé sont déterminées en fonction de l'endommagement lié à l'évolution des plans de faiblesse. Dans la fonction de charge et le potentiel plastique, deux contraintes invariantes et une variable d'écrouissage plastique sont introduites pour chaque famille de plans de faiblesse. L'écoulement plastique dans chaque orientation est couplé avec l'endommagement correspondant. En conséquence, une version spécifique de ce model est proposée et appliquée aux grés secs, la fonction de charge et le potentiel plastique de type Coulomb tandis que le critère d'endommagement proposé par Mazars, est utilisé pour chaque famille des plans de faiblesse. En utilisant le modèle proposé, les essais en compression sont simulés. L'évolution et distribution de variable d'endommagement et de l'écrouissage plastique sont analysées. Une très bonne concordance est obtenue entre les prédictions et les données expérimentales. Ce modèle est donc capable de décrire les mécanismes principaux observés dans la plupart des roches fragiles sous contrainte compressive.

Dans le quatrième chapitre, le modèle proposé dans le chapitre précédent sera validé de nouveau par les simulations des essais réalisés sur des échantillons saturés. L'accent est mis sur l'influence de l'état hydrique sur le comportement mécanique ainsi que sur l'évolution de coefficients de Biot et la variation de la perméabilité intrinsèque. Des essais de compression triaxiale sont d'abords simulés. Une bonne concordance est

également observée. En conclusion, le modèle proposé est capable de décrire la non linéarité de courbe de contrainte-déformation, la transition contraction-dilatance, le changement de comportement (de fragile à ductile) avec l'augmentation de confinement, la dégradation des propriétés élastiques et l'anisotropie induite. Ensuite, un modèle micromécanique est introduite pour décrire l'anisotropie des coefficients de Biot. Les coefficients de Biot sont donc formulés en fonction des tenseurs effectifs de rigidité et du module de compressibilité de la matrice solide. Les comparaisons entre les simulations numériques et les résultats d'essai nous permettent de conclure que le modèle proposé est capable de décrire correctement l'évolution des coefficients de Biot dans les directions axiale et radiale. Concernant la perméabilité, la perméabilité axiale est séparée en deux parties dans le modèle numérique : la perméabilité de matrice et la perméabilité à cause des microfissures. Le premier terme étant défini par une relation empirique liée à la contrainte moyenne. Par ailleurs, le deuxième dépend de l'orientation, de l'ouverture et de la déformation normale des fissures. L'évolution de la perméabilité axiale est simulée pendant l'essai triaxial sous différentes confinements. On obtient encore une fois une bonne concordance entre les simulations numériques et les données expérimentales.

En se basant sur les travaux antérieurs de modèle discret couplé et la modélisation des coefficients de Biot, on développe un modèle anisotropie poroplastique couplé avec l'endommagement afin de décrire les propriétés poromécaniques du grès saturé dans le cinquième chapitre. On propose une surface de charge améliorée et un potentiel plastique sur chaque groupe des plans de faiblesse glissant en utilisant la conception des contraintes équivalentes. Une variable de porosité plastique, fonction linéaire des déformations volumiques plastiques, est introduite dans le cadre de théorie de la poroélasticité de Biot. Le modèle proposé est appliqué au grès de Vosges pour décrire le comportement du matériau dans les essais triaxiaux en condition non-drainée, y compris des essais triaxiaux en appliquant une pression de liquide. En général, un très bon accord est obtenu entre les prédictions et les données expérimentales. On peut conclure que ce modèle est capable de décrire l'évolution de pression interstitielle et de l'écrouissage dans la phase dilatante (dilatance hardening), ainsi que l'anisotropie des déformations accentuée par l'évolution de pression interstitielle.

Abstract

This thesis presents the laboratory and numerical investigations on anisotropic mechanical, poromechanical and fluid transport behavior of sandstone.

A literature review is first presented including the experimental studies and modeling on mechanical behaviour, poromechanical behaviour and fluid transport properties of brittle geomaterial.

After the X-ray and SEM tests, the samples were stressed under triaxial loading to study the initial and stress-induced mechanical behavior. Effective Biot's coefficients in axial and lateral directions are measured at different stress (damage) level to explore the evolution of Biot's coefficients, the permeability in axial direction are measured in triaxial compression tests with cyclic loading. The evolution of anisotropic Biot's coefficients and axial permeability are discussed related to mechanical behavior.

A plastic damage model is presented based on discrete approach. The modified Coulomb-type plastic yield and plastic potential function, and damage evolution criterion proposed by Mazars are given for each family of weakness planes. The proposed model is applied to simulate the mechanical behavior of dry sandstone under different loading conditions, the evolution and distribution of damage variable and plastic hardening variable are also discussed.

The proposed model is applied to simulate the previous experimental results of saturated sandstones. After the modelling of mechanical behaviour in triaxial compression, the relation of Boit's coefficients is introduced following the micromechanical analysis, the axial permeability is divided into two parts: matrix permeability and permeability induced by cracks. The comparisons between the numerical result and test data show a good performance of the present model.

An anisotropic poroplastic damage model is developed to describe the poromechanical behavior of saturated sandstone. The modified plastic yield and potential functions are presented for each family of weakness sliding planes with the help of equivalent stress concept, and the constitutive equations of coupling system is set up base on Biot's theory, the plastic porosity is introduced and related to volume plastic strain. The comparisons between numerical simulation and experimental data is given for the triaxial compression tests under draind and undrained condition, the tests of strain response to pore pressure increment is also simulated, a good accordance is obtained.

General introduction

In stability and durability analysis on underground engineering structures such as geological storage of nuclear wastes, sequestration of carbon and residual gas, oil and gas production and so on, where geomaterials serve as host formation, it is crucial to understand in depth multi-physical coupling mechanisms involved by means of both laboratory tests and numerical methods. On this topic, various research works have been carried out, among which two different approaches were widely adopted, that is, the mixture theories and the poromechanical theory. For the former, porous media are described by spatially superimposed interacting components while the latter, mainly based on the work by Biot (1941, 1955), assumes that the standard concepts of continuum mechanics are still relevant at macroscopic scale for porous media. In practical applications, the poromechanical theory is most often applied for its facility.

One of the essential tasks in these works consists in the determination of multi-physical properties, such as the Biot's coefficients, which is the main parameter in the poroelasticity theory (Biot, 1941, 1955), and rock permeability, which is strongly dependent on applied stress and subsequent rock deformation. Various experimental investigations have been so far reported on their determination in different rocks (Brace et al, 1968b; Dropek et al, 1978; Green and Wang, 1986; Fabre and Gustkiewicz, 1997; Hart and Wang, 2001; Lion et al, 2004; Trautwein and Huenges, 2005; Ghabezloo, 2009; just to mention a few) and on the validation and application of the concept of *effective stress* for poroelastic modeling (Brace, 1968a; Carrol, 1979). However, the great majority of these contributions have focused on the study of poroelastic and flow properties of rocks in their initial (undamaged) state and under hydrostatic stress. It is now known from observations in situ and experiments at laboratory that most brittle rocks (sandstone, limestone, granite, etc.) exhibit deviatoric stress induced anisotropy due to nucleation and propagation of microcracks in some preferential orientations (Tapponier and Brace, 1976; Wong, 1982; Moore and Lockner, 1995; Wong et al, 1997; Baud et al, 1999) which from mechanical viewpoints, is commonly characterized by the theory of the continuum

damage mechanics. The main consequences of the induced anisotropic damage include non linear stress-strain relations, anisotropic degradation of elastic properties, anisotropic variation in multi-physical properties, such as permeability, diffusivity, fluid transport through pore network and so on (Ismail and Murrell, 1976; Steif, 1984; Horii and Nemat-Nasser, 1985; Fredrich et al, 1989; Schmitt and Zoback, 1992; Olsson, 1995; Shao and Rudnicki, 2000). Evaluation of permeability during rock cracking has also been performed by many authors, for instance, Zhu and Wong, 1997a; Suzuki et al, 1998; Schulze et al, 2001; Souley et al, 2001; Bossart et al, 2002; Wang and Park, 2002; Oda et al, 2002; Shao et al, 2005. These works have clearly shown that the evolutions of poroelastic properties are directly related to the distribution, opening and coalescence of induced microcracks.

Based on experimental investigations, some coupled poromechanical modelling has been developed for saturated rocks. Recent progresses have been achieved in completing and generalizing the pioneer theory of Biot particularly for anisotropic porous media (Biot, 1941, 1955; Detournay and Cheng, 1998; Coussy, 1995; Carrol, 1979). Reformulation of the equations of anisotropic poroelasticity was proposed by Thompson and Willis (1991) where the relationships between macroscopic poroelastic constants and the properties of porous medium constituents have been established. To better elucidate the physical meaning of poroelastic constants, Cheng (1997) proposed a comprehensive methodology for the determination of anisotropic poroelastic constants from easily realizable laboratory tests. Analytical and numerical solutions using anisotropic poroelasticity have also been proposed by Abousleiman et al. (1996) and Cui et al. (1996) for modelling of the generalized Mandel's problem and of an inclined borehole problem. Shao (1997, 2004) proposed a poroelastic model with anisotropic damage for describing the evolution of poroelastic behaviour under drained, undrained triaxial and pore pressure controlled tests. The fluid transport in interstitial space is described by the well-known Darcy's law, among which rock permeability is often determined by the empirical method related to stress, volume strain and porosity from experimental result (Carman, 1956; Paterson, 1983; Berryman and Blair, 1987; David et al, 1994; Zhu and Wong, 1997).

In summary, existing research works have mainly focused upon poroelastic behaviors

and the variation in multi-physical properties. However, brittle geomaterials in underground settings may suffer significant inelastic deformation in compression regime, particularly induced by frictional sliding on the surfaces of cracks on micro- and meso-scales (Halm and Dragon, 1998; Pensée et al., 2002; Dormieux et al., 2006; Zhu et al., 2008) and by slipping faults on structural scale (Wong, 1982). Therefore, the commonly-used poroelastic framework becomes insufficient any more and thus the current mathematical framework has to be adapted for proper description of this poroplastic damage coupling process. The main objective of the present work aims to fill up this research vacancy. Focus is mainly cast upon the experimental and numerical study of coupled anisotropic plastic damage behaviours and of the influence of induced anisotropic damage by microcracks on the evolution of poromechanical behavior and fluid transport properties. To attain this goal, the mechanical response, the evolution of Biot's coefficients and the variation of rock permeability of sandstone are studied by different loading paths in triaxial compression tests, a coupled poroplastic damage model is developed within the discrete thermodynamic approach (Zhu et el. 2008c) for modelling anisotropic plastic deformation and damage evolution in sandstones, dry or saturated, under both drained and undrained conditions. This Ph.D. thesis is structured as follows:

In chapter 1, we give a bibliographic summary of previous works on mechanical and poromechanical behaviours of brittle geomaterials. After the introduction of porous media, the experimental studies on the brittle geomaterials are reviewed. Finally, the modelling of mechanical and poromechanical behaviours is summarized.

The mechanical behaviours, determination of the Biot's coefficients and intrinsic permeability of sandstone with induced anisotropic damage in saturated conditions are presented in Chapter 2. In the X-ray and SEM tests, the samples are stressed under triaxial loading to study the initial and stress-induced mechanical behavior. Hydrostatic compression tests and a series of triaxial tests with different confining pressures are performed.

In Chapter 3, an anisotropic plastic damage model is developed within the discrete thermodynamic framework. Macroscopic plastic strains of material are assumed to be

physically generated by frictional sliding along weakness planes. The evolution of damage is related to growth of weakness planes physically in connection with propagation of microcracks. Plastic flow in each orientation is coupled with damage evolution. The modified Coulomb-type plastic yield and plastic potential function, and damage evolution criterion proposed by Mazars are given for each family of weakness planes. The mechanical behavior under compressive loading are simulated, the evolution and distribution of damage variable and plastic hardening variable are discussed.

In Chapter 4, the basic model is applied to simulate the experimental results of saturated sandstones including mechanical behaviour, Boit's coefficients and permeability. In permeability characterization, rock permeability is divided into matrix permeability and permeability induced by crack, an empirical relationship between matrix permeability and mean stress is introduced to describe the former term, the latter one is regarded as a function of the crack orientation, crack radius and normal strain, which can be easily obtained from the mechanical model.

An anisotropic poroplastic damage model is developed in Chapter 5 to describe the poromechanical behavior of saturated sandstone. A modified plastic yield and potential functions are formulated for each family of weakness sliding planes in the context of the *equivalent stress concept* and the constitutive equations of coupling system is set up base on Biot's theory. The complementary variable of plastic porosity is introduced and related to volume plastic strain. This model is applied to Vosges sandstone to describe the undrained compression tests and strain response to pore pressure increment.

Chapter 1 Fundamentals of mechanical and poromechanical modelling in geomaterials

In the first chapter, we will give a bibliographic summary of previous works on mechanical and poromechanical behaviours of brittle geomaterials. After an introductive description of porous media, experimental investigations on brittle geomaterials are reviewed on three aspects: mechanical behaviours under stress loading, evolution in permeability and in Biot's coefficients, and effects of pore fluid on mechanical response. Finally, some fundamental formulations for mechanical and poromechanical modelling will be presented. For the former, focus is cast on anisotropic plastic damage behaviors. Constitutive equations for modelling poromechanical behavior will be formulated within the framework of the Biot's theory of porous media.

1.1 Description of porous media

Brittle geomaterials, generally regarded as a kind of porous media, are composed of a matrix phase and some porous space (see Fig. 1.1); the latter is often filled by fluid in underground setting. The matrix phase consists of a solid part and some occluded pores, through which no filtration occurs, whether saturated or not (Coussy, 2004). The connected porous space is the one through which the fluid can flow freely and any two points inside which can be joined by a path lying entirely within it so that the fluid phase remains continuous therein. Correspondingly, the connected porosity is defined as the ratio of the volume of the connected porous space to the total volume.

Based on laboratory investigations, two essential mechanisms, which may play a key role in the interaction between the interstitial fluid and the porous media where it is present, can be identified, (a) elastic and inelastic material deformation under stress loading, leading to linear and more often nonlinear mechanical behaviors and usually bringing some evolution in material microstructure (e.g. size, density and spatial

distribution of microcracks) and finally in multiphysical properties, such as permeability, diffusivity, fluid transport through pore network and so on; (b) existence of interstitial fluid in porous geomaterials, which modifies mechanical responses of the latter; for example, the strength of geomaterials is usually higher under dry condition than saturated one; another example consists that geomaterials behave more compliant under drained condition (when excess pore pressure is completely dissipated) than undrained one (when the fluid cannot escape from the porous rock). In fact, these two mechanisms are generally coupled each other in underground engineering, such as water power station, nuclear waste disposal industry, carbon dioxide sequestration process, petrol industry, rock mining and so on.

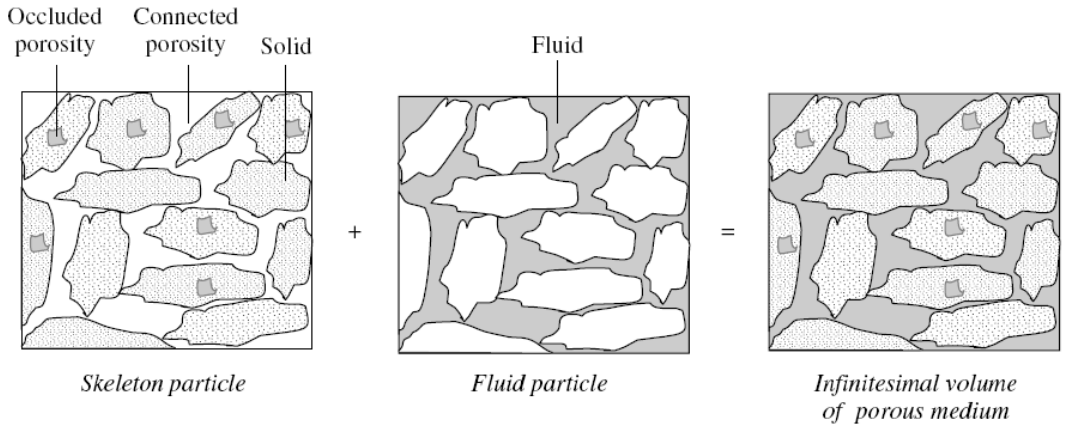

Fig. 1.1 *Structure of porous material (Coussy, 2004)*

1.2 Experimental studies on brittle geomaterials

In multiphysical context, brittle geomaterials such as concrete and some rocks generally exhibit coupled poromechanical behaviors. On the one hand, during failure process of material, the stress-induced deformation can change in significant way some poromechanical properties of material, such as elastic constants, Biot's coefficients, permeability, acoustic emission, elastic wave speed and others; on the other hand, the pore fluid can also influence material mechanical response. In this section, we will review some existing experimental works on the effects of stress on multiphysical properties and inversely the effect of pore fluid on mechanical behavior in geomaterials, based on which are formulated some constitutive modelings.

1.2.1 Mechanical behaviours

The mechanical behaviors of brittle rocks have been extensively investigated in laboratory. We are first concerned with the stress-strain curves obtained from a series of triaxial compression tests performed on Wombeyan marble under different confining pressures (Paterson, 1958). Fig.1.2 shows its typical stress-strain curves under increasing confining pressures. Some essential features common to brittle geomaterials are summarized below:

1) The mechanical behaviors are strongly dependent on confining pressures. For all levels of confinement, after a more or less linear phase, the stress-strain curves show significant nonlinear mechanical behaviors. It is obviously seen that the material strength or the peak stress increases with the confining pressure.
2) There is an increasing tendency on the stress-strain curves of continuously rising up to large strains with greater slope, that is, there is a greater extent and degree of strain-hardening at higher pressures.
3) A brittle-ductile transition occurs with the increase of confining pressures. At low confining pressures, brittle behaviors with a sharp drop on the stress-strain curves are observed just after the peak-stress while at high confining pressures ductile behaviors without stress softening are captured.

Crack patterns

Four types of crack configuration can be identified in Wombeyan marble tested under increasing confining pressure as shown in Fig.1.3: (a) splitting crack along the axial stress in uniaxial compression test, (b) single shear crack when the extent of confining pressures is between 3MPa an 5MPa, (c) conjugate shear cracks at confining pressure of about 35MPa, (d) ductile behavior without occurrence of obvious main crack when confining pressures are beyond 70MPa.

Volumetric strain

The evolution in volumetric strain is another important phenomenon frequently involved in loading process. In triaxial compression tests under hydrostatic pressure or at low level of deviatoric stresses, the compaction (volumetric strain decrease due to the

closure of total or partial pre-existing cracks and pores) is often observed; however, with the increase of deviatoric stress, the development of volumetric strain gradually undergoes an increase instead of decrease, in other words, a compaction-dilatancy transition occurs during failure process. The volume dilatancy is regarded as one of important aspects in mechanical behaviors of geomaterials. In compression regime, this phenomenon is mainly due to the nucleation and growth of microcracks.

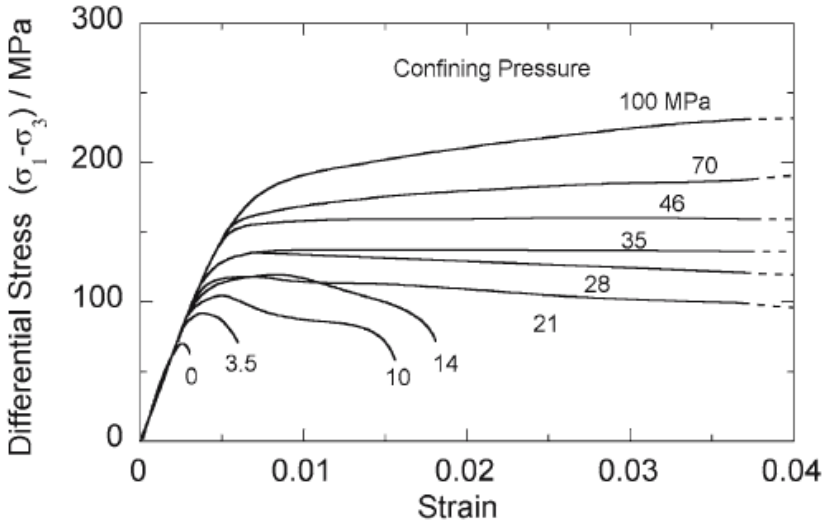

Fig. 1.2 *Stress-strain curves of Wombeyan marble in triaxial compression tests with different confining pressure (Paterson, 1958)*

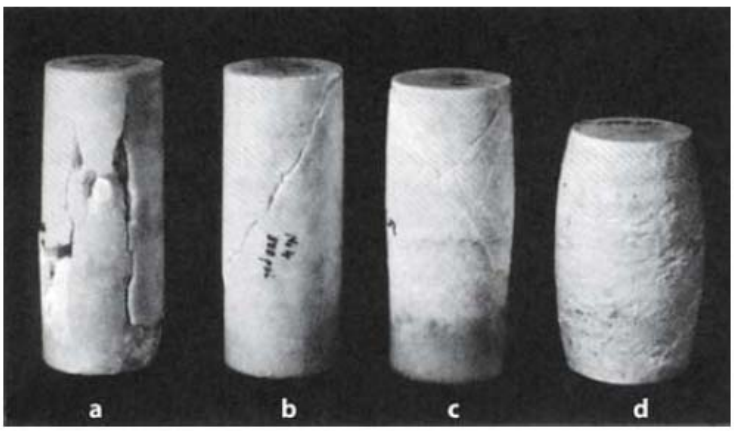

Fig. 1.3 *Fracture patterns in Wombeyan marble in triaxial compression tests with different confining pressure (Paterson, 1958)*

Material degradation by cracking

In brittle geomaterials, the propagation of microcracks generally leads to a progressive degradation in elastic stiffness. For clarity, let us look at a conventional triaxial compression test on argillite with some unloading-reloading cycles (see Fig.1.4). It is observed that elastic constants in both axial and lateral directions are gradually reduced after the onset of plastic yielding, this fact being manifested by progressive decrease in slope of the cycles. Moreover, the degradation of the material stiffness in the lateral direction is more important than that in the axial direction. This stress-induced anisotropy is predominantly attributed to preferred propagation of microcracks whose surfaces are inclined at small angles with respect to the axial loading direction.

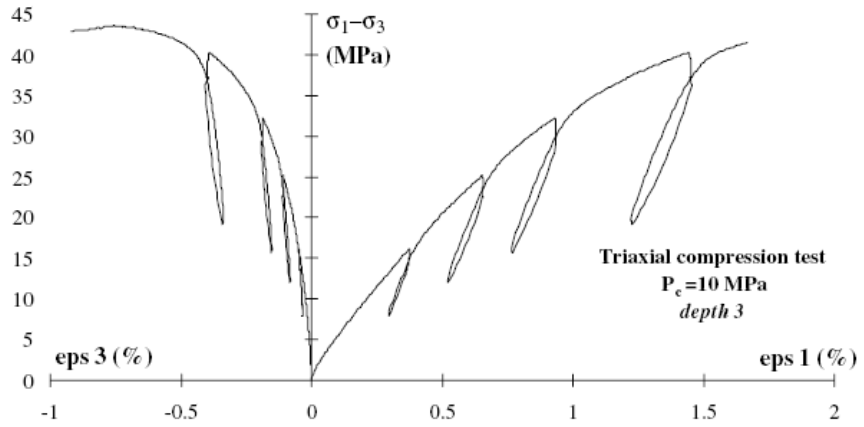

Fig. 1.4 *Stress-strain curves in a triaxial compression test with unloading-reloading cycles on argillite (Chiarelli et al., 2003)*

1.2.2 Evolution of Biot's coefficients and permeability

As aforementioned in Section 1.2, deformation of porous media can bring significant change upon multiphysical properties of material. Discusses are here addressed on the evolution of Biot's coefficients and permeability in saturated porous media subjected to stress loading.

Mechanical behaviour of porous geomaterials under compressive or shear stress, either elastic or inelastic, depends in general on both the state and history of applied stress and the pore pressure. In practice, for the sake of simplicity, an effective stress, denoted by $\tilde{\boldsymbol{\sigma}}$, is usually used in constitutive modelling, which is a nominal macroscopic stress determined by the measured total macroscopic Cauchy stress $\boldsymbol{\sigma}$ and the pore

pressure p, and practically treated as the stress variable (thermodynamic force) governing the mechanical response of the porous material under consideration. This viewpoint of effective stress is clearly set out by Skempton (1961), Robin (1973) and Berryman (1992) and is adopted in the present work.

Experimental observations show that the effective stress can be written in the form $\boldsymbol{\sigma} - \boldsymbol{b}p$, where $\boldsymbol{b}$ is called as the *Biot's coefficients*, which is a second order tensor depending on the pore geometry. In isotropic case, the tensor of Biot's coefficients reduces to a scalar b and the Tergazhi's effective stress law is recovered when the value of b is taken to be 1. For most geomaterials under stress loading, microcracks undergo successively the stages of nucleation, growth and coalescence, which can bring significant change in the Biot's coefficients. Therefore, the Biot's coefficients of damaged geomaterials are reasonably assumed function of the variables charactering microcracks, such as size, density, spatial distribution and so on (Cheng, 1997; Shao, 1998). In the present work, internal damage variables are used to achieve this goal. The detailed discussions on this point are presented later.

The fluid transport in interstitial space can be described by the well-known Darcy's law, which is an empirical equation originated for description of seepage flow in porous media and which can also be derived from Navier-Stokes equations by dropping the inertial terms (Bear, 1972). Consistent with the assumption of small deformation and by ignoring the fluid density variation effect (Hubert, 1940), the Darcy's law is here adopted without modification:

$$\underline{v} = -\frac{\boldsymbol{K}}{\mu} \cdot \nabla p, \tag{1.1}$$

where $\underline{v}$ is referred to as the filtration velocity vector, $\boldsymbol{K}$ denotes a second order tensor, describing intrinsic permeability and having the dimension of length squared and function of pore geometry, μ represents the dynamic fluid viscosity and ∇p a vector representing the hydraulic head gradient. In isotropic case, the above equation can be rewritten in the form

$$v = -\frac{K}{\mu}\frac{\Delta p}{\Delta h}, \tag{1.2}$$

where Δp is the difference of hydraulic head and Δh the height difference.

Experimental studies confirmed that deformations induced by stress can bring significant evolution in rock permeability. The relationship between stress-induced deformation and permeability evolution has been revealed by the following two frequent events: permeability reduces with material volumetric compaction (Gatto, 1984; Zhu and Wong, 1997a; Wang and Park, 2002) while augments with material volumetric dilatancy (Zoback and Byerlee, 1975; Stormont and Daemen, 1992; Zhang et al, 1994; Peach and Spiers, 1996; Suzuki et al, 1998; Schulze et al, 2001; Souly et al, 2001). More precisely, on the one hand, for highly porous rocks under compressive stress, the permeability deceases continuously with compaction induced by reduction in porosity; on the other hand, for moderately porous rocks, the permeability experiences a change from reduction to augmentation as the volume suffers a compaction-dilatancy transition.

1.2.3 Role of pore fluid

The previous parts focus mainly on the evolution of physical properties under mechanical loading. However, pore fluid also shows important impacts on the mechanical behaviour of geomaterials. For example, water content may influence considerably material strength and deformation extent, material hardening, chemical degradation and so on. Here, only the impact of pore pressure on mechanical response will be discussed.

In undrained compression tests, pore pressures can be substantially modified by changes in porosity during stress loading, which in reverse, influence the mechanical behaviour. A dilatancy in volume can then lead to a decrease of pore pressure in samples (Heck, 1972; Dropek et al, 1978; Green and Wang, 1986). Consequently, effective normal stress seems to increase from the viewpoint of effective stress law. This effect is known as the dilatancy hardening (Brace and Martin, 1968a; Rutter, 1972; Ismail and Murrell et al, 1976; Chiu et al, 1983; Rudnicki, 1985; Schmitt and Zoback, 1992; Paterson, 2005).

In laboratory, in order to make occurrence of material deformation by increasing pore pressure, saturated specimens are first subjected to a classic triaxial loading until a certain damage level is attained. Next, the pore pressure is increased progressively by injecting

water into the specimen with the total macroscopic stresses remained constant. In this process, the axial and lateral strains are recorded. Such tests provide great interest in investigating the effects of induced microcracks on poromechanical behaviour. A representative result concerning such tests is shown in Fig. 1.5 (Karami, 1998).

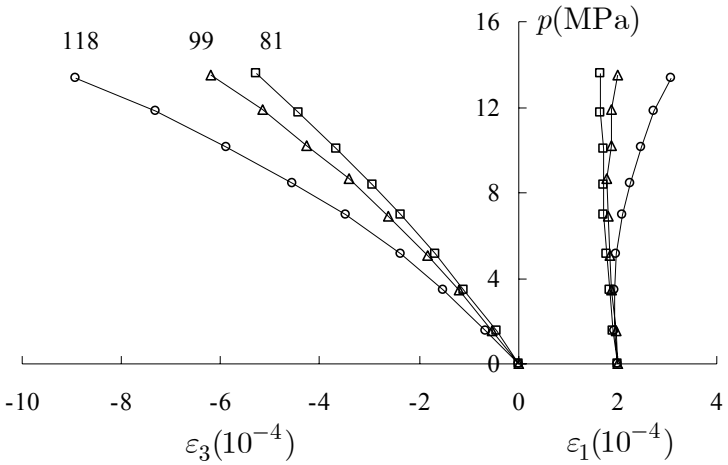

Fig. 1.5 *Strain responses to pore pressure increase at different deviatoric stress in triaxial compression tests with the same confining pressure of 40MPa (Karami, 1998)*

1.3 Constitutive modelling of geomaterials

In order to describe the mechanical and poromechanical behaviour of brittle geomaterials, various constitutive models have been proposed on the basis of the mechanisms revealed by laboratory investigations. In this section, a short review on previous works is presented.

1.3.1 Mechanical modelling

For most brittle geomaterials, such as concrete and some rocks, the nucleation, propagation and coalescence of microcracks in some preferential orientations are commonly observed in failure process. Microcracks growth could lead to anisotropic plastic deformation and damage evolution. As a consequence, these geomaterials exhibit stress-induced anisotropies. Optical microscope method has been largely used to trace the evolution of microcracks (crack size and distribution in space) as well as the formation of shear localization in a compact quartzite (Hallbauer et al., 1973). Further studies

(Tapponier and Brace, 1976) using the Scanning Electron Microscope (SEM) allow to observe crack growth in three-dimensional setting and finally make available the information of spatial geometric attributes and of stress-induced anisotropy. During failure process, when stress is increased to near the peak, stress-induced anisotropy becomes more important with some obvious degradation in elastic properties of material (Wong, 1985). After the peak, microcracks begin to be localized into a macroscopic shear band with significant plastic deformation (Wong, 1985; Moore and Lockner, 1995). It is commonly adopted that microcracks nucleation and growth in brittle geomaterials, often modelled in the framework of continuum damage mechanics, can enhance plastic flow while inversely plastic deformation in brittle geomaterials often plays a driving force for damage evolution. In summary, these two mechanisms usually couple each other.

Some phenomenological models have been developed for modelling aforementioned coupled plastic damage behaviour (Dragon and Mroz, 1979; Ju, 1989; Hayakawa and Murakami, 1997; Chiarelli et al., 2003; Shao et al., 2006 and others). The advantages of such models are such that they are formulated in the irreversible thermodynamics framework and provide macroscopic constitutive equations so that these models can be easily implemented for engineering applications. The obvious weakness consists in the fact that some concepts and parameters used are not clearly connected to physical mechanisms and that it is difficult for such models to avoid some difficulties in accounting for more complex phenomena involved in geomaterials, such as unilateral effects, interactions between different cracks families, poromechanical coupling in anisotropic state, and so on. On the other hand, from physical consideration, a number of micromechanical damage models are developed in order to describe these physical mechanisms involved in geomaterials (e.g. Kachanov, 1982; Gambarotta and Lagomarsino, 1993; Zhu et al., 2008a, 2008b, just to mention a few). In these models, the macroscopic effective quantities are obtained through a micro-macro up-scaling procedure. However, mathematical formulation of the micromechanics-based models developed so far is still limited in elastic regime. In the framework of linear homogenization, their extension to coupled plasticity-damage one is still quite difficult.

Finally, our eyes have to been cast onto another class of constitutive models. It

consists in formulating macroscopic constitutive models with consideration of physical mechanisms at microscopic scales. These models share the feature of orientation-dependence and could be cast back to the slip theory of plasticity for metal materials initiated by Taylor in 1938. This concept has then been applied to model mechanical behaviors of geomaterials. In soil mechanics, the multi-laminate concept was introduced for plastic/viscoplastic modelling of clays (Pande and Sharma, 1983). However, in these models, effects of damage related to growth of weakness planes have usually been neglected. For cement-based materials and rocks, Bazant and Oh (1985) proposed the microplane model and various extensions have been performed for specific applications (Carol and Bazant, 1997; Carol et al., 2001; Bazant and Zi, 2003 and others). Moreover, Chang and Hicher (2005) have proposed an elastoplastic model for granular materials with micro-structural considerations. The macroscopic behaviours of granular materials are obtained by averaging deformations in contact surfaces between grains, formally similar to the case of microcracks. More recently, Zhu et al. (2008c) proposed a discrete thermodynamic approach to model coupled anisotropic plastic damage behaviours in cohesive frictional geomaterials. In this model, macroscopic plastic strains of material are physically generated by frictional sliding along weakness planes, and the evolution of damage is related to growth of weakness planes physically in connection with propagation of microcracks. This model will be adopted and extended in this work to for modelling coupled anisotropic poromechanical behaviors in brittle geomaterials.

1.3.2 Poromechancial modelling

The above mentioned models only treat the mechanical behaviour of brittle materials. In this part, the poromechanical models based on Biot's theory are presented.

1.3.2.1 Fundamentals of linear poroelasticity

In order to investigate the failure process of geomaterials and to evaluate the stability of structure in underground engineering, it is obviously necessary to study the hydraulic-mechanical coupling system. Terzaghi (1923) initially developed the earliest theory to account for the influence of pore fluid on the quasi-static deformation in soils and to treat one-dimensional consolidation. This theory was then generalized to

three-dimensional case by Rendulic (1936). Biot (1935 and 1941) proposed the theory of linear poroelasticity, which is consistent with the two basic mechanisms outlined above. This theory has been reformulated by Biot himself (1962) and by Rice and Cleary (1976) to link the poroelastic parameters to concepts that are well understood in rock and soil mechanics. More recent works on this topic (Coussy, 1995 and 2004; Detournay and Cheng, 1993; Cheng, 1997) have been dedicated to complete and generalize the pioneer works of Biot, particularly for anisotropic porous media. Alternative theories have also been developed using the formalism of mixtures theory (Crochet and Naghdi, 1966; Morland, 1972; Atkin and Craine, 1976; Bowen, 1982; Katsube and Carroll, 1987). Coussy et al, (1998) established a link between Biot's theory and mixtures theory. However, in practice the latter does not offer any advantage over the Biot's theory. Therefore, in the following part, we present the Biot's theory based on the Biot's poroelasticity framework.

The porous media is seen as an open thermodynamic system exchanging fluid mass with the exterior domain. Limited to isothermal and small deformation cases, the state variables involved are strain tensor ε and fluid mass change per unit initial volume m. Considering a natural initial state (without pre-stress and pressure), the quadratic free energy function is:

$$\psi\left(\varepsilon,m\right)=g_m^0 m+\frac{1}{2}\varepsilon:\mathbb{C}:\varepsilon-M(\boldsymbol{b}:\varepsilon)\left(\frac{m}{\rho_f^0}\right)+\frac{1}{2}M\left(\frac{m}{\rho_f^0}\right)^2 \tag{1.3}$$

where g_m^0 is the specific free fluid enthalpy and ρ_f^0 the reference volumetric fluid mass, the fourth order tensor $\mathbb{C}$ denotes the elastic stiffness of the porous media in undrained state, $\boldsymbol{b}$ is the second order Biot's coefficients tensor and M is the scalar Biot's modulus. Standard derivative of (1.3) with respect to the state variables allows us to write the constitutive equations of linear poroelasticity as follows:

$$\boldsymbol{\sigma}=\mathbb{C}:\varepsilon-M\boldsymbol{b}\left(\frac{m}{\rho_f^0}\right) \tag{1.4}$$

$$\left(g_m - g_m^0\right) = -M\left(\boldsymbol{b} : \varepsilon\right)\left(\frac{1}{\rho_f^0}\right) + M\left(\frac{1}{\rho_f^0}\right)\left(\frac{m}{\rho_f^0}\right) \tag{1.5}$$

By making use of the state law of perfect fluid, (1.5) may be rewritten in the following form:

$$\left(g_m - g_m^0\right) = \frac{p - p_0}{\rho_f^0} \tag{1.6}$$

$$\left(p - p_0\right) = M\left[-\boldsymbol{b} : \varepsilon + \left(\frac{m}{\rho_f^0}\right)\right] \tag{1.7}$$

where p_0 denotes the initial pore pressure in the reference state of deformation. Substituting (1.7) in (1.4) leads to the constitutive relations of linear poroelasticity in drained conditions:

$$\boldsymbol{\sigma} = \mathbb{C}^b : \varepsilon - \boldsymbol{b}(p - p_0) \tag{1.8}$$

with

$$\mathbb{C}^b = \mathbb{C} - M(\boldsymbol{b} \otimes \boldsymbol{b}) \tag{1.9}$$

Above, $\mathbb{C}^b$ denotes the drained elastic stiffness tensor. According to the concept of effective stress, (1.8) may also be rewritten in the form

$$\tilde{\boldsymbol{\sigma}} = \mathbb{C}^b : \varepsilon \tag{1.10}$$

It follows

$$\tilde{\boldsymbol{\sigma}} = \boldsymbol{\sigma} + \boldsymbol{b}(p - p_0) \tag{1.11}$$

where the second order tensor $\tilde{\boldsymbol{\sigma}}$ is called as the *effective stress*, serving as the thermodynamic force associated with the elastic strain tensor ε.

The constitutive relations for isotropic material are given by

$$\boldsymbol{\sigma} = 2\mu^b\varepsilon + \lambda^b tr\left(\varepsilon\right)\boldsymbol{\delta} - b\left(p - p^0\right)\boldsymbol{\delta} \tag{1.12}$$

$$\left(p - p^0\right) = M\left[-btr(\varepsilon) + \left(\frac{m}{\rho_f^0}\right)\right] \tag{1.13}$$

where λ^b and μ^b are the Lame's constants under drained condition.

There are totally four parameters involved in the above linear poroelastic formulations: two elastic constants under drained conditions, λ^b and μ^b (or equivalently drained Young's modulus E^b and Poisson's ratio ν^b) as well as two coupling parameters b and M. The elastic constants may be identified in the framework of linear elasticity through standard laboratory tests. As for the Biot's coupling parameters, the following intrinsic relations have been derived from microstructural analysis for saturated porous media (Coussy, 1995; Dormieux et Kondo, 2005):

$$b = 1 - \frac{k^b}{k^s}, \quad \frac{1}{M} = \frac{b - \phi_c}{k^s} + \frac{\phi_c}{k^f}, \tag{1.14}$$

where k^s and k^f are the compressibility modulus of the solid matrix and the fluid, respectively, and ϕ_c denotes the connected porosity. The equation (1.14) can be recast into the form

$$b = \frac{1}{B^s}\left(1 - \frac{k^b}{k^u}\right), \tag{1.15}$$

$$B^s = \frac{bM}{k^u}, \quad k^u = k^b + b^2 M, \tag{1.16}$$

Above, k^u is the bulk modulus of the porous media under undrained conditions and can be determined from the stress-strain curve from an undrained hydrostatic compression test:

$$k^u = \left(\frac{\Delta\sigma_m}{\Delta\varepsilon_v}\right)_{\Delta m=0} \tag{1.17}$$

with $\sigma_m = tr\sigma/3$ being the mean stress and $\varepsilon_v = tr\varepsilon$ the volumetric strain. Through the same test, we can also measure the pore pressure generated by compressive stress and then the Skempton's coefficient B^s

$$B^s = -\frac{\Delta p}{\Delta\sigma_m}. \tag{1.18}$$

Back to (1.14), the drained bulk modulus k^b may be identified from the stress-strain curve obtained from a drained hydrostatic compression test

$$k^b = \left(\frac{\Delta \sigma_m}{\Delta \varepsilon_v} \right)_{p=0}. \tag{1.19}$$

Moreover, note that unlike macroscopic modulus k^b and k^u, the compressibility modulus of solid matrix k^s is a microstructure parameter. In practice, the modulus k^s (or more precisely, the average value of compressibility of the solid matrix) can be determined through a specific compression test in which the confining pressure and pore pressure are increased simultaneously with an increment $\Delta \sigma_m = \Delta p$. The following relation concerning the determination of the parameter k^s is then established

$$k^s = \left(\frac{\Delta \sigma_m}{\Delta \varepsilon_v} \right)_{\Delta \sigma_m = \Delta p} \tag{1.20}$$

1.3.2.2 Fundamentals of poroplasticity

We present in this section some fundamental formulations for modelling plastic behaviour of saturated porous media. More detailed discussions may be found in Biot (1973) and Coussy (1995 and 2004). The assumption adopted here of small disturbances for porous media which exhibit elastoplastic behaviour allows to decompose both the strain tensor and fluid mass into an elastic part and a plastic part

$$\varepsilon = \varepsilon^e + \varepsilon^p, \ m = m^e + m^p. \tag{1.21}$$

In practice, it is convenient to use a complementary state variable to describe irreversible change of fluid mass. For this, a parameter of plastic porosity change is introduced and defined as

$$\phi^p = m^p / \rho_f^0. \tag{1.22}$$

For later use, we also define the parameters of total induced porosity change ϕ and of elastic porosity change ϕ^e as follows

$$\phi = m / \rho_f^0, \quad \phi^e = m^e / \rho_f^0$$

The thermodynamic potential of poroelastic media is then extended by including plastic

process

$$\psi\left(\boldsymbol{\varepsilon}^e, m^e, \boldsymbol{V}_k\right) = g_m^0 m + \frac{1}{2}(\boldsymbol{\varepsilon} - \boldsymbol{\varepsilon}^p) : \mathbb{C} : (\boldsymbol{\varepsilon} - \boldsymbol{\varepsilon}^p) - M(\boldsymbol{b} : \boldsymbol{\varepsilon}^e)(\phi - \phi^p) + \frac{1}{2} M(\phi - \phi^p)^2 + \psi^p\left(\boldsymbol{V}_k\right) \tag{1.23}$$

where $\psi^p\left(\boldsymbol{V}_k\right)$ denotes locked energy due to plastic hardening, assumed to be function of internal hardening variables denoted by the set $\boldsymbol{V}_k$ (scalar for isotropic hardening and tensorial for kinematic hardening). The standard derivative of the thermodynamic potential (1.23) leads to the constitutive relations of elastoplastic behaviour of saturated media

$$\boldsymbol{\sigma} = \mathbb{C}^b : (\boldsymbol{\varepsilon} - \boldsymbol{\varepsilon}^p) - \boldsymbol{b}(p - p_0) \tag{1.24}$$

$$\left(p - p_0\right) = M[-\boldsymbol{b} : (\boldsymbol{\varepsilon} - \boldsymbol{\varepsilon}^p) + (\phi - \phi^p)] \tag{1.25}$$

The Clausius-Duhen inequality for intrinsic dissipation reads

$$\boldsymbol{\sigma} : \dot{\boldsymbol{\varepsilon}}^p + (p - p_0)\dot{\phi}^p - \boldsymbol{A}_k \dot{\boldsymbol{V}}_k \geq 0, \ \boldsymbol{A}_k = \frac{\partial \psi}{\partial \boldsymbol{V}_k} \tag{1.26}$$

Appropriate plastic laws are now required to fully determine the evolution rate of the state variables $(\dot{\boldsymbol{\varepsilon}}^p, \dot{\phi}^p, \dot{\boldsymbol{V}}_k)$. This may be done by establishing a (dual) plastic dissipation potential. Limited to a time-independent process, plastic complementary laws are defined by a yield function, a plastic potential in the case of non associated flow and a hardening function. The yield function is an indicative function of a convex elastic domain; it is a scalar function of stresses and thermodynamic forces associated with hardening variables, i.e.

$$f\left(\boldsymbol{\sigma}, p, \boldsymbol{A}_k\right) \leq 0 \tag{1.27}$$

For most geomaterials with internal friction, a non-associated plastic flow rule is needed. We thus have to define a complementary plastic potential, $g\left(\boldsymbol{\sigma}, p, \boldsymbol{A}_k\right)$, verifying the dissipation condition (1.26). Similar to the plastic yield function (1.27), $g\left(\boldsymbol{\sigma}, p, \boldsymbol{A}_k\right)$ can be expressed in the following general form

$$g\left(\boldsymbol{\sigma}, p, \boldsymbol{A}_k\right) = 0 \tag{1.28}$$

The evolution of plastic deformation and plastic porosity are calculated by following normality rule

$$\dot{\varepsilon}^p = \lambda \frac{\partial g\left(\boldsymbol{\sigma}, p, \boldsymbol{A}_k\right)}{\partial \boldsymbol{\sigma}},\ \dot{\phi}^p = \lambda \frac{\partial g\left(\boldsymbol{\sigma}, p, \boldsymbol{A}_k\right)}{\partial p},\ \dot{\boldsymbol{A}}_k = \lambda h\left(\boldsymbol{\sigma}, p, \boldsymbol{A}_k\right) \tag{1.29}$$

The complementary plastic laws are constrained by the Kuhn-Tucker conditions:

$$\lambda \geq 0,\quad f\left(\boldsymbol{\sigma}, p, \boldsymbol{A}_k\right) \leq 0,\quad \lambda f\left(\boldsymbol{\sigma}, p, \boldsymbol{A}_k\right) = 0 \tag{1.30}$$

The plastic multiplier $\lambda \geq 0$ is determined by the plastic consistency conditions $f = 0$ and $\dot{f} = 0$.

The above formulation provides the general framework for elastoplastic modelling of saturated porous media.

1.3.2.3 Elastic damage modelling of saturated porous media

Damage due to microcracks is known as essential mechanism of inelastic behaviors and failure process in a large class of geomaterials such as rocks and concrete. During recent decades, a number of research works have been devoted to physical characterization and mathematical modelling of brittle damage. Different types of constitutive models, based on either phenomenological or micromechanical approaches, have been developed. Damage modelling of saturated materials has recently been of great research interest and remains largely open. It is known that material damage affects not only mechanical behaviour but also hydromechanical and thermomechanical properties (Fauchet, 1991; Carmeliet, 1998). Here, we recall the framework of poroelastic damage and the determination method of some effective poroelastic parameters (Shao, 1998).

According to the theory of damage mechanics, the damage state of material is characterized by one or several internal variables (scalar and tensorial) , formally denoted by the set $\mathbf{d}$. Appropriate damage variables should have the ability of taking into account basic characteristics of microcracks such as crack density, crack size and orientation (Kachonov, 1993; Lemaitre, 1996). For the sake of simplicity, at present stage, the plastic deformation is not involved. It is also assumed that the initial undamaged material is linear elastic and that its mechanical response to stress unloading in constant damage state is also linear elastic. Given the existence of a thermodynamic potential, the constitutive relations of elastic damage behaviour for saturated porous media can be

deduced in the same way as that for dry materials. Considering a more general case that damage affects both elastic constants and poroelastic coupling coefficients, the thermodynamic potential in the system of poroelastic damaged media is then written as:

$$\psi(\varepsilon, m) = g_m^0 m + \frac{1}{2}\varepsilon : \mathbb{C}(\mathbf{d}) : \varepsilon - M(\mathbf{d})[\boldsymbol{b}(\mathbf{d}) : \varepsilon]\phi + \frac{1}{2}M(\mathbf{d})\phi^2 \tag{1.31}$$

where the fourth order tensor $\mathbb{C}(\mathbf{d})$ denotes the effective elastic stiffness of the damaged porous media in undrained condition. Analogically, $\boldsymbol{b}(\mathbf{d})$ and $M(\mathbf{d})$ are the effective Biot's coefficients tensor and the effective Biot's modulus, respectively. Contrast to the counterpart in (1.23), the energy (1.31) is now dependent on damage variable $\mathbf{d}$.

The standard derivative of the thermodynamic potential leads to the constitutive relations for elastic damage behaviour of saturated media:

$$\boldsymbol{\sigma} = \mathbb{C}^b(\mathbf{d}) : \varepsilon - \boldsymbol{b}(\mathbf{d})(p - p_0) \tag{1.32}$$

$$p = M(\mathbf{d})[-\boldsymbol{b}(\mathbf{d}) : \varepsilon + \phi] \tag{1.33}$$

It seems more convenient to use the porosity variation as a state variable instead of the change of fluid mass m / ρ_f^0. The free Skeleton energy may be separated from the free fluid enthalpy. The equation (1.33) is then rearranged into the form

$$\phi = \boldsymbol{b}(\mathbf{d}) : \varepsilon + \beta(\mathbf{d})p \tag{1.34}$$

where $\beta(\mathbf{d}) = 1/M(\mathbf{d})$ defines the compressibility of the pores, which is also function of damage variable.

In stationary damage state, the time derivative of (1.32) and (1.33) gives incremental forms of the constitutive relations:

$$\mathrm{d}\varepsilon = \mathbb{S}^b(\mathbf{d}) : \mathrm{d}\boldsymbol{\sigma} + \boldsymbol{H}(\mathbf{d})\mathrm{d}p \tag{1.35}$$

$$\mathrm{d}\phi = \boldsymbol{H}^*(\mathbf{d}) : \mathrm{d}\boldsymbol{\sigma} + \frac{\mathrm{d}p}{L(\mathbf{d})} \tag{1.36}$$

with

$$\boldsymbol{H}(\mathbf{d}) = \mathbb{S}^b(\mathbf{d}) : \boldsymbol{b}(\mathbf{d}) \tag{1.37}$$

$$\boldsymbol{H}^*(\mathbf{d}) = \boldsymbol{b}(\mathbf{d}) : \mathbb{S}^b(\mathbf{d}) \tag{1.38}$$

$$\frac{1}{L(\mathbf{d})} = \frac{1}{M(\mathbf{d})} + \boldsymbol{b}(\mathbf{d}) : \boldsymbol{H}(\mathbf{d}) \tag{1.39}$$

Above, the fourth order tensor $\mathbb{S}^b = (\mathbb{C}^b)^{-1}$ denotes the effective elastic compliance of a damaged material in drained conditions, and the second order symmetric tensor $\boldsymbol{H}(\mathbf{d})$ defines strain variations due to changes of pore pressure. $\boldsymbol{H}^*(\mathbf{d})$ is also a second order symmetric tensor producing stress-induced change of pore fluid. Finally, the scalar $L(\mathbf{d})$ establishes the relationship between the variation of pore pressure and the change of fluid mass. It is clear that all the effective coefficients are function of the damage state.

It is further assumed that there are three symmetric planes in damaged materials, which means that the effects of randomly distributed microcracks may be considered equivalent to those contributed by three orthogonal microcrack families (Kachanov, 1993). Therefore, it is possible to define three principal directions of damage state, and with the principal damage components, the effective compliance tensor $\mathbb{S}^b(\mathbf{d})$ may be written in the following matrix form:

$$\mathbb{S}^b = \begin{bmatrix} \frac{1}{E_1^b} & -\frac{\nu_{12}^b}{E_2^b} & -\frac{\nu_{13}^b}{E_3^b} & 0 & 0 & 0 \\ -\frac{\nu_{21}^b}{E_1^b} & \frac{1}{E_2^b} & -\frac{\nu_{23}^b}{E_3^b} & 0 & 0 & 0 \\ -\frac{\nu_{31}^b}{E_1^b} & -\frac{\nu_{32}^b}{E_2^b} & \frac{1}{E_3^b} & 0 & 0 & 0 \\ 0 & 0 & 0 & \frac{1}{2G_{23}} & 0 & 0 \\ 0 & 0 & 0 & 0 & \frac{1}{2G_{31}} & 0 \\ 0 & 0 & 0 & 0 & 0 & \frac{1}{2G_{12}} \end{bmatrix} \tag{1.40}$$

where $E_k^b \ (k = 1,2,3)$ and $\nu_{ij}^b \ (i, j = 1,2,3, \ i \neq j)$ are respectively the Young's modules and Poisson's ratio of the damaged material under drained condition and $G_{ij} \ (i, j = 1,2,3, \ i \neq j)$ the shear modulus. In a similar way, the coupling coefficient

tensor $\boldsymbol{H}(\mathbf{d})$ may be expressed as:

$$\boldsymbol{H}(\mathbf{d}) = \begin{bmatrix} \dfrac{1}{H_1} & 0 & 0 \\ 0 & \dfrac{1}{H_2} & 0 \\ 0 & 0 & \dfrac{1}{H_3} \end{bmatrix} \tag{1.41}$$

In rock mechanics, basic laboratory tests are usually performed on cylinder samples. In this particular case, a transversely isotropic behaviour is assumed. When the axis x_1 is chosen parallel to the cylinder axis, the following relations are obtained:

$$E_2^b = E_3^b,\ \nu_{12}^b = \nu_{13}^b,\ \nu_{21}^b = \nu_{31}^b,\ \nu_{23}^b = \nu_{32}^b,\ G_{12} = G_{31},\ H_2 = H_3 \tag{1.42}$$

and the incremental constitutive equations can be rewritten as:

$$\mathrm{d}\varepsilon_{11} = \frac{1}{E_1^b}\mathrm{d}\sigma_{11} - \frac{2\nu_{12}^b}{E_2^b}\mathrm{d}\sigma_{22} + \frac{1}{H_1}\mathrm{d}p \tag{1.43}$$

$$\mathrm{d}\varepsilon_{22} = \mathrm{d}\varepsilon_{33} = -\frac{\nu_{21}^b}{E_1^b}\mathrm{d}\sigma_{11} + \left(\frac{1-\nu_{23}^b}{E_2^b}\right)\mathrm{d}\sigma_{22} + \frac{1}{H_2}\mathrm{d}p \tag{1.44}$$

$$\frac{\mathrm{d}m}{\rho_f^0} = \frac{1}{H_1^*}\mathrm{d}\sigma_{11} + \frac{2}{H_2^*}\mathrm{d}\sigma_{22} + \frac{1}{L}\mathrm{d}p \tag{1.45}$$

The above equations may be inverted to give incremental stresses versus incremental strains and pore pressure:

$$\mathrm{d}\sigma_{22} = \left(\frac{E_2^b}{1-2\nu_{12}^b\nu_{21}^b-\nu_{23}^b}\right)(\mathrm{d}\varepsilon_{22} + \nu_{21}^b\mathrm{d}\varepsilon_{11}) - b_{22}\mathrm{d}p \tag{1.46}$$

$$\mathrm{d}\sigma_{11} = \left(E_1^b + \frac{2\nu_{12}^b\nu_{21}^bE_1^b}{1-2\nu_{12}^b\nu_{21}^b-\nu_{23}^b}\right)\mathrm{d}\varepsilon_{11} + \left(\frac{2\nu_{21}^bE_1^b}{1-2\nu_{12}^b\nu_{21}^b-\nu_{23}^b}\right)\mathrm{d}\varepsilon_{22} - b_{11}\mathrm{d}p \tag{1.47}$$

The two Biot's coefficients b_{11} and b_{22} are given in terms of some measurable quantities:

$$b_{11} = \left(\frac{E_1^b}{1 - 2\nu_{12}^b \nu_{21}^b - \nu_{23}^b} \right) \left(\frac{1 - \nu_{23}^b}{H_1} + \frac{2\nu_{21}^b}{H_2} \right) \tag{1.48}$$

$$b_{22} = \left(\frac{E_2^b}{1 - 2\nu_{12}^b \nu_{21}^b - \nu_{23}^b} \right) \left(\frac{\nu_{12}^b}{H_1} + \frac{1}{H_2} \right) \tag{1.49}$$

Thus, in the case of axisymmetric conditions, the effective poroelastic behaviour of damaged porous media is determined by 8 independent parameters: E_1^b, E_2^b, ν_{12}^b, ν_{21}^b, ν_{23}^b, G_{12}, H_1 and H_2, which are all dependent on the damage variable. The effective Biot's coefficients may be determined by combining (1.48) and (1.49). It follows in Chapter 2 some details on experimental method for determination of effective Biot's coefficients.

1.4 Objectives of this thesis

We have summarized the previous laboratory and theoretical works on physical description and numerical modeling of mechanical and poromechanical behavior in brittle geomaterials. So far as geomaterials are concerned, few works have been reported on laboratory investigations and constitutive modeling of coupled anisotropic poromechanical behaviors. The present work aims to fill up this research vacancy. First, a series of triaxial compression tests with different loading paths were conducted to study the anisotropic mechanical and poromechanical behavior of sandstone. Next, the discrete plastic damage model is extended to model anisotropic mechanical behaviors for dry materials and anisotropic poromechanical behaviors for saturated porous media, including the evolution of permeability and Biot's coefficients.

This thesis is organized as follows: we will present the experimental results of triaxial compression tests and of Biot's coefficients and permeability measuring tests on red sandstone in Chapter 2. A coupled anisotropic plastic damage model is developed in Chapter 3 within the discrete thermodynamic framework. In Chapter 4, the mechanical model is applied to simulate experimental data reported in Chapter 2, including modeling

of the evolution of permeability and Biot's coefficients. In the final chapter, the basic mechanical model is extended to simulate poroelastoplastic damage behaviors observed in drained and undrained compression tests as well as strain response in pore pressure change tests performed on Vosges sandstone.

Chapter 2 Experimental studies on red sandstone

In this chapter, the microscopic properties, triaxial compression tests, Biot's coefficients and permeability measuring tests of red sandstone are presented. Firstly, the microscopic scanning tests were conducted to investigate the composition and microstructure of the red sandstone. Secondly, the samples were stressed under triaxial loading to study the initial and stress-induced mechanical behaviour. Thirdly, effective Biot's coefficients in axial and lateral directions were measured at different deformation level to explore their evolution with deformation. Finally, in order to study the effect of stress on permeability, a series of axial permeability measuring tests were conducted under triaxial compression tests with cyclic loading. Fig. 2.1 shows the frame of this chapter.

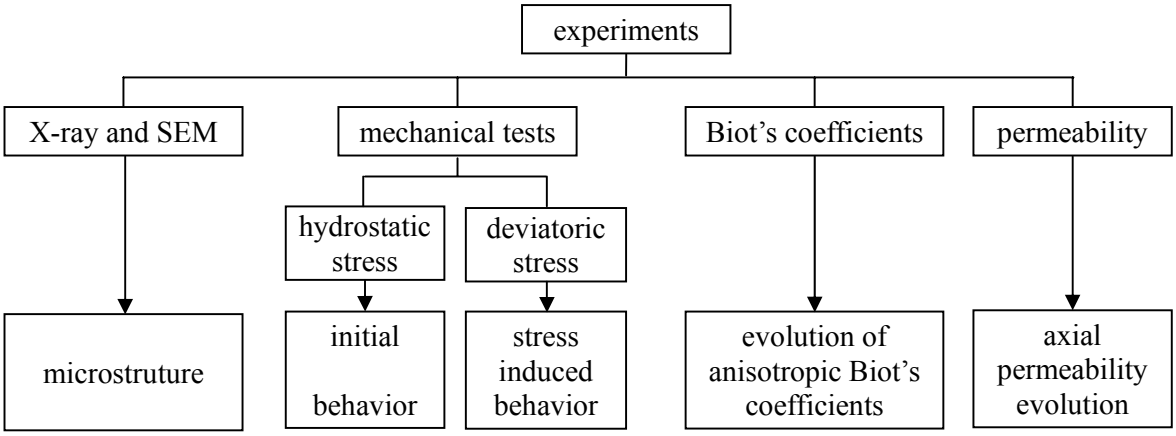

Fig. 2.1 *The framework of this chapter*

2.1 Studied sandstone

The rock studied in the present work is red sandstone from the Zhejiang province in China. The average porosity is about 21%; the density under dry and saturated conditions is 2.17g/cm3 and 2.35g/cm3, respectively. The petrophysical analysis with the X-ray diffraction

technique shows that the main mineral compositions of the sandstone are quartz, feldspar, mica and calcite, as shown in Table 2.1. The microscopic analysis of sandstone microstructure is also performed with the SEM technique. Two representative pictures are shown in Fig. 2.2. The quartz and feldspar grains are ovoid and surrounded by mica and calcite; this results in a continuous pore network which constitutes the connected porosity for interstitial fluid flow. The sandstone can be considered as a typical porous medium in the sense of Biot's theory, composed of skeleton and connected porosity. Further, due to the relative high porosity and small size of main mineral grains, it seems reasonable to use samples of centimetre scale as a representative volume element; and at this scale the sandstone can be seen as a continuous porous medium.

Table 2.1: Mineral compositions of red sandstone

Composition	Content (%)	Grain radius (mm)
quartz	55	0.02-0.35
feldspar	33	0.02-0.15
mica	5	0.002-0.02
calcite	4	0.002-0.02
chlorite	2	0.02-0.07
montmorillonite	1	0.02-0.07

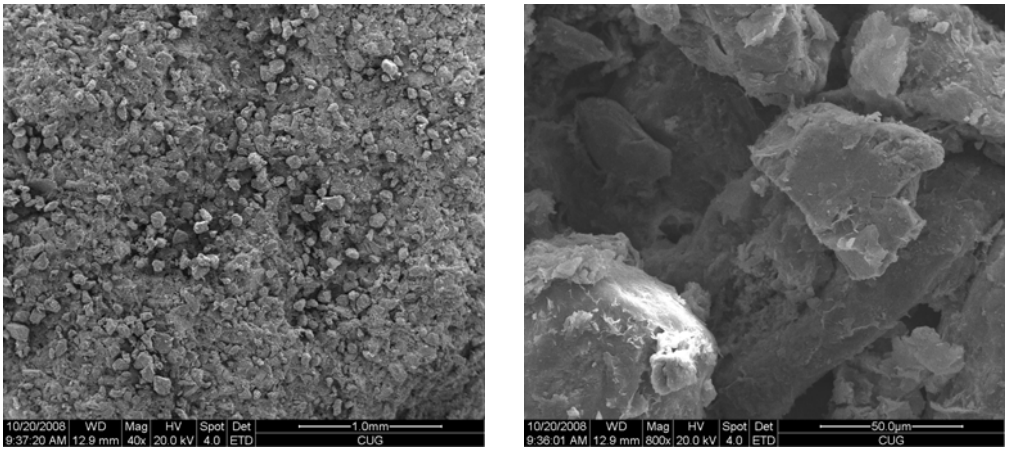

Fig. 2.2 *Microscopic structure (SEM)*

2.2 Experiment condition

Like most rocks, the mechanical behaviour of the red sandstone is sensitive to the saturation, scale, loading parameters and so on. In this section we will present the following aspects: preparation for samples, loading rate and temperature.

2.2.1 Preparation for samples

The samples are cored from a big block without macroscopic cracks, carefully cut from an intact layer in situ formation. Cylindrical samples are used and the average size is 50mm in diameter and 100mm in height. There is the presence of moderate parallel bedding planes in the sandstone, resulting in a slight transverse isotropic structure. The emphasis here is the study of poroelastic properties with induced anisotropy due to microcracks. The slight initial anisotropy of the sandstone is not investigated. All the samples are then drilled in the direction perpendicular to the bedding planes.

The saturation condition is an important factor for the determination of poroelastic properties. Thus, the sample is first saturated with distilled water in vacuum condition before each test. The sample is then inserted inside rubber jacket and thus isolated from confining pressure fluid. It is placed between two porous steel pads, in order to have uniform distribution of fluid pressure at the injection and outlet faces of the sample. In addition, after the application of confining pressure, the saturation of sample will be again verified by the injection of water from one side face until the set up of some uniform counter pressure.

2.2.2 Loading rate

As in previous studies (Paterson et al., 2005), rock compression strength is higher if the loading rate is greater, after investigating the effect of loading rate on strength and considering the quasi-static stress condition, the stress loading rate in triaxial compression tests were chose in magnitude order of 10^{-3}MPa/s.

2.2.3 Temperature

Thermal effects are not studied here and all the tests will be carried out under isothermal

conditions with room temperature, an air conditioning system was employed to control temperature maintained at 20±2°C.

2.3 Triaxial testing system

A thermo-hydro-chemic-mechanical (THMC) coupling test system was used to conduct the experiments (Fig. 2.3), the essential elements will be shown in this section.

2.3.1 Triaxial cell

In our laboratory, an auto-compensated cell was developed for triaxial tests (patent No. 9007594). In this cell, an auto-compensated room allows to counterbalance the piston load due to the confining pressure alone, so that the external loading device only apply the net axial force itself plus the friction on the piston, which is a much smaller net force than would otherwise be the case when the confining pressure is high. In addition, an external furnace was developed to heat the whole pressure cell; the maximum temperature is up to 90°C and an inside thermocouple was used. A special type of oil named as ENERPACK HF95Y was used as the confining medium.

The samples used for this cell are cylinder and the sizes can be Φ20mm×40mm, Φ37.5mm×75mm or Φ50mm×100mm. The maximum confining pressure is up to 100MPa and the stroke length of piston is up to 20mm. Some measurement methods were designed for this cell, they were as follows:

- Strain gauge
- Lateral deformation collar
- 1 linear variable differential transformer (LVDT) transducer on the stroke of the piston and 2 LVDT transducers on the axial deformation
- Measurement of fluid volume injected in or exhaust out of the sample
- Confining pressure sensor
- Deviatoric stress sensor
- Pore pressure sensor

All of classic mechanical tests on rock can be conducted with this cell:

- Hydrostatic compression test, classic triaxial drained or undrained test with or without

temperature variation

- Hydrostatic or triaxial creep test
- Permeability test
- Cyclic stress loading test
- Proportion loading test
- Lateral extension test
- Mechanical-temperature coupling test
- Mechanical-chemical coupling test
- Thermo-hydro-mechanical-chemical (T-H-M-C) coupling test

2.3.2 High pressure pump

Three high pressure pumps are respectively employed for deviatoric stress, confining and pore pressure. Table 2.2 shows their detail parameters.

Table 2.2 Parameters of pump

parameters	deviatoric stress pump	confining pressure pump	pore pressure pump
maximum pressure (MPa)	100	100	100
accuracy (MPa)	±2	±2	±2
flow scale (mm^3/s)	0.05～50	0.05～50	0.05～50
control method	pressure, flow, deformation	pressure, flow	pressure, flow
medium	oil	oil	water, oil, chemical liquid

2.3.3 Deformation measuring procedure

Some methods were developed to measure the sample deformations under the necessary of tests.

Axial deformation measurement:

- Strain gauge
- LVDT

Lateral deformation measurement:

- Strain gauge
- Collar using LVDT (patent No.05/05203)
- Collar using strain gauge (patent No.05/05204)

Capillary tube was used to measure the volume deformation.

2.3.4 Microcomputer system

A microcomputer system with software was used under laboratory view, by which we can control the three pumps and record the values from the above mentioned sensors.

2.3.5 Auxiliary devices

There are also some auxiliary devices which can be chose in triaxial tests under test need.

- Siliconized rubber tube for isolating the sample
- Modified siliconized rubber tube (with three metal gasket) for isolating the sample from confining medium in creep test
- Metal pipe for access of interstitial fluid
- Capillary tube for volume measure of fluid in or out the sample
- A vacuum pump and sealed container for saturating the sample

2.4 Test results

In the present work, different laboratory tests will be performed, including hydrostatic compression, monotonous triaxial compression, triaxial compression with unloading - reloading cycles for the determination of Biot's coefficients and permeability measuring.

Throughout the dissertation, the rock mechanics sign convention will be used; the positive sign will be used for compressive stresses and strains. Further, a fixed coordinate frame will be used for the cylinder sample as shown in Fig.2.3; the cylinder axis is parallel to the axis x_1. σ_i and ε_i ($i = 1,2,3$) denote the three principal stresses and strain in this frame while p is the interstitial pressure.

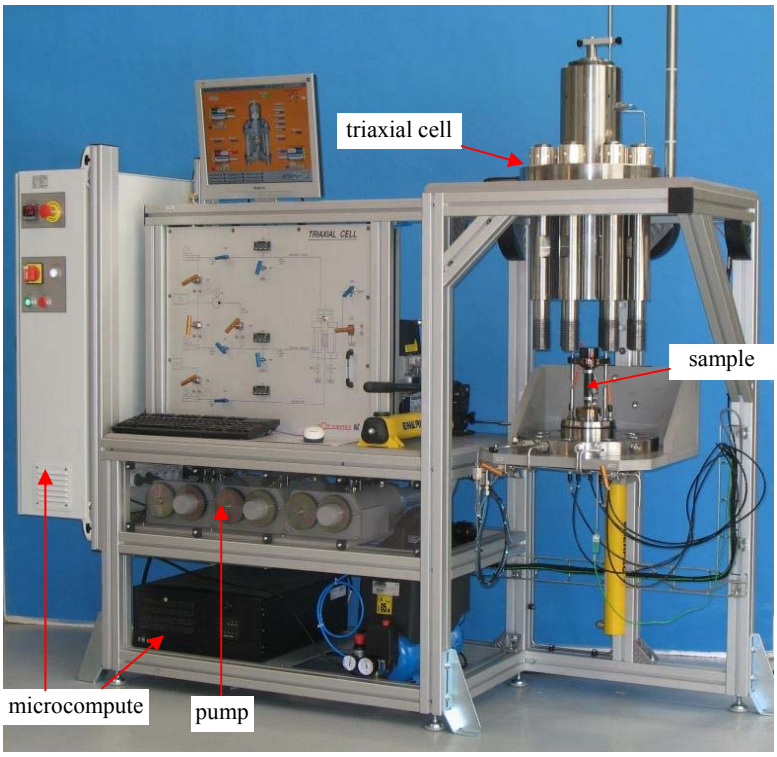

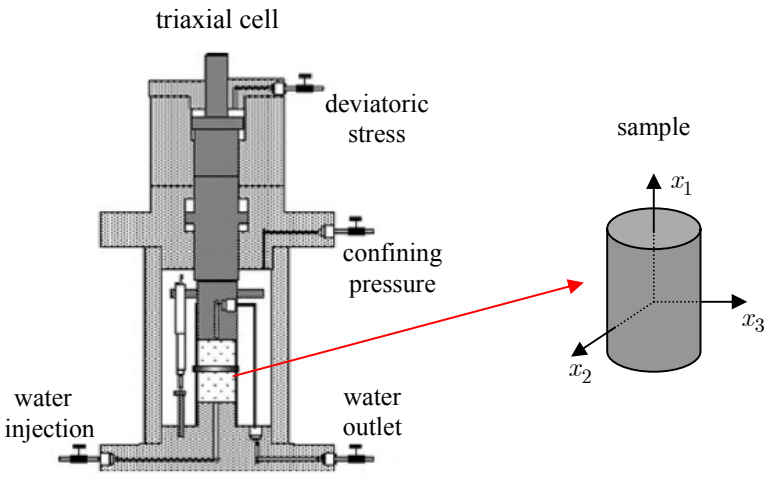

Fig. 2.3 *Test system, triaxial testing cell and the coordinate frame of sample*

2.4.1 Mechanical tests

Both hydrostatic and deviatoric stress tests were respectively conducted in order to study the mechanical behaviour.

2.4.1.1 Hydrostatic stress tests

Hydrostatic compression tests are first performed in order to determine the volumetric compressibility of sandstone and initial value of Bio's coefficient in initial (undamaged) state. In this classic test, the sample is subjected to hydrostatic stress loading with $\sigma_1 = \sigma_2 = \sigma_3$. Two loading conditions are considered: drained test with constant interstitial pressure ($\Delta p = 0$) and partially drained test with prescribed interstitial pressure equal to confining pressure ($\Delta p = \Delta\sigma_m$) with σ_m being the mean stress.

In the first case, the hydrostatic stress is increased with constant rate of 8×10^{-3} MPa/s in drained condition with $\Delta p = 0$. This load rate is chosen according to rock permeability in order to avoid excessive pore pressure generated by hydrostatic stress. Typical stress strain curves are presented in Fig. 2.4. The axial strain is slightly different with radial (or lateral) one under hydrostatic stress; this confirms the small structural anisotropy of the sandstone. Further, both the axial and radial strains exhibit a non linear phase during the first stage of loading. Such a non linearity may be attributed to the progressive closure of initial microcracks and defeats. We recover a linear response phase after certain value of hydrostatic stress, say about $18\,\text{MPa}$; this linear phase should reflect the elastic behaviour of sandstone in hydrostatic condition. Volumetric strain is simply calculated by $\varepsilon_v = \varepsilon_1 + 2\varepsilon_3$ and shown on the same figure. From this linear phase, we can easily calculate the bulk modulus of sandstone in drained condition noted by k^b with (1.19).

On the other hand, a second hydrostatic test is performed. Hydrostatic stress and pore pressure are simultaneously increased with the same rate ($\Delta p = \Delta\sigma_m$) as that in the first drained test. The objective here is the determination of compressibility modulus of the solid skeleton material (or solid matrix) k^s. Typical stress strain curves are shown in Fig. 2.5. We also observe some slight anisotropy of axial and radial strains and a small non linear phase at the beginning of loading. This seems to show that the slight structural anisotropy of sandstone

is mainly related to oriented microstructure of the solid matrix. And there exists some isolated microcracks inside the solid matrix contributing to the nonlinear response of this one. After the calculation of the volumetric strain, the compressibility modulus of the solid matrix can be calculated from the linear phase by (1.20).

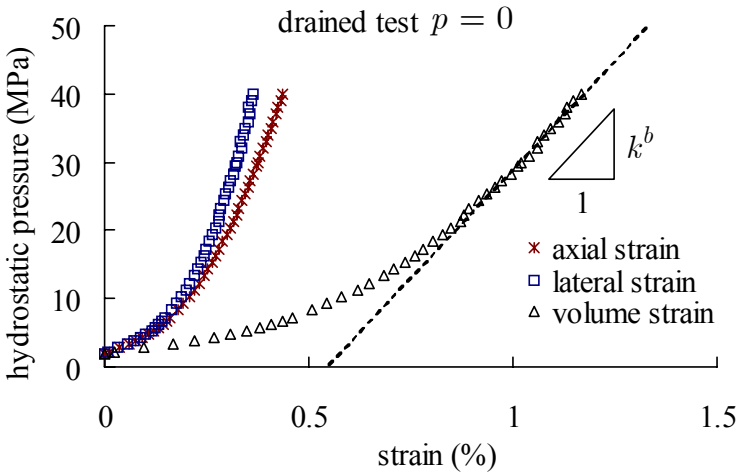

Fig. 2.4 *Stress-strain curves in hydrostatic compression tests under drained conditions*

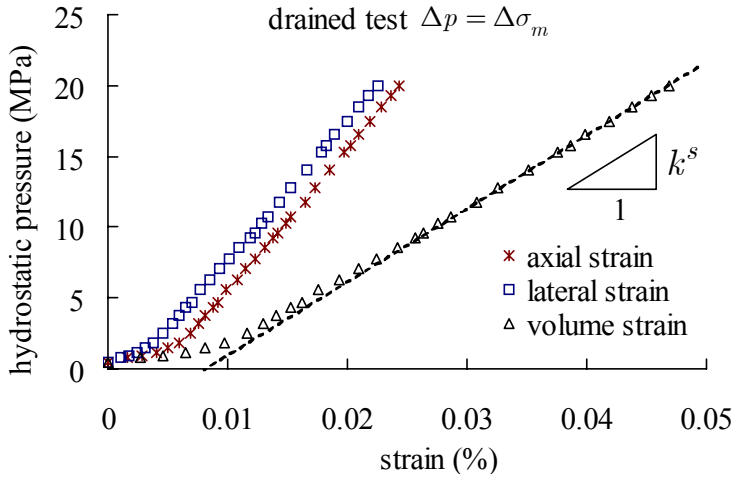

Fig. 2.5 *Stress-strain curves in hydrostatic compression tests under partially drained conditions*

As mentioned above, the slight structural anisotropy is neglected here and the initial state of sandstone is assumed to be isotropic one. According to the relations between Biot's coefficient and compressibility properties of constituents, the initial Biot's coefficient of

sandstone, noted by b is given by:

$$b = 1 - \frac{k^b}{k^s} \tag{2.1}$$

For the sandstone studied, the initial values of drained bulk modulus, compressibility modulus of solid matrix and Biot's coefficient are summarized in Table 2.3.

Table 2.3 Initial values of compressibility modulus and Biot's coefficient of sandstone

k^b (MPa)	k^s (MPa)	b
6905	50548	0.86

2.4.1.2 Deviatoric stress tests

In order to investigate basic mechanical behaviour of sandstone, monotonous triaxial compression tests are now performed in drained conditions and under different values of confining pressure. The loading procedure is conventional and composed of two stages: set up of confining pressure and application of deviatoric stress. All the tests are conducted in strain controlled conditions in order to get post peak responses. The average strain rate is 3×10^{-6} /s (corresponding to an average stress rate of 10^{-3}MPa/s); which is chosen as low as enough in order to avoid excessive interstitial over pressure and to verify the condition ($\Delta p = 0$). Five values of confining pressure are used such as 0, 5, 10, 20 and 30MPa. In Fig. 2.6, we show axial, radial and volumetric strains as functions of deviatoric stress ($\sigma_1 - \sigma_3$) for the five values of confining pressure. These results are quite representative for most brittle rocks such as sandstone and the following main remarks can be issued.

1) The mechanical response of sandstone is strongly dependent upon confining pressure. Under low confining pressure, in particular in uniaxial compression test ($\sigma_2 = \sigma_3 = 0$), there exists some non linear phase at the beginning of deviatoric loading. This non linear phase is attributed to the progressive closure of initial microcracks in the axial direction. With the increase of confining pressure, such a non linear phase disappears because the initial microcracks are almost closed during the application of confining stress. Also, under

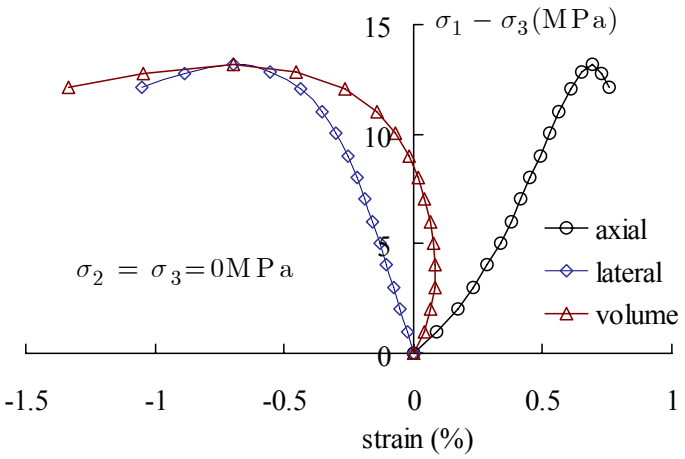

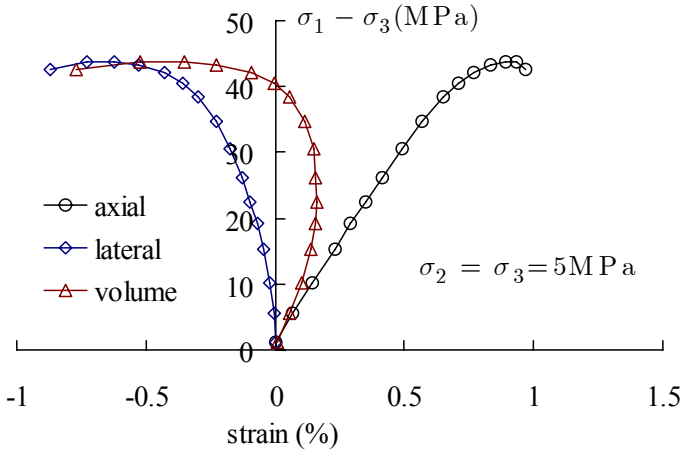

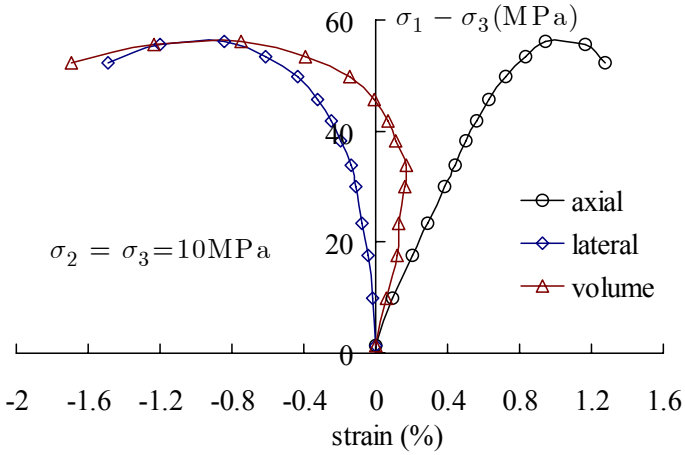

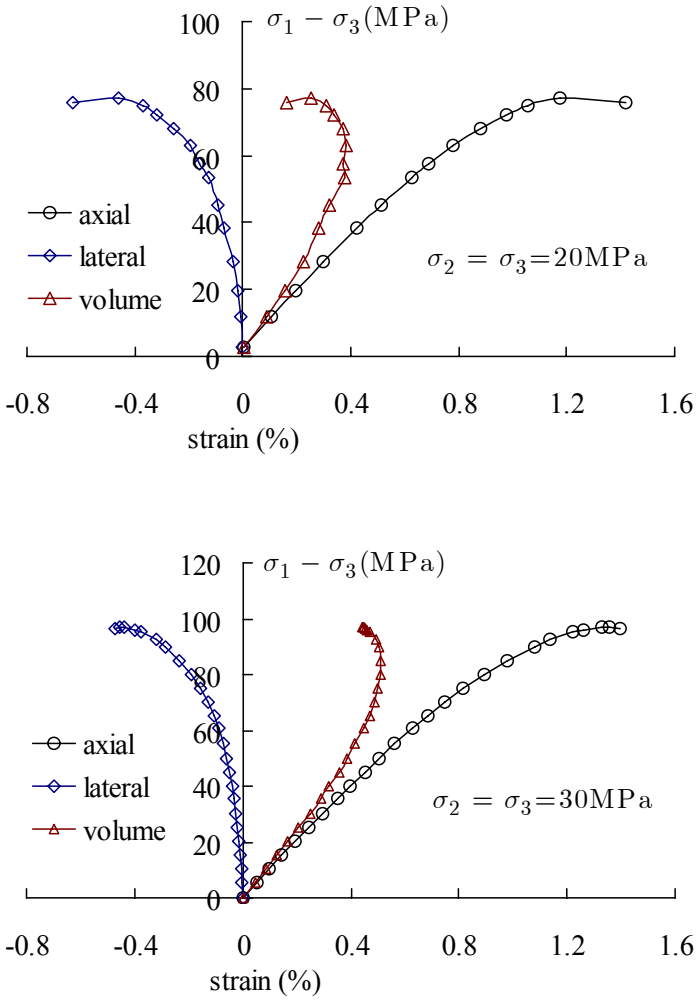

Fig. 2.6 *Stress-strain curves of triaxial compression tests under different confining pressures*

low confining pressure, the sample failure is marked by sharp peak stress; due to the coalescence of cracks leading to splitting of sample. Under higher confining pressures, this peak stress state is much less pronounced and even disappears. The failure of sample is generally associated with the onset of shear or compaction bands (Steif, 1984; Moore et Lockner, 1995; Olsson, 1995). There is a clear transition from brittle to ductile behaviour with confining pressure increase.

2) For all confining pressures, after a more and less marked linear stress strain phase, we observe non linear responses of material before and after peak stress. These non linear inelastic strains are directly related to the nucleation and growth of microcracks and mainly generated by frictional sliding along cracks surfaces.

3) There is a clear transition from volumetric compressibility to dilatancy for almost all the confining pressures considered. However, this transition occurs much earlier and the volumetric dilatancy is more important under low confining pressure than higher one. Physically, this volumetric dilatancy in brittle rocks under compressive stresses may be related to the normal opening of microcracks generated by frictional sliding along rough crack surfaces.

4) In Fig. 2.7, we have reported the values of (peak) failure stress as functions of confining pressure. For the reason of completeness, the values of failure stress obtained from the tests presented in the later sections are also presented. We can see that the failure line is non linear for the regime of low confining pressures and progressively becomes quasi linear for higher ones. This indicates that the failure condition of sandstone is more sensitive to confining pressure when its value is low. For the purpose to get some indicative values of failure parameters, we tried to represent the failure stresses of sandstone by the classic linear Mohr-Coulomb criterion. The following values are obtained for material cohesion and frictional angle: $c = 6.3\mathrm{MPa}$ and $\tan\varphi = 0.684$.

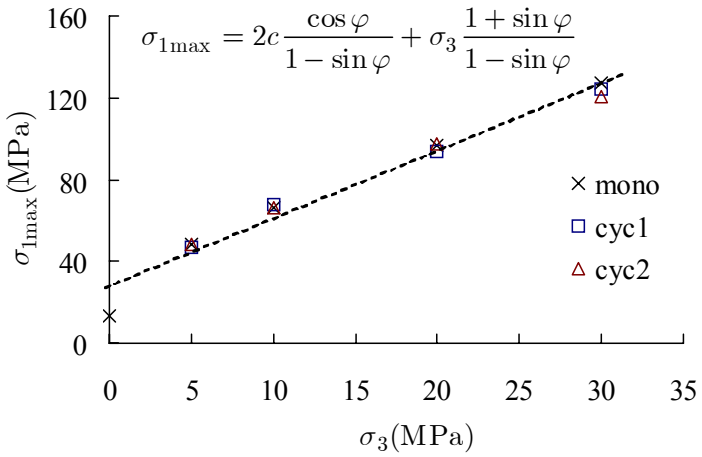

Fig. 2.7 *Experimental values of failure stress and Mohr-Coulomb criterion fitting, with the data obtained from the three series of tests (monotonous, "cyc1" for determination of Biot's coefficients and "cyc2" for permeability determination)*

2.4.2 Evolution of Biot's coefficient

In this section, specific triaxial compression tests are performed in order to investigate the

evolution of Biot's coefficient with induced damage by microcracks.

2.4.2.1 Determining method of Biot's coefficients

In Section 1.4.2, we have formulated the determination method of Biot's coefficients in damaged material. According to (1.48) and (1.49), for the determination of Biot's coefficients, the laboratory tests consist in the measurement of two elastic modulus E_1^b and E_3^b, three Poisson's ratios ν_{31}^b, ν_{13}^b and ν_{32}^b, and the two coupling parameters H_1 and H_3, for different levels of deviatoric stress. Note that the Biot's coefficients given in (1.48) and (1.49) are determined for a given damage state; the measurement of the elastic parameters and coupling coefficients should be performed during elastic loading process without additional damage evolution. This is done by proceeding unloading-reloading cycles during triaxial tests. The testing procedure is described as follows and schematically illustrated in Fig. 2.8.

1) Setting up of confining pressure to desired value under drained condition;
2) The axial displacement is increased with a fixed rate and corresponding deviatoric stress is monitored, while the confining pressure is kept constant;
3) When the deviatoric (or axial) stress reaches a desired value corresponding to certain state of damage, a unloading-reloading cycle of axial stress is proceeded;
4) The unloading-reloading phase corresponds to poroelastic response of material without damage evolution; the poroelastic relations (1.35) can be used. During the unloading of axial stress, the radial stress (or confining pressure) and interstitial pressure remain unchanged. The incremental strains are given by $\Delta\varepsilon_1 = \Delta\sigma_1 / E_1^b$ and $\Delta\varepsilon_3 = (-\nu_{31}^b \Delta\sigma_1) / E_1^b$. This leads to the determination of E_1^b and ν_{31}^b.
5) After the unloading of axial stress to certain chosen value (see Fig. 2.8), the axial stress is hold at this value and we increase the radial stress with some incremental value (the final radial stress remains lower than the axial stress) and measure the variations of axial and radial strains; which are related to the variation of radial stress by $\Delta\varepsilon_1 = (-2\nu_{13}^b \Delta\sigma_3) / E_3^b$ and $\Delta\varepsilon_3 = (1-\nu_{32}^b)\Delta\sigma_3 / E_3^b$. Et the end of this step, the radial stress is back to its initial value. This step leads to the determination of the quantities ν_{13}^b / E_3^b and $(1-\nu_{32}^b) / E_3^b$.
6) In this step, an incremental variation of interstitial pressure is applied by water injection

into the sample while keeping the axial and radial stresses constant. Note that the magnitude of pressure variation should be small in order to avoid additional growth of microcracks and to keep the loading step in elastic range. The variations of axial and radial strains are measured as functions of pressure variation and the following relations hold: $\Delta\varepsilon_1 = \Delta p / H_1$ and $\Delta\varepsilon_3 = \Delta p / H_3$. At the end of this step, the injected water is outlet and the interstitial pressure is back to its initial value. During this step, the values of two coupling coefficients (H_1, H_3) can be easily determined.

By combination of the steps (4-6), we should determine 7 parameters with only 6 measured quantities. More precisely, in the step (5), we should determiner three elastic parameters with only two measured strains. In order to overcome this difficulty, we propose the following simplification: the Poisson's ratio corresponding to the isotropic plane, say ν_{23}^b is not significantly affected by the induced damage and remains at the initial value of undamaged material. This initial value is easily determined from the linear part of stress strain curves in a triaxial compression test and the average value is found to be $\nu_{23}^b = 0.23$. Such a simplification seems to be plausible in triaxial compression conditions due to the fact that the induced microcracks are mainly oriented in the axial direction.

The most important difference between the current test and the test of strain response to pore pressure increment, which was mentioned in Section 1.3.3, is that: the process of pore pressure loading in the latter one can be elastic or inelastic and it may cause further damage induced by microcrack growth; however, in the former one, the process of pore pressure loading is ensured to be elastic, in other words, the pore pressure is restricted to make sure that no further microcracks growth is generated.

2.4.2.2 Test results

A series of four tests are performed with the different values of confining pressures (5, 10, 20 and 30MPa), following the testing procedure described above. Typical results are plotted in Fig. 2.9-2.12. As the emphasis here is to study poroelastic properties, pay our attention to the curves of strain variation due to interstitial pressure change. We can see that the variations of

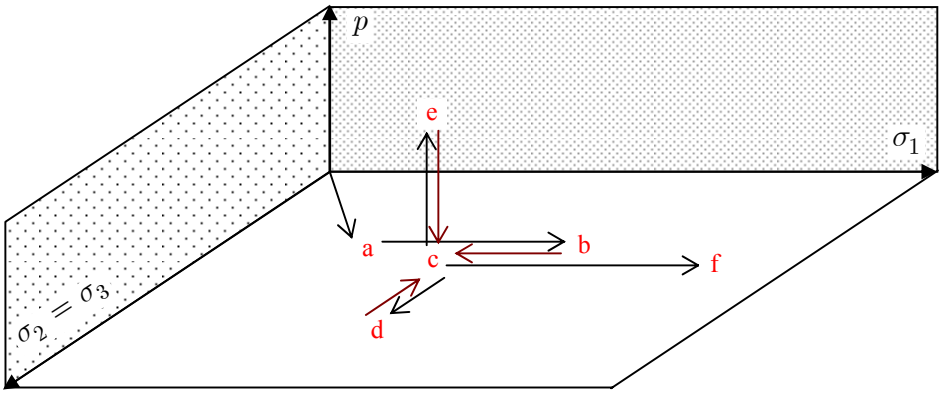

(a) Loading path in stress space ($\sigma_1, \sigma_2 = \sigma_3, p$)

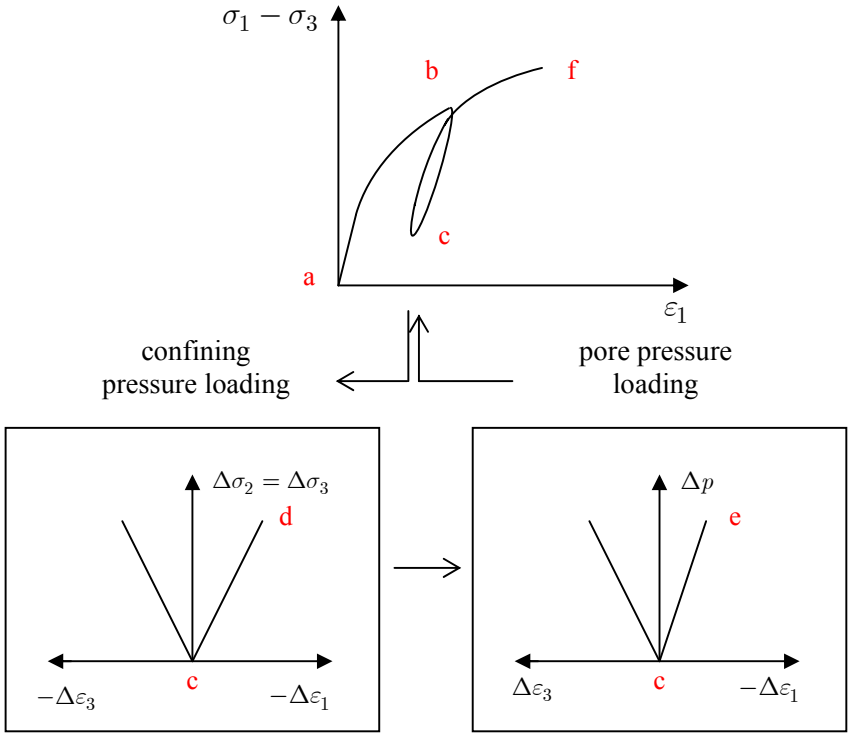

(b) Stress-strain curves in one measuring process

Fig. 2.8 *Schematic illustration of loading path for the determination of Biot's at different levels of deviatoric stress: (a) stress and pressure path and (b) corresponding strain measurement*

strain are clearly anisotropic between in axial and radial directions, in particular under high value of deviatoric stress (high level of damage). This is typically the consequence of induced anisotropic damage in sandstone. The variation of axial strain is much important than the radial one during the interstitial pressure change. This means that the Biot's coefficient in the axial direction (b_1) becomes higher than the radial one (b_3). This anisotropy of Biot's coefficients is in correlation with the fact that the induced microcracks are mainly oriented in the axial direction.

For more details, the experimental values of elastic parameters and coupling coefficients are reported in Tables 2.4-2.7, respectively for the four values of confining pressure; the corresponding values of Biot's coefficients are calculated and also given in these Tables. For more clarity, the evolutions of effective elastic modulus and Biot's coefficients are plotted as functions of the relative axial strain in Fig. 2.13 and 2.14, respectively. From these data, some interesting remarks can be drawn.

1) Under low values of the axial strain, i.e. when the induced damage is still negligible, the difference of elastic modulus between the axial direction (E_1^b) and radial direction (E_3^b) is quite small. And this difference is as smaller as the confining pressure is higher. This confirms the slight structural anisotropy of the sandstone and this initial anisotropy is progressively attenuated by the confining pressure due to the closure of bedding planes and initial microcracks. However, at the same time, the values of elastic modulus increase with the confining pressure due to this compaction effect.
2) In Fig. 11, the variations of elastic modulus are presented as functions of the relative axial strain. We can see that the axial modulus increases in the first stage and the decrease when the axial peak strain is closed. This means that the elastic modulus in the axial direction is not clearly deteriorated by the induced damage. This may be explained by the fact that most induced microcracks are mainly parallel to the axial direction. On the other hand, the radial elastic modulus is decreasing almost continuously with the axial strain and then growth of induced damage. Therefore, with the progress of induced damage under higher values of axial strain, the effective elastic modulus are affected. The deterioration of the radial modulus is much more significant than the axial one, and there is an induced anisotropy on the elastic properties of sandstone. However, the deterioration of the radial elastic modulus is more important under low confining pressures. This indicates that the evolution of

induced damage becomes smaller under higher confining pressure. This is in conformation with the transition from brittle to ductile behaviour in most brittle rocks.

3) Look at now the evolution of Biot's coefficients in the axial and radial directions. Some interesting remarks can be drawn. Under low axial strains, i.e. in undamaged or moderate damage state, the Biot's coefficient in the axial direct (b_1) is higher than that in the radial direction (b_3). This confirms the existence of bedding planes (which are perpendicular to the cylinder axis) in the initial state of sandstone. In a logic way, the difference of Biot's coefficient between the two directions is largely attenuated with the confining pressure; this is well correlated with the closure of bedding planes. Another interesting phenomenon is that the values of Biot's coefficients at lower axial strains (considered as undamaged or moderate damage state) decrease quite significantly with confining pressure; this is also correlated with the closure of initial bedding planes and microcracks.
4) Under higher axial strains, the induced damage has developed. The Biot's coefficients are affected by the induced damage. In an average way, the Biot's coefficient in the axial direction (b_1) is in most time decreasing with the axial strain. This decrease is associated with the progressive closure of bedding planes and initial microcracks, which are perpendicular to the axis (x_1). In induced microcracks are developed essentially in the direction parallel to the axis (x_1). Therefore, the Biot's coefficient (b_1) is not affected by the induced damage. Only under very higher level of load and damage, approaching to the coalescence of microcracks, the Biot's coefficient (b_1) is affected by the induced damage and increases with axial strain, for instance in the test with 5MPa confining pressure. On the other hand, the Biot's coefficient in the radial direction (b_3) is significantly affected by the induced damage due to the preferential orientation of microcracks. This coefficient is almost continuously increasing with the nucleation and growth of induced damage. However, the rate of such an increase is lower when the confining pressure higher; this confirms again that the damage evolution rate is smaller under higher confining pressure. Note that in the test with 5MPa confining pressure, the axial Biot's coefficient (b_1) is also significantly increasing with axial strain and both the values of (b_1) and (b_3) become higher than the unit at the end of loading. This is theoretically impossible and should be considered with critical caution.

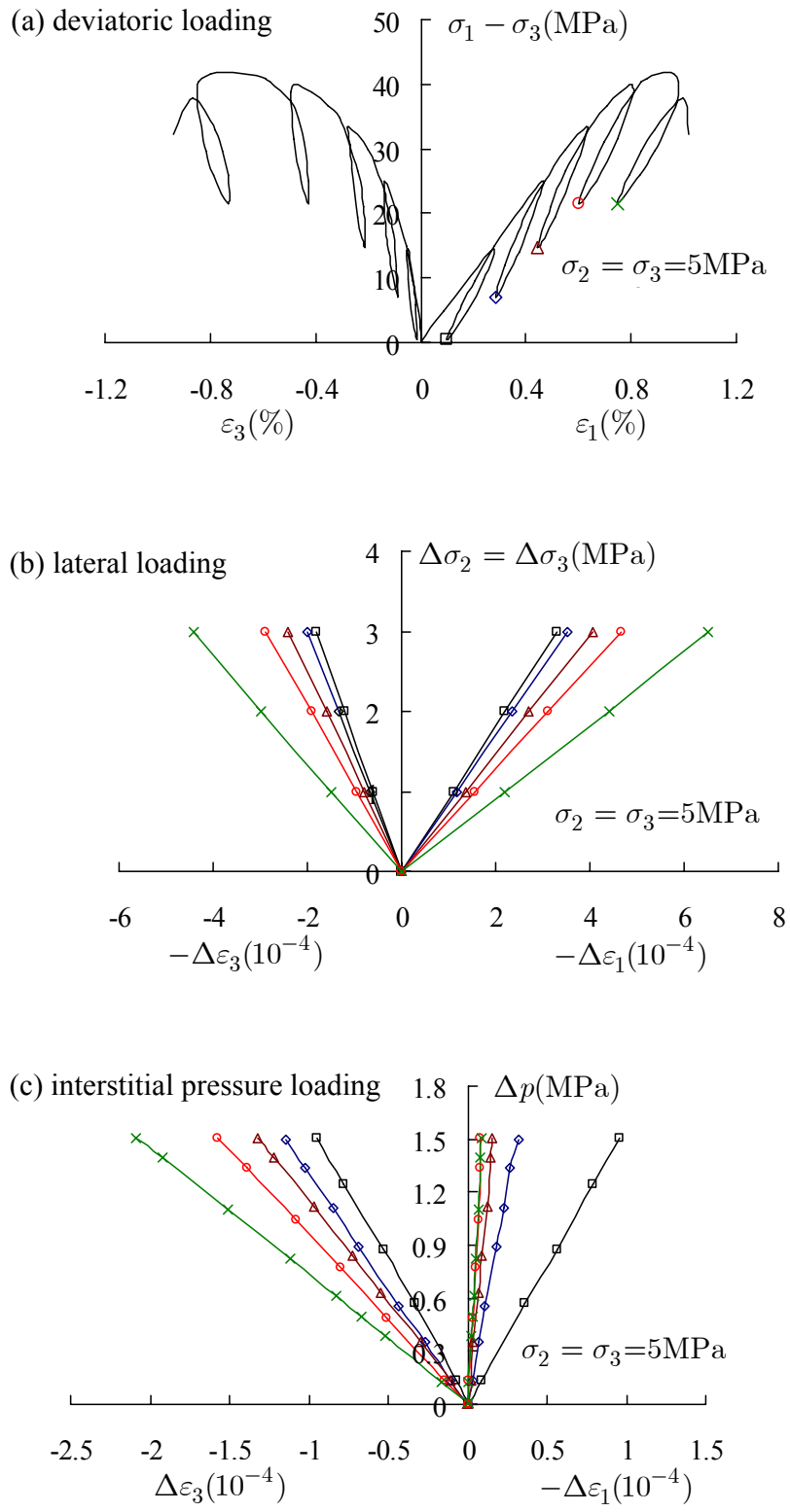

Fig. 2.9 *Triaxial compression test under 5MPa confining pressure: (a) Stress-strain curves, (b) variations of strains due to radial stress, and (c) interstitial pressure variations*

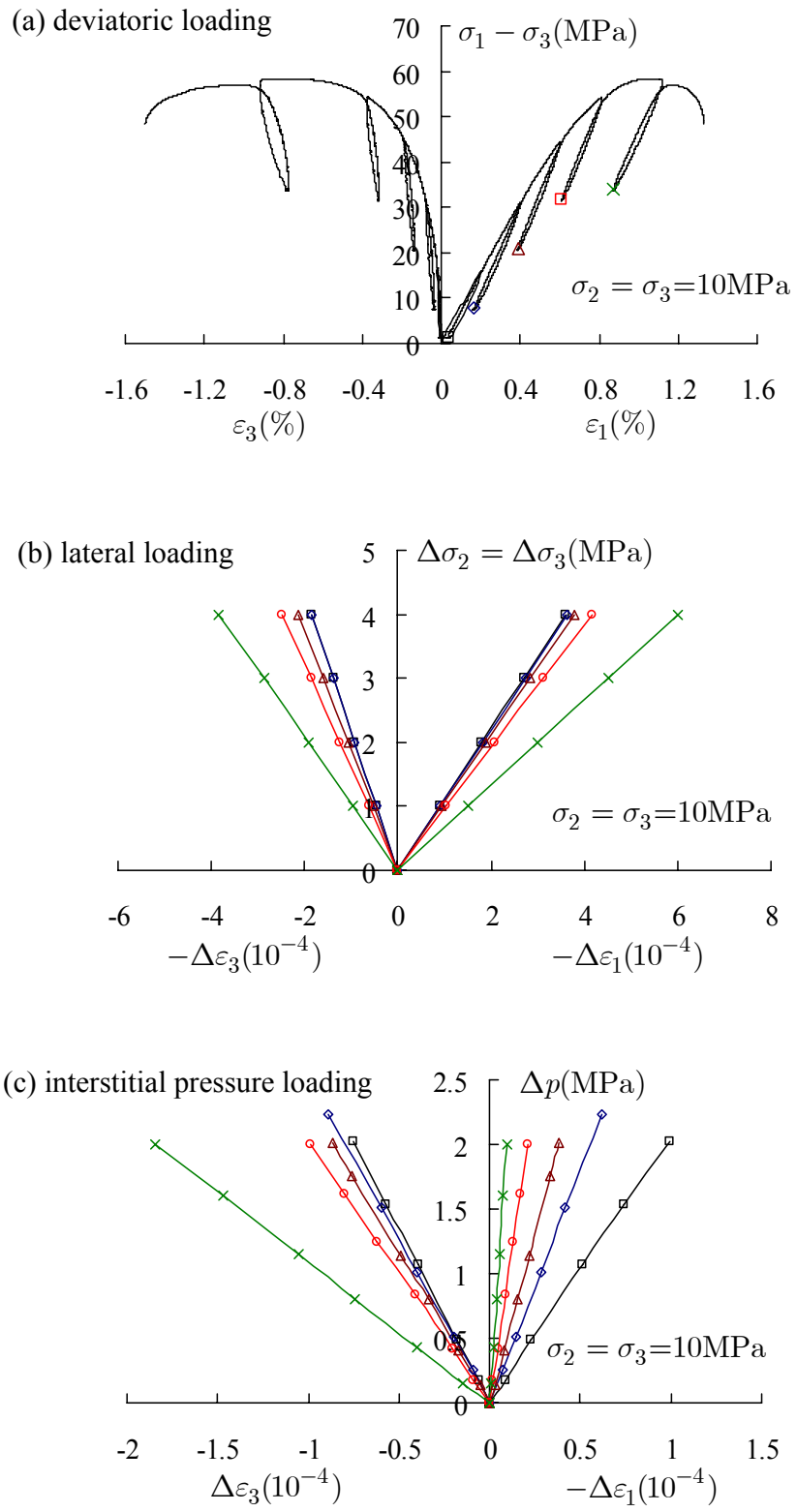

Fig. 2.10 *Triaxial compression test under 10MPa confining pressure: (a) Stress-strain curves, (b) variations of strains due to radial stress, and (c) interstitial pressure variations*

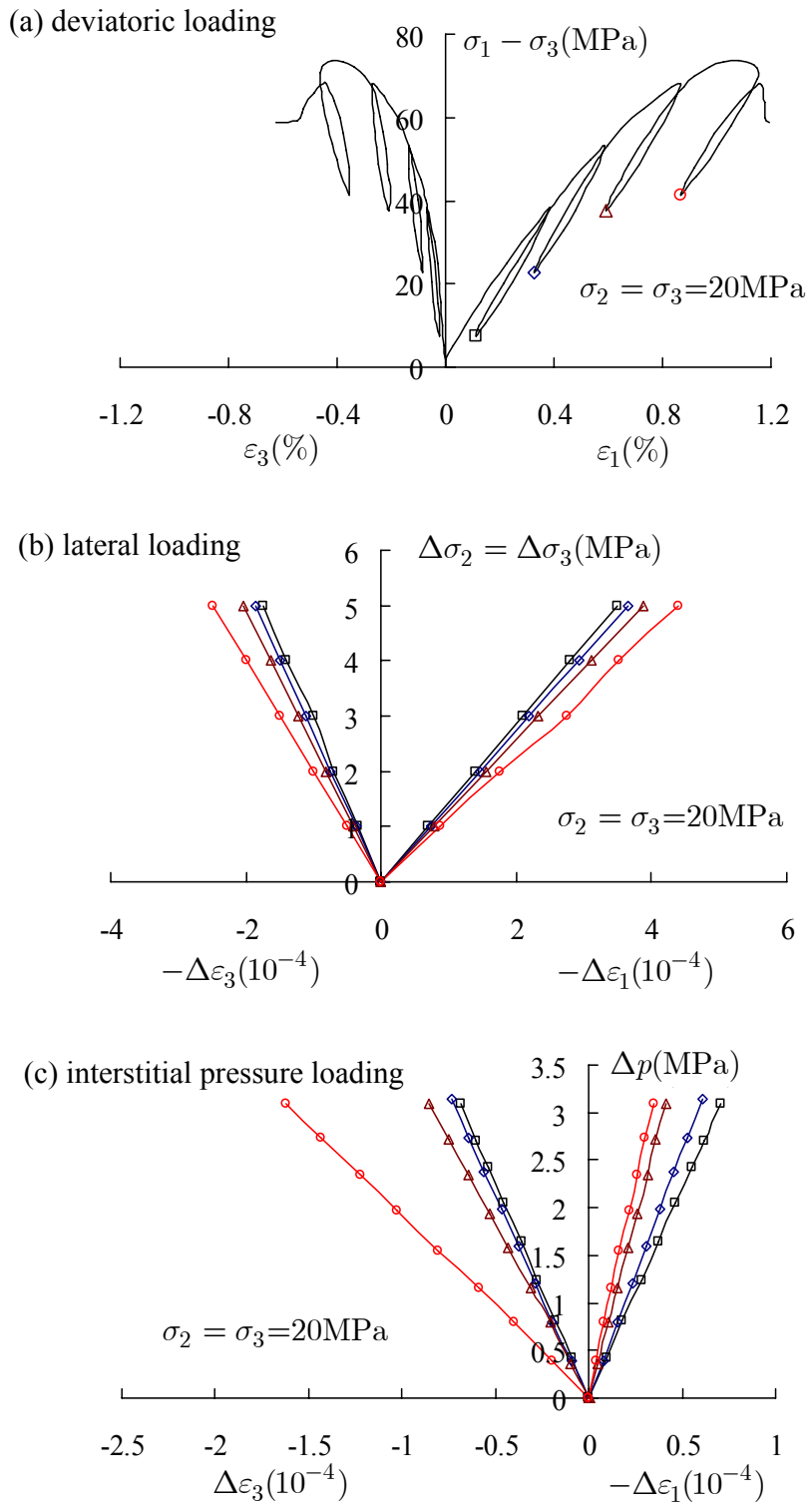

Fig. 2.11 *Triaxial compression test under 20MPa confining pressure: (a) Stress-strain curves, (b) variations of strains due to radial stress, and (c) interstitial pressure variations*

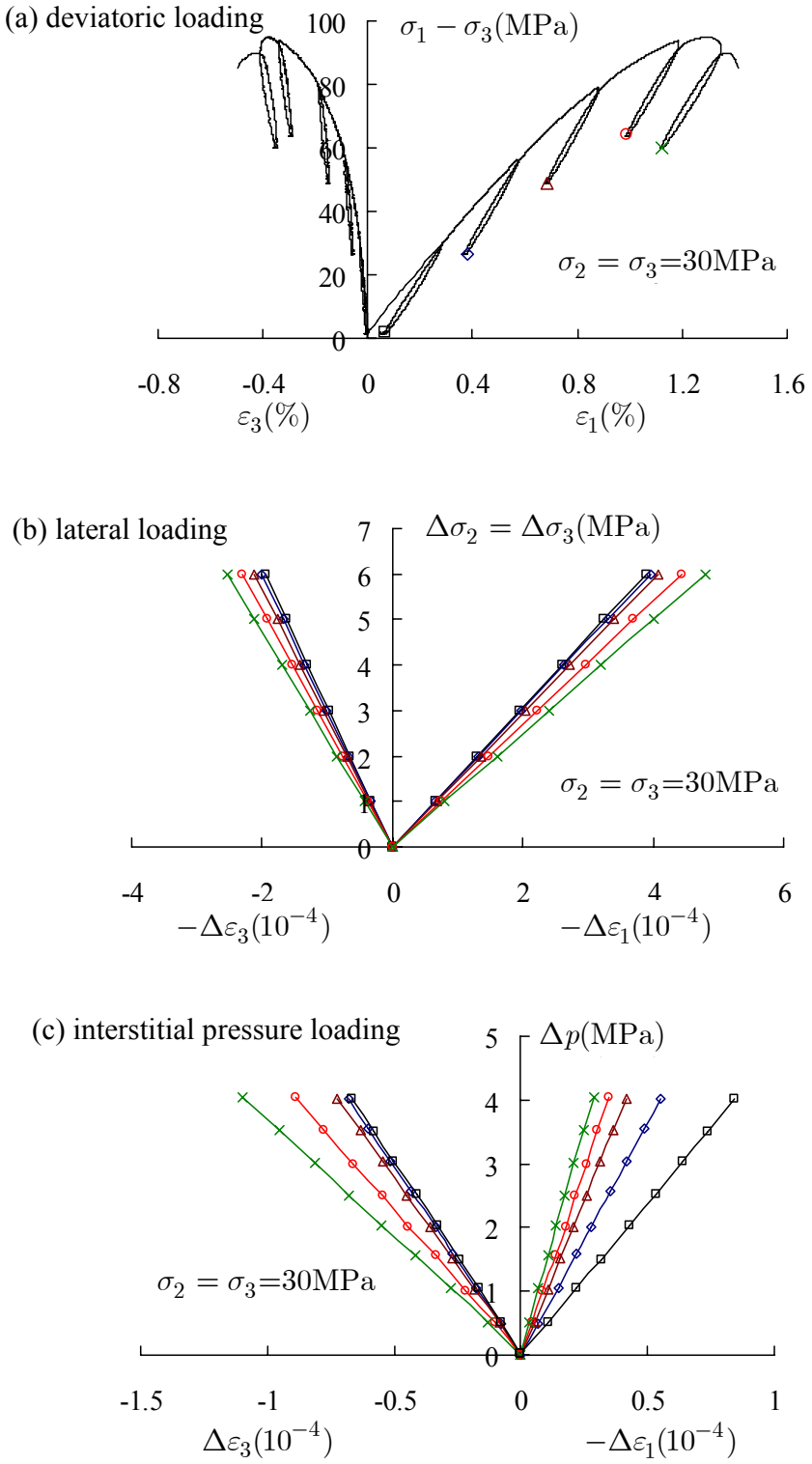

Fig. 2.12 *Triaxial compression test under 30MPa confining pressure: (a) Stress-strain curves, (b) variations of strains due to radial stress, and (c) interstitial pressure variations*

Table 2.4 Evolutions of elastic properties and Biot's coefficients with axial strain in triaxial compression test with the confining pressure of 5MPa

$\varepsilon_1(\%)$	E_1^b (MPa)	E_3^b (MPa)	ν_{13}^b	ν_{31}^b	H_1 (MPa)	H_3 (MPa)	b_1	b_3
0.28	7967	6991	0.2	0.21	15776	15770	0.877	0.777
0.46	10257	6525	0.27	0.22	47793	13099	0.784	0.823
0.66	9358	5727	0.372	0.23	96971	11401	0.756	0.877
0.84	8363	4845	0.501	0.242	122720	9594	0.901	0.997
0.98	6802	3563	0.631	0.256	167630	7182	1.157	1.143

Table 2.5 Evolutions of elastic properties and Biot's coefficients with axial strain in triaxial compression test with the confining pressure of 10MPa

$\varepsilon_1(\%)$	E_1^b (MPa)	E_3^b (MPa)	ν_{13}^b	ν_{31}^b	H_1 (MPa)	H_3 (MPa)	b_1	b_3
0.20	9158	8544	0.16	0.197	20485	26912	0.677	0.544
0.40	10384	8450	0.189	0.195	36386	24991	0.549	0.549
0.61	9907	8094	0.191	0.216	42427	20064	0.572	0.641
0.81	9145	7374	0.234	0.231	56171	16275	0.582	0.732
1.12	8013	5095	0.538	0.243	144370	10881	0.789	0.960

Table 2.6 Evolutions of elastic properties and Biot's coefficients with axial strain in triaxial compression test with the confining pressure of 20MPa

$\varepsilon_1(\%)$	E_1^b (MPa)	E_3^b (MPa)	ν_{13}^b	ν_{31}^b	H_1 (MPa)	H_3 (MPa)	b_1	b_3
0.382	11352	11002	0.177	0.191	43921	44988	0.421	0.412
0.598	11250	10508	0.183	0.196	49165	42698	0.400	0.409
0.879	10313	9899	0.226	0.202	52185	35963	0.395	0.470
1.153	9305	8624	0.285	0.215	74680	22619	0.422	0.641

Table 2.7 Evolutions of elastic properties and Biot's coefficients with axial strain in triaxial

compression test with the confining pressure of 30MPa

$\varepsilon_1(\%)$	E_1^b (MPa)	E_3^b (MPa)	ν_{13}^b	ν_{31}^b	H_1 (MPa)	H_3 (MPa)	b_1	b_3
0.29	11945	11831	0.106	0.191	47380	59883	0.371	0.308
0.59	13457	11652	0.139	0.196	72488	58690	0.326	0.309
0.90	12776	11291	0.154	0.202	96899	55473	0.273	0.313
1.21	12024	10392	0.204	0.215	116860	45150	0.270	0.361
1.35	11188	9586	0.235	0.191	138710	36662	0.276	0.412

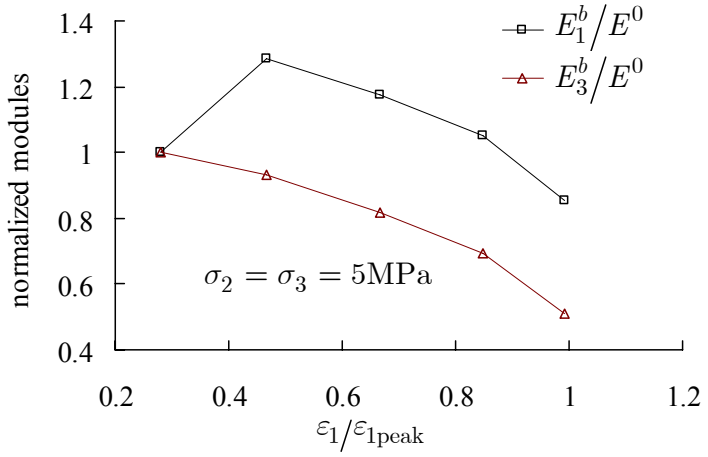

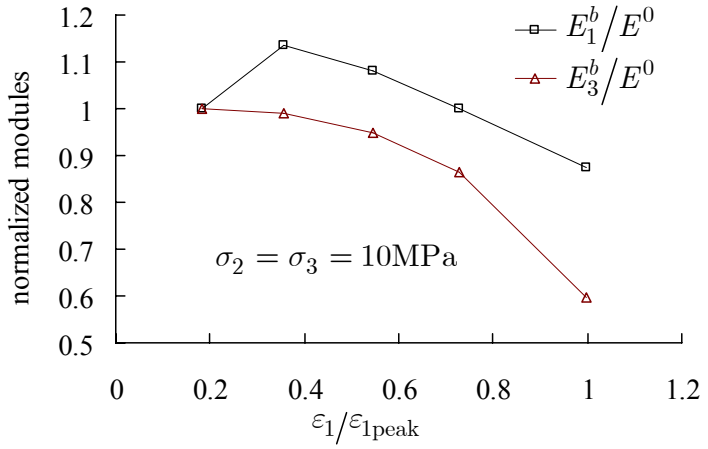

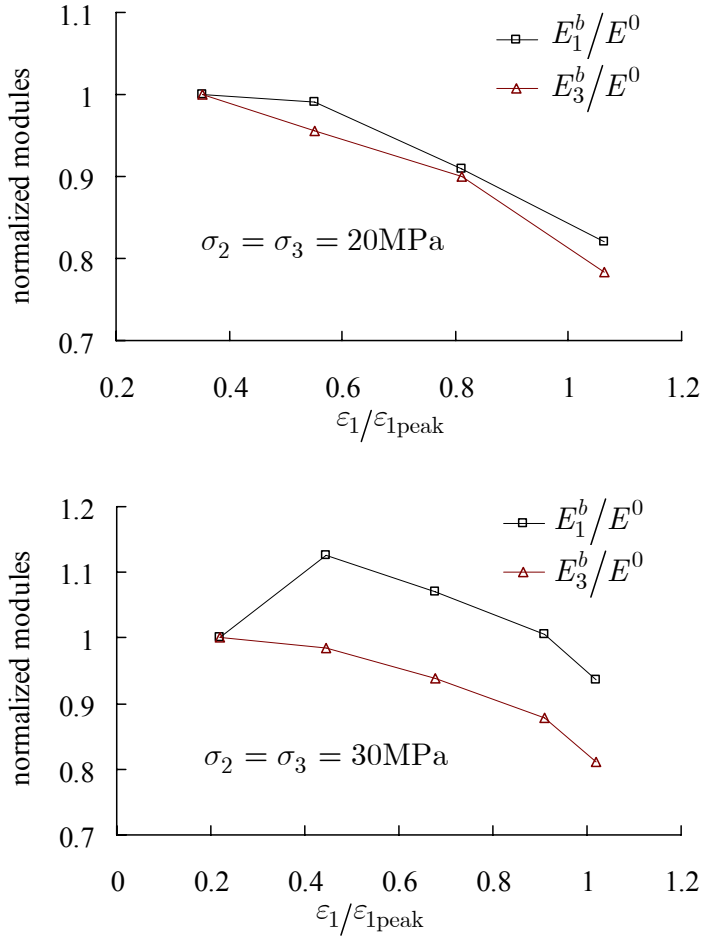

Fig. 2.13 *Evolutions of elastic modulus in axial and radial directions with relative axial strain in triaxial compression tests with different confining pressures for the determination of Biot's coefficients*

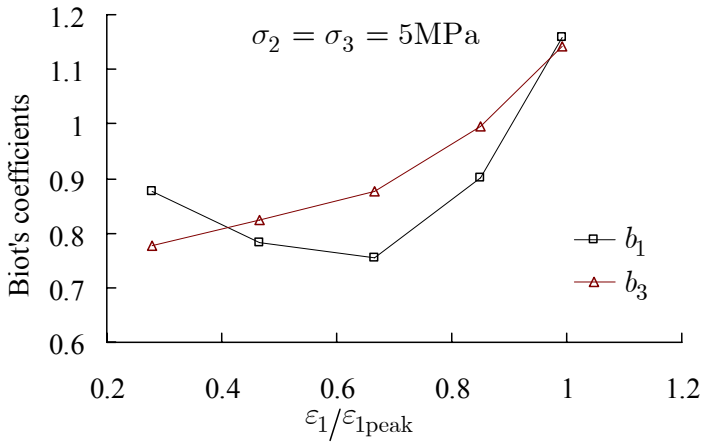

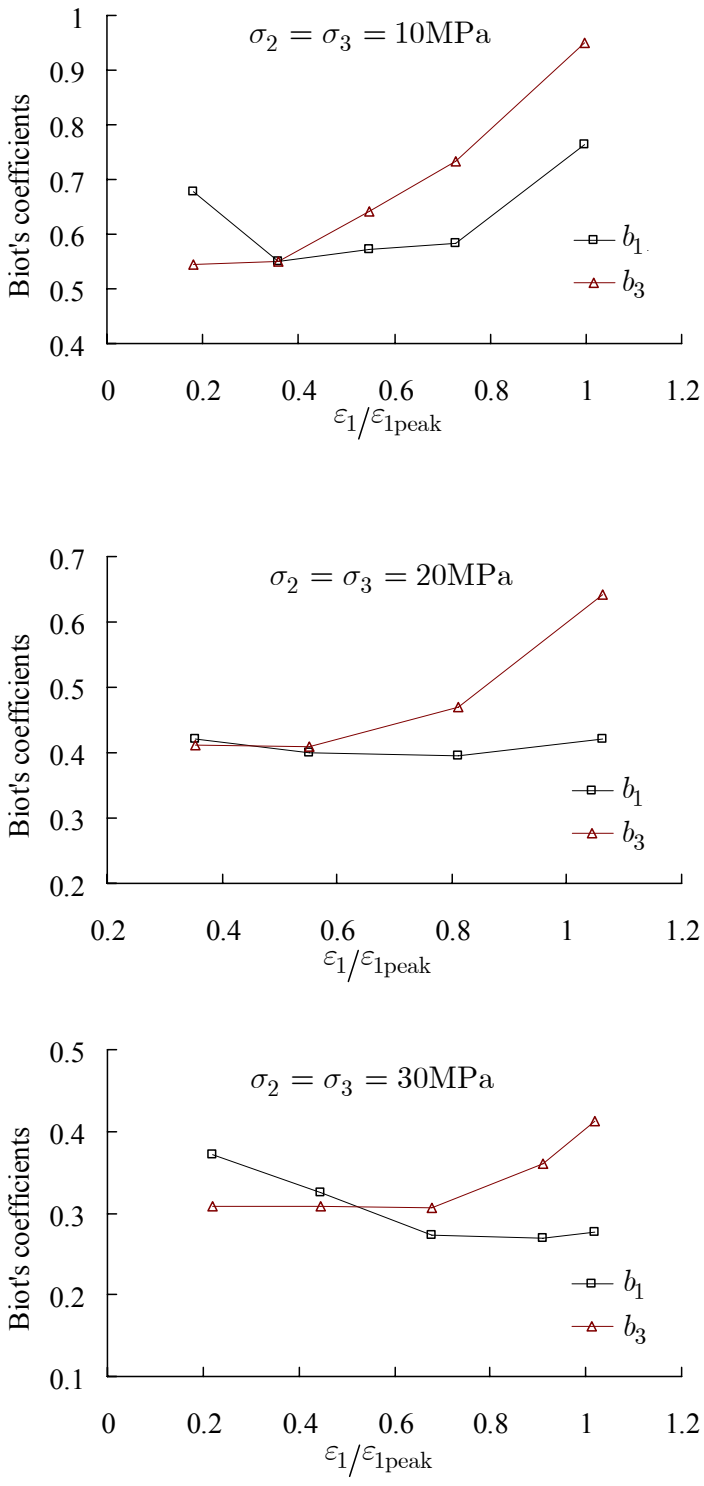

Fig. 2.14 *Evolutions of Biot's coefficients in axial and radial directions with relative axial strain for different confining pressures*

2.4.3 Permeability evolution

The emphasis of this work is the investigation of poroelastic properties of saturated sandstone undergoing induced anisotropic damage. However, the poroelastic coupling is inherently related to fluid flow in pore space, which is controlled by rock permeability. On the other hand, the induced damage will affect not only elastic and poroelastic properties of rock but also the permeability. As mentioned in the introduction section, a number of previous works have shown that the permeability can significantly change due to the evolution of microstructure of rocks such as nucleation, propagation and closure of microcracks, onset of shear and compaction bands (Zhu and Wong 1997a, Suzuki et al. 1998, Schulze et al. 2001, Souley et al. 2001, Bossart et al. 2002, Wang and Park 2002, Oda 2002). Therefore, for the completeness of the present work, the variation of permeability during triaxial compression tests is here investigated in addition to the poroelastic properties.

2.4.3.1 Test procedure

Two different experimental techniques are usually used for the measurement of rock permeability: the steady-state flow (or permanent regime) method and pulse test (or transient regime) technique. The choice of the one or the other method mainly depends on the range of permeability to be determined. Generally, for materials with relatively higher permeability (say $>10^{-16}m^2$), it is easily to reach the permanent flow regime in the sample and the steady-state flow is preferred. On the opposite side, for rocks with low and very low permeability, the set up of the steady state flow needs a very long time period and it is then technically impossible to directly estimate the permeability. An indirect method, the most largely used one is called the pulse test method (Brace, 1968b), is needed. The permeability is estimated from pressure evolution with time, using an inverse numerical algorithm.

In the case of the sandstone studied here, its initial permeability is relatively high and estimated as about $10^{-16}\ m^2$. We have then adopted the steady-state flow method. A schematic illustration of the testing procedure is shown in Fig. 2.14. The principle of the test is very simple; it consists in the injection of water from the bottom surface of the sample in order to obtain an incremental variation of the interstitial pressure (Δp) on this surface while keep the pressure at the upper surface constant. When the steady-state flow is established, the pressure

variation (Δp) and the injection flow rate, noted as Q $(\mathrm{m}^3 \cdot \mathrm{s}^{-1})$, become constant in time. Applying the classic Darcy's law, the intrinsic permeability (noted as k) can be easily deduced by:

$$k(m^2) = \frac{Q\mu L}{\Delta p A} \tag{2.2}$$

The coefficient, μ, denotes the dynamic fluid viscosity coefficient and equals to μ=1.005×10^{-3} Pa·s under the room temperature; L and A are the length and cross section of the sample respectively.

Note that the objective here is to study the evolution of permeability with the level of deviatoric stress (then of induced damage). Therefore, unloading-reloading cycles are performed for different levels of deviatoric stress during triaxial compression tests with different confining pressures. And the permeability is measured at the beginning of unloading and reloading. The average flow rate used is about 0.07ml/min.

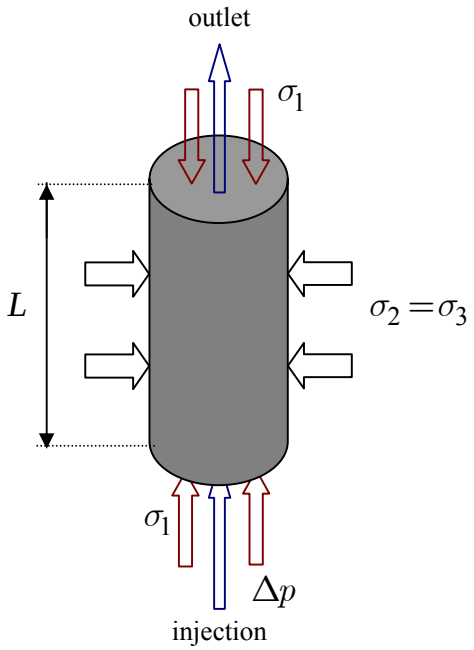

Fig. 2.14 *Schematic illustration of testing principle for permeability*

2.4.3.2 Test results

The typical stress strain curves obtained in these triaxial tests for permeability measurement are plotted in Fig. 2.15. These stress-strain curves complete those obtained in the monotonous tests and cyclic tests for Biot's coefficient determination presented in the previous sections. In an overall way, these results confirm the general trends obtained in the previous tests concerning the mechanical behaviour of the sandstone. We observe again the induced anisotropic degradation of elastic modulus, transition from volumetric compressibility to dilatancy and the transition from brittle to ductile behaviour with the confining pressure.

In Fig. 2.15, we also show the variations of the intrinsic permeability with the relative axial strain ($\varepsilon_1 / \varepsilon_1^{peak}$) during the triaxial compression tests with the four confining pressures of 5, 10, 20 and 30MPa. Note that only the permeability in the axial direction is measured in the present work due to technical limitation of the device. However, as the induced microcracks are mainly oriented in the axial direction, the permeability in this direction should be more significantly affected than that in the radial direction. From these curves for the different confining pressures, the most important feature of the axial permeability variation seems to be that the permeability decreases quite quickly during the two first stages of rock deformation, say the closure phase of initial bedding planes and microcracks and the linear elastic deformation phase. After then, with the onset of propagation of induced microcracks, the diminution of permeability is attenuated and an increase of permeability is even observed for low confining pressures. Such results seem to indicate that due to the relatively high value of the initial permeability of the sandstone, the variation of the permeability is more sensitive to the closure of bedding planes and initial microcracks and defeats than to the growth of induced damage. The effect of induced damage on the sandstone permeability becomes significant only at the late stage of induced damage approaching to the coalescence of microcracks. At the diffuse regime of damage, the sandstone permeability is very moderately affected. Further, it is also interesting to look at the permeability variation during the unloading-reloading cycle. The permeability increases slightly during the unloading stage and then decreases more significantly during the reloading stage. The permeability at the end of unloading does not recover its initial value before loading. All these phenomena indicate that the diminution of permeability is related to some irreversible deformation process.

In addition, we have also looked at the correlation between the permeability change and

the cumulated volume strain ε_v and applied mean stress σ_m at each point of unloading. The obtained variation curves are plotted in Fig. 2.15 and Fig. 2.16. We can see that the axial permeability first decreases with the volumetric compressive strain. After the transition point of compaction-dilatancy, the axial permeability decreases with smaller rate and finally begins to increase. Therefore, there exists some correlation between permeability change and volumetric deformation. However, the permeability increase with the volumetric dilatancy is not as significantly as in priori expected. On the other hand, it seems that the permeability continuously decreases with applied effective mean stress.

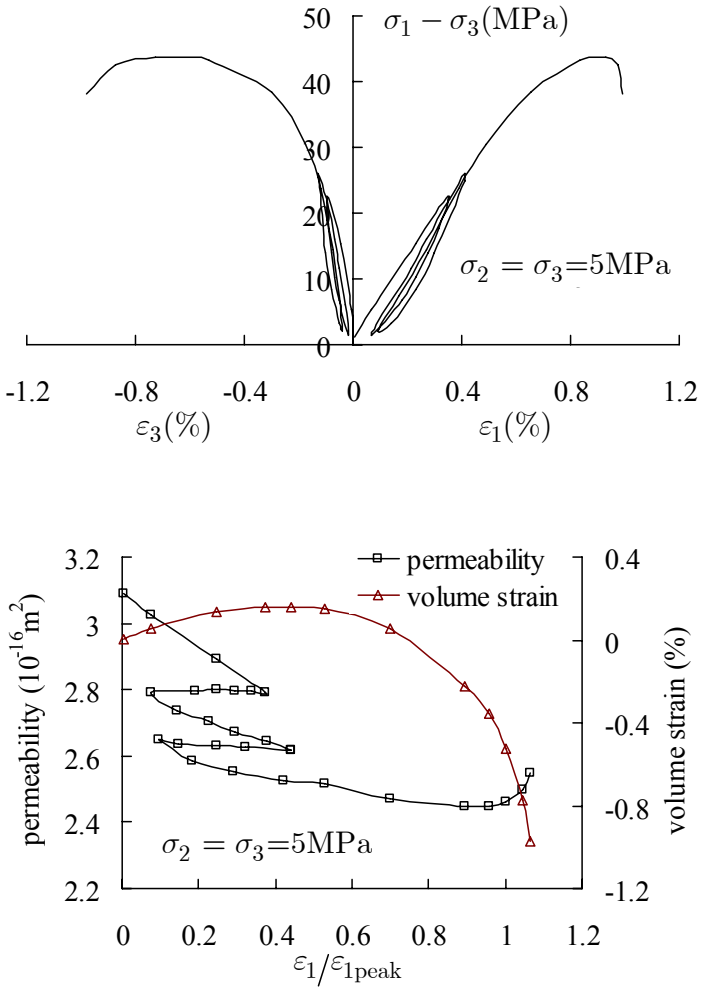

(a) Confining pressure 5MPa

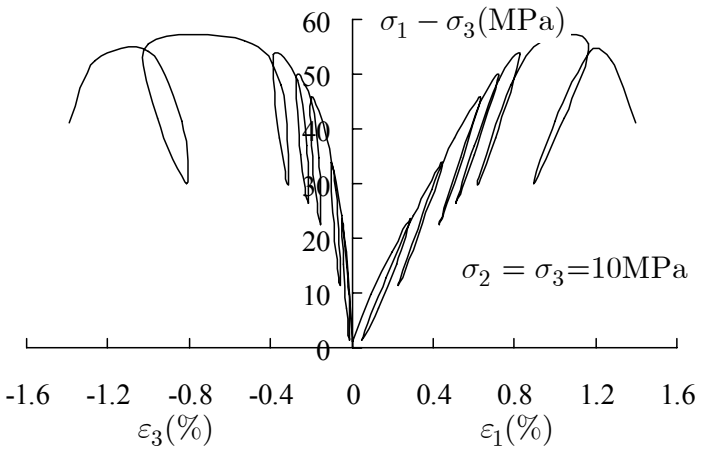

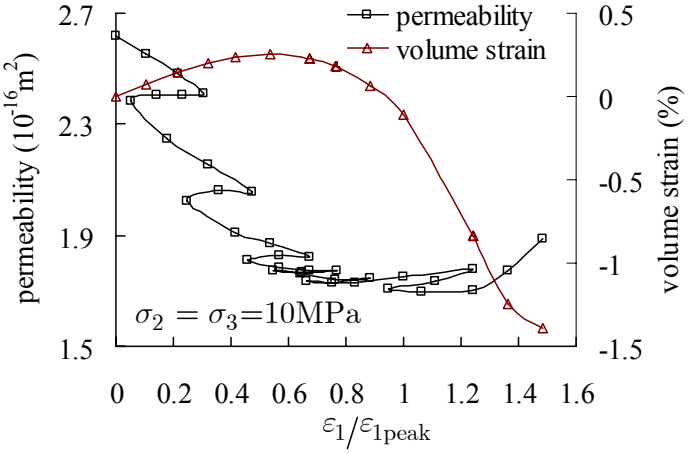

(b) Confining pressure 10MPa

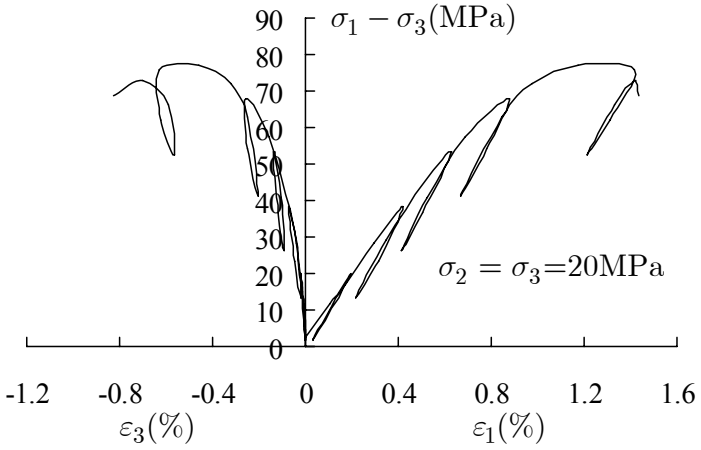

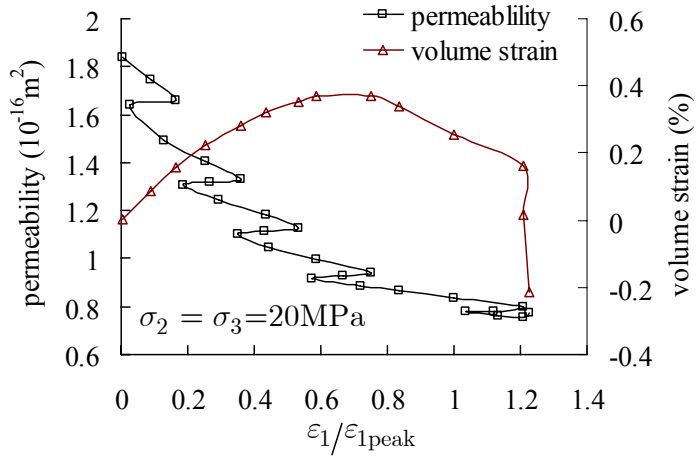

(c) Confining pressure 20MPa

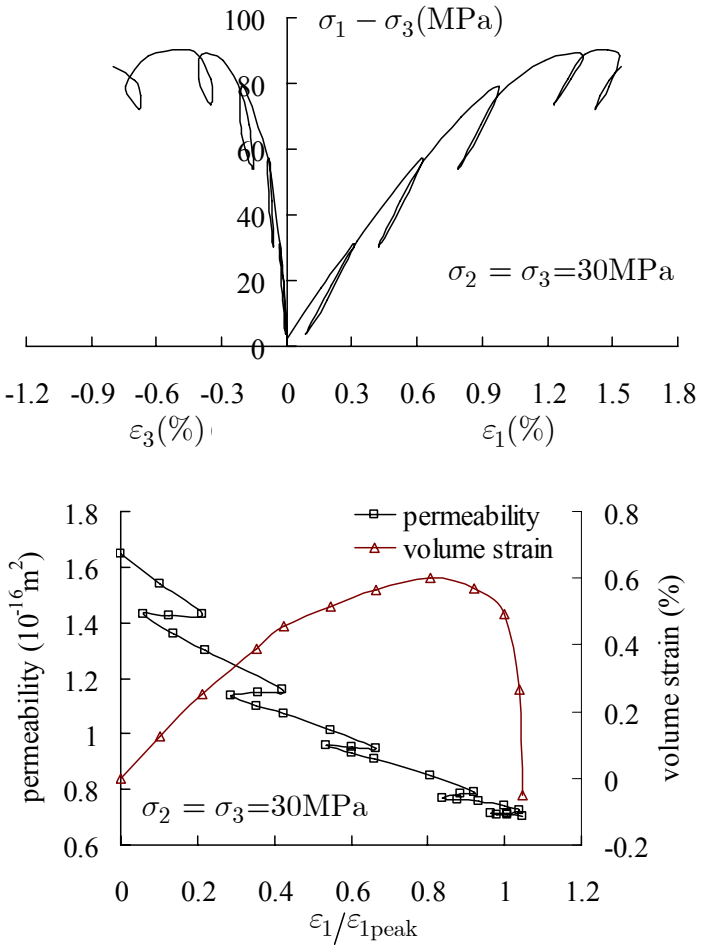

(d) Confining pressure 30MPa

Fig. 2.15 *Stress-strain curves, variations of permeability and volumetric deformation during triaxial tests for permeability measurement*

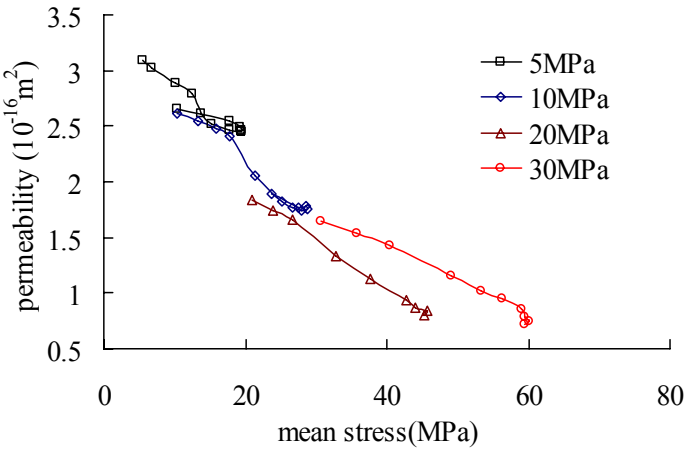

Fig. 2.16 *Relationship between intrinsic permeability and effective mean stress during triaxial compression tests with different confining pressure*

2.5 Conclusions

In this chapter, we have investigated the mechanical behaviour, Biot's coefficient and intrinsic permeability of sandstone in saturated conditions and with induced anisotropic damage. Hydrostatic compression tests and three series of triaxial tests with different confining pressures have been performed. The studied sandstone exhibits a slight structural anisotropy due to the existence of parallel bedding planes and initial microcracks. Under compressive stresses, these initial defeats are progressively closed leading to non linear stress strain relations. Under applied deviatoric stress and after certain threshold, there is propagation of existing microcracks and nucleation of new ones. The propagation of microcracks is mainly oriented in the axial direction in conventional triaxial compression tests. The main consequences of the induced damage include the deterioration of elastic properties and induced anisotropy, strong sensitivity to confining pressure, transition from volumetric compressibility to dilatancy, anisotropic variation of Biot's coefficient and also intrinsic permeability. There is also the transition from brittle to ductile behaviour due to the diminution of induced damage rate under higher confining pressure. The oriented induced damage affects Biot's coefficient much more significantly in the axial direction than in the lateral one. There exists also some

correlation between the permeability change and volumetric deformation as well as effective mean stress. However, the influence of volumetric dilatancy on the permeability increase is not very significant during the diffuse regime of damage. It seems that the induced damage will affect the rock permeability in a significant way only after the coalescence of microcracks. This important feature needs further investigations. In the following chapters, based on the present experimental work, it is proposed to formulate an anisotropic poroelastic damage model in order to take into account the coupling between rock deformation and the evolutions of poroelastic properties and permeability.

Chapter 3 Modelling of anisotropic mechanical behaviours

In this chapter, a coupled anisotropic plastic damage model is formulated within the discrete thermodynamic framework proposed by Zhu et al. (2008c). It is assumed that macroscopic plastic strains in cohesive-frictional geomaterials are mainly induced by frictional sliding along weakness planes and that the evolution of damage is related to growth of weakness planes physically in connection with propagation of microcracks. For determination of plastic flow and damage evolution, a modified Coulomb-type plastic yield function capable of taking into account material hardening/softening behaviour and a Mazars-type damage criterion are proposed for each family of weakness planes. A non-associated plastic flow is used to model volumetric dilatancy of geomaterials. Finally, the developed model is applied to simulate the mechanical behaviour of dry Vosges sandstone under different compressive loading paths. Comparisons between numerical predictions and experimental data are presented. The evolution and distribution in orientation of discrete plastic hardening variables and damage variables are discussed.

3.1 Presentation of model

3.1.1 Isotropic thermodynamic framework

We first briefly review the thermodynamic framework of isotropic coupled plasticity-damage formulation using internal variables (Ju, 1989; Chiarelli et al., 2003; Shao et al., 2006, and others). Assume that the total macroscopic strain admits the following two-part decomposition

$$\boldsymbol{\varepsilon} = \boldsymbol{\varepsilon}^e + \boldsymbol{\varepsilon}^p, \quad \mathrm{d}\boldsymbol{\varepsilon} = \mathrm{d}\boldsymbol{\varepsilon}^e + \mathrm{d}\boldsymbol{\varepsilon}^p, \tag{3.1}$$

where ε^e and ε^p are elastic strain and plastic strain, respectively. Under the assumption of small strains and isothermal condition, the internal variables involved are then isotropic scalar-valued damage variable d_0, plastic strain tensor ε^p (equivalently elastic strain ε^e) and isotropic plastic hardening variable γ_0^p. The Helmholtz free energy of damaged materials are generally formulated as a sum of an elastic free energy term $\psi^e\left(\varepsilon^e, d_0\right)$ and a plastic hardening energy term $\psi^p\left(\gamma_0^p, d_0\right)$

$$\psi = \frac{1}{2}\varepsilon^e : \mathbb{C}(d_0) : \varepsilon^e + \psi^p(\gamma_0^p, d_0). \tag{3.2}$$

In the above equation, $\mathbb{C}(d_0)$ denotes the fourth order effective elastic stiffness tensor of damaged materials. When assuming that the studied material is elastic, isotropic and undamaged in its initial state, its initial elastic stiffness tensor, denoted by $\mathbb{C}^0$ can be characterized by two elastic constants, for example, the bulk modulus k^0 and the shear modulus μ^0. According to the second principle of irreversible thermodynamics, the Clausius-Duhem inequality requires $\boldsymbol{\sigma} : \dot{\varepsilon} - \dot{\psi} \geq 0$, from which is derived

$$\left(\boldsymbol{\sigma} - \frac{\partial \psi}{\partial \varepsilon^e}\right) : \dot{\varepsilon} + \frac{\partial \psi}{\partial \varepsilon^e} : \dot{\varepsilon}^p - \frac{\partial \psi}{\partial d_0}\dot{d}_0 - \frac{\partial \psi^p}{\partial \gamma_0^p}\dot{\gamma}_0^p \geq 0. \tag{3.3}$$

Due to the fact that the above inequality must hold for any combination of the increments $\dot{\varepsilon}$, $\dot{\varepsilon}^p$, $\dot{d}_0$ and $\dot{\gamma}_0^p$, it follows the macroscopic stress-strain relation

$$\boldsymbol{\sigma} = \frac{\partial \psi}{\partial \varepsilon^e} = \mathbb{C}(d_0) : \left(\varepsilon - \varepsilon^p\right), \tag{3.4}$$

as well as the conjugate thermodynamics forces respectively associated with the damage variable d_0 and the plastic hardening variable γ_0^p. For completeness, a plastic yield function, a damage criterion and a plastic hardening law are required for determination of plastic flow and damage evolution during loading process,. For geomaterials such as rocks and soils, a non-associated plastic flow is also necessary for description of volumetric dilatancy.

3.1.2 Discrete thermodynamic framework

Many laboratory investigations have clearly shown plastic deformation and damage propagatation in geomaterials essentially nucleate and develop at some preferred weakness sliding planes (Hallbauer et al., 1973; Tapponier and Brace, 1976; Wong, 1985; Moore and Lockner, 1995). In view of this orientation dependent feature, the commonly used thermodynamic framework of isotropic plastic damage formulation seems inappropriate for proper description of coupled anisotropic plastic damage behaviors.

In the present work, we adopt the discrete thermodynamic framework recently proposed by Zhu et al. (2008c) for anisotropic formulations. Note that geometrically, each weakness sliding plane (WSP) can be identified by a unit vector normal to its plane (Fig. 3.1) and all planes with a same normal vector may be included into the same family. Without loss of generality, this normal vector is denoted by $\underline{n}$.

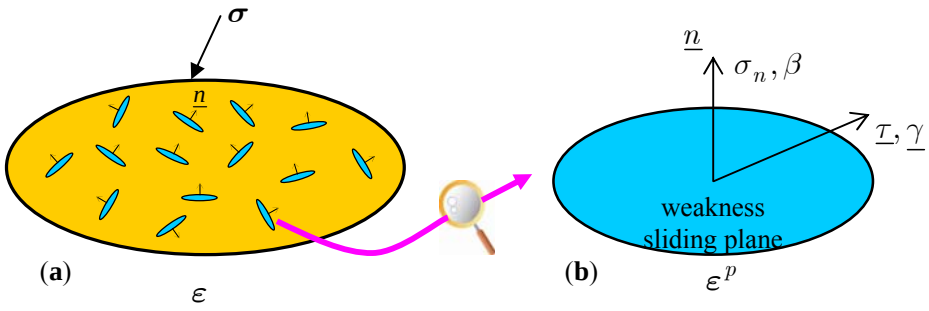

Fig. 3.1: *(a) Representative volume element (RVE),*
(b) Schematic representation of a weakness sliding plane

When ignoring interactions between different families of WSPs, the total plastic strain in a representative volume element (see Fig.3.1) can be considered as a superimposed consequence of all families of WSPs. For general distribution of WSPs, the macroscopic total plastic strain can be also generalized into an orientational integration over the surface of a half unit sphere $\mathcal{S}^+$.

$$\varepsilon^p = \int_{\mathcal{S}^+} \varepsilon^p(\underline{n}) \mathrm{d}S \tag{3.5}$$

Moreover, the planar geometry of the weakness planes allows us to decompose the local plastic

strain tensor $\boldsymbol{\varepsilon}^p(\underline{n})$ into a normal part and a tangential part

$$\boldsymbol{\varepsilon}^p(\underline{n}) = \beta(\underline{n})\underline{n} \otimes \underline{n} + \underline{\gamma}(\underline{n}) \otimes^s \underline{n} \tag{3.6}$$

where $\beta(\underline{n})=\mathrm{tr}\boldsymbol{\varepsilon}^p(\underline{n})$ is defined as the normal strain component and $\underline{\gamma}(\underline{n})$ as the shear strain vector related to the family of WSPs of unit normal $\underline{n}$. Similarly, the isotropic scalar damage variable d_0 and the plastic hardening variable γ_0^p involved in isotropic plasticity-damage formulation can be replaced by an orientation-dependent functions (ODF) $d(\underline{n})$ and $\gamma^p(\underline{n})$, respectively. Note that the damage distribution function $d(\underline{n})$ is often combined with the second and/or fourth order fabric tensor $\underline{n} \otimes \underline{n}$ and $\underline{n} \otimes \underline{n} \otimes \underline{n} \otimes \underline{n}$ to define the classic second- and fourth rank tensorial damage variables $\boldsymbol{D}$ and $\mathbb{D}$,

$$\boldsymbol{D} = \int_{\mathcal{S}^+} d(n) n \otimes n \mathrm{d}S \tag{3.7}$$

$$\mathbb{D} = \int_{\mathcal{S}^+} d(n) n \otimes n \otimes n \otimes n \mathrm{d}S \tag{3.8}$$

In addition, inspired by classic isotropic plasticity theory, plastic hardening variable associated with a general family of defects with normal vector $\underline{n}$ is defined as:

$$\gamma^p(\underline{n}) = \int \sqrt{2\dot{\boldsymbol{\varepsilon}}^p(\underline{n}) : \mathbb{T} : \dot{\boldsymbol{\varepsilon}}^p(\underline{n})} \tag{3.9}$$

From numerical viewpoints, the Gauss-type discretization procedure has been widely adopted for numerical approximation of the orientational integration, for instance Stroud (1971), Bazant and Oh (1986). In the work by Zhu et al. (2008c), an integration scheme with 15 equally-weighted integration points distributed over the surface of a unit sphere in 3D Cartesian coordinates system has been used (see Fig. a.1), in which each orientation vector defined by an integration point and the original point corresponds to one family of weakness sliding planes. Isotropy and discretization characteristics of this integration scheme have been studied in detail by Elata and Rubin (1995) and Zhu et al. (2006, thesis). The components of these 15 orientation vectors denoted by $\underline{n}^r, r = 1,\cdots,15$ are provided in Appendix A. With these 15 orientation vectors, the discrete form of the above integral formulations is given as follows

$$\varepsilon^p = \sum_{r=1}^{15} \varpi^r \left(\beta^r \underline{n}^r \otimes \underline{n}^r + \underline{\gamma}^r \otimes^s \underline{n}^r \right), \tag{3.10}$$

$$\boldsymbol{D} = \sum_{r=1}^{15} \varpi^r d^r \underline{n}^r \otimes \underline{n}^r, \tag{3.11}$$

$$\mathbb{D} = \sum_{r=1}^{15} \varpi^r d^r \underline{n}^r \otimes \underline{n}^r \otimes \underline{n}^r \otimes \underline{n}^r. \tag{3.12}$$

where, without loss of generality, we have used ϖ^r to represent the integration weight related to the integration direction $\underline{n}^r$. For the current 15-point integration scheme, one has $\varpi^r = \frac{1}{15}$ for all considered families.

It has to be pointed out that after discretization, we have now 15 local plastic strain tensor $\varepsilon^{p,r}$, 15 discrete internal damage variables d^r, and 15 plastic hardening variables $\gamma^{p,r}$. When representing all 15 discrete damage variables d^r by the set $\mathbf{d}$ and $\gamma^{p,r}$ by the set $\boldsymbol{\gamma}^p$, the Helmholtz free energy (3.2) is rewritten in the form

$$\psi = \frac{1}{2} \varepsilon^e : \mathbb{C}(\mathbf{d}, \mathbf{n}) : \varepsilon^e + \psi^p \left(\boldsymbol{\gamma}^p, \mathbf{d} \right). \tag{3.13}$$

It follows the Clausius-Duhem inequality

$$\sum_{r=1}^{15} \varpi^r \left(\boldsymbol{\sigma} : \dot{\varepsilon}^{p,r} - \frac{\partial \psi}{d^r} \dot{d}^r - \frac{\partial \psi}{\gamma^{p,r}} \dot{\gamma}^{p,r} \right) \geq 0. \tag{3.14}$$

Above, use has been made of the stress-strain relation (3.4). Due to the fact that (3.14) must hold for any combination of $\dot{\varepsilon}^{p,r}$, $\dot{d}^r$ and $\dot{\gamma}^{p,r}$, one has

$$\boldsymbol{\sigma} : \dot{\varepsilon}^{p,r} - \frac{\partial \psi}{d^r} \dot{d}^r - \frac{\partial \psi}{\gamma^{p,r}} \dot{\gamma}^{p,r} \geq 0, \tag{3.15}$$

from which the thermodynamic force associated with the discrete damage and plastic hardening variables d^r and $\gamma^{p,r}$ are derived as follows

$$F^{d^r} = -\frac{\partial \psi}{d^r}, \quad \alpha^{p,r} = \frac{\partial \psi}{\gamma^{p,r}}, \tag{3.16}$$

and we also find that it is the macroscopic stress tensor $\boldsymbol{\sigma}$ that controls the plastic flow of the local plastic tensor $\dot{\varepsilon}^{p,r}$, in other words, $\boldsymbol{\sigma}$ servers as a thermodynamic force common to all WSP families.

The normal and tangential parts of the macroscopic stress tensor $\boldsymbol{\sigma}$ with respect to one WSP family of the unit normal $\underline{n}$, denoted by $\boldsymbol{\sigma}_n$ and $\boldsymbol{\sigma}_t$, can be obtained respectively by projection of the stress tensor $\boldsymbol{\sigma}$ onto $\underline{n}$

$$\boldsymbol{\sigma}_n(\underline{n}) = \mathbb{N}(\underline{n}) : \boldsymbol{\sigma}, \quad \boldsymbol{\sigma}_t(\underline{n}) = \mathbb{T}(\underline{n}) : \boldsymbol{\sigma} \tag{3.17}$$

in which both two fourth order tensorial operators $\mathbb{N}$ and $\mathbb{T}$ are function of the unit normal vector $\underline{n}$ and expressed as follows

$$N_{ijkl} = n_i n_j n_k n_l \tag{3.18}$$

$$T_{ijkl} = \frac{1}{2}\left(\delta_{ik} n_j n_l + \delta_{il} n_j n_k + \delta_{jk} n_i n_l + \delta_{jl} n_i n_k - 4 n_i n_j n_k n_l\right) \tag{3.19}$$

For later use in plastic formulations, the following stress invariants based on $\boldsymbol{\sigma}_n$ and $\boldsymbol{\sigma}_t$ are defined

$$\sigma_n = \sqrt{\boldsymbol{\sigma}_n : \boldsymbol{\sigma}_n} = \sqrt{\boldsymbol{\sigma} : \mathbb{N} : \boldsymbol{\sigma}} \tag{3.20}$$

$$\sigma_t = \sqrt{\frac{1}{2}\boldsymbol{\sigma}_t : \boldsymbol{\sigma}_t} = \sqrt{\frac{1}{2}\boldsymbol{\sigma} : \mathbb{T} : \boldsymbol{\sigma}} \tag{3.21}$$

3.1.3 Characterization of plastic flow

This part is devoted to develop the plastic yield and potential function. It is assumed that the material is initially isotropic and that anisotropic plastic deformation is induced by preferential slip in some weakness orientations due to deviatoric stress, in other words, the material anisotropy is stress induced. On the other hand, as discussed in the previous section, the macroscopic stress serves as the thermodynamic force common to all WSP families. Therefore, plastic yield function for all material orientations should take a same form and so does the plastic potential function. In what follows, unless required, the superscript used to prescribe the WSP family will be omitted.

According to many experiments, most geomaterials can be classed into cohesive-frictional materials. A modified Coulomb-type plastic yield function is then used for each family. The plastic yield function for the chosen weakness sliding planes can be formulated with the help of the stress invariants σ_n and σ_t

$$f^p(\sigma_n, \sigma_t, \gamma^p) = \sigma_t + \alpha^p \left(\sigma_n - c_0\right) - \vartheta^p \leq 0\,, \tag{3.22}$$

where c_0 denotes the material inherent cohesion, ϑ^p is used to described isotropic hardening/softening effect within the sliding plane and assumed to takes the form $\vartheta^p = H_1 \gamma^p e^{-a_1 \gamma^p}$ in which H_1 is a model constant and the parameter a_1 controls its kinetics. By virtue of (3.6), the hardening variable γ^p is now updated as:

$$\gamma^p = \int \sqrt{\mathrm{d}\underline{\gamma} \cdot \mathrm{d}\underline{\gamma}}\,, \tag{3.23}$$

which can be interpreted as local cumulated shear strain. The function α^p defines the plastic hardening law and should be dependent on the plastic hardening variable γ^p. For most geomaterials, the following exponential function provides an appropriate simulation

$$\alpha^p = \alpha_f^p - (\alpha_f^p - \alpha_0^p) e^{-a_2 \gamma^p} \tag{3.24}$$

in which α_0^p and α_f^p are the initial and asymptotic values of the hardening function, respectively and the parameter a_2 controls the evolution rate of α^p ranging from α_0^p to α_f^p as γ^p increases.

Some further discussions are addressed upon the yield function (3.22) by comparing with some existing formulations:

- The yield function (3.22) can be rewritten in the standard Coulomb form:

$$f^p(\sigma_n, \sigma_t, \gamma^p) = \sigma_t + \alpha^p \sigma_n - c \leq 0 \tag{3.25}$$

  with $c = \alpha^p c_0 + H_1 \gamma^p e^{-a_1 \gamma^p}$ interpreted as kinetic cohesive strength. In fact, most laboratory experiments have shown that the cohesive strength depends not only on material properties but on loading history as well and that it is mobilized and consumed due to plastic deformation in loading process (Hajiabdolmajid, 2001). The failure process initiates with the growth of microcracks in the direction of maximum shearing and consequently these microcracks weaken the rock by reducing its cohesive strength in its post-peak phase. Therefore, it seems reasonable for the proposed yield function to divide the material cohesive strength into two parts, the

first one is inherent cohesion and the second one is mobilized cohesive strength as a function of the plastic hardening variable γ^p.

- Noticing that σ_t equals to $\left\|\underline{\tau}\right\|$ with $\underline{\tau} = \boldsymbol{\sigma}\cdot\underline{n}\cdot\left(\boldsymbol{\delta}-\underline{n}\otimes\underline{n}\right)$ defined as the tangential part of the traction vector $\boldsymbol{\sigma}\cdot\underline{n}$, the yield function is then equivalent to the following form:

$$f^p(\sigma_n,\sigma_t,\gamma^p) = \left\|\underline{\tau}-\vartheta^p\underline{t}\right\| + \alpha^p\left(\sigma_n - c_0\right) \le 0 \tag{3.26}$$

with $\underline{t} = \frac{1}{\sigma_t}\boldsymbol{\sigma}\cdot\underline{n}\cdot(\boldsymbol{\delta}-\underline{n}\otimes\underline{n})$. In the above form, $\vartheta^p\underline{t}$ plays a role of back stress hardening/softening within the sliding plane.

For geomaterials, a non-associated plastic flow rule is usually necessary. The following form of the plastic potential similar to the plastic yield function (3.22) is used here:

$$g^p\left(\sigma_t,\sigma_n,\gamma^p\right) = \sigma_t + \eta^p\sigma_n = 0 \tag{3.27}$$

where η^p is defines as a coefficient describing plastic volumetric strain in undamaged state, which is induced by plastic shearing within the weakness planes. In order to describe the transition from plastic compressibility to dilatancy in geomaterials η^p is defined as an increasing function of plastic hardening variable γ^p and expressed as follows:

$$\eta^{p,r} = \eta_f^p - \left(\eta_f^p - \eta_0^p\right)e^{-a_3\gamma^p} \tag{3.28}$$

Similar to the classic plasticity theory, the current value of η^p is usually called as *local plastic dilatancy coefficient*, the two parameters η_0^p and η_f^p denote the initial and asymptotic value of dilatancy coefficient, respectively, and it is also assumed for both η_0^p and η_f^p to take the same values for all chosen families. The parameter a_3 controls the evolution rate ranging from η_0^p to η_f^p.

The plastic flow rule and loading-unloading condition are respectively described by

$$\mathrm{d}\boldsymbol{\varepsilon}^p = \mathrm{d}\lambda^p\frac{\partial g^p}{\partial\boldsymbol{\sigma}} = \mathrm{d}\lambda^p\left(\underline{t}\otimes^s\underline{n} + \eta^p\underline{n}\otimes\underline{n}\right), \tag{3.29}$$

$$f^p(\sigma_n,\sigma_t,\gamma^p)=0,\quad \mathrm{d}\lambda^p\geq 0,\quad f^p\cdot\mathrm{d}\lambda^p=0\,. \tag{3.30}$$

where $\underline{t}$ is defined as the plastic shear direction. On the other hand, the increment of plastic strain can be derived from the equation (3.6) by differentiation

$$\mathrm{d}\boldsymbol{\varepsilon}^p=\mathrm{d}\beta\underline{n}\otimes\underline{n}+\mathrm{d}\underline{\gamma}\otimes^s\underline{n}\,. \tag{3.31}$$

Comparison of the above equation with (3.29) leads to the increments of the variables β and $\underline{\gamma}$

$$\mathrm{d}\underline{\gamma}=\mathrm{d}\lambda^p\underline{t},\quad \mathrm{d}\beta=\mathrm{d}\lambda^p\eta^p \tag{3.32}$$

It follows finally

$$\mathrm{d}\gamma^p=\mathrm{d}\lambda^p \tag{3.33}$$

The plastic multiplier $\mathrm{d}\lambda^p$ should be determined by accounting for the plastic consistency conditions $f^p=0$ and $\dot{f}^p=0$ of all WSP families. With numerical implementation in mind, it is convenient to rewrite the yield function in strain-based form. The yield function for the family with the unit normal $\underline{n}^r$ is now renewed as

$$f^{p,r}=\left(\boldsymbol{\varepsilon}-\sum_{k=1}^{15}\varpi^k\boldsymbol{\varepsilon}^{p,k}\right):\boldsymbol{\mathcal{C}}(\mathbf{d},\mathbf{n}):\left[\underline{t}^r\otimes^s\underline{n}^r+\alpha^{p,r}\underline{n}^r\otimes\underline{n}^r\right]-c\leq 0 \tag{3.34}$$

In the case of stationary state of damage ($\dot{d}^r=0,\ r=1,\ldots,15$), one obtains the differential formulation of (3.34)

$$\dot{f}^{p,r}=\frac{\partial f^{p,r}}{\partial\boldsymbol{\varepsilon}}:\dot{\boldsymbol{\varepsilon}}+\sum_{k=1}^{15}\varpi^k\frac{\partial f^{p,r}}{\partial\boldsymbol{\varepsilon}^{p,k}}:\dot{\boldsymbol{\varepsilon}}^{p,k}+\frac{\partial f^{p,r}}{\partial\alpha^{p,r}}\frac{\partial\alpha^{p,r}}{\partial\gamma^{p,r}}\dot{\gamma}^{p,r}=0 \tag{3.35}$$

When the following matrix of coefficients $[\mathbf{M}^p]_{15\times 15}$ is introduced

$$M^p_{IJ}=-\varpi^J\frac{\partial f^{p,I}}{\partial\boldsymbol{\varepsilon}^{p,J}}:\frac{\partial g^{p,J}}{\partial\boldsymbol{\sigma}}-\frac{\partial f^{p,I}}{\partial\gamma^{p,I}}\frac{\partial g^{p,I}}{\partial\sigma_t^I}\delta_{IJ}\,, \tag{3.36}$$

the system to be solved for determination of plastic multipliers for all considered families is then expressed in the following form:

$$[\mathbf{M}^p]\left\{\mathrm{d}\lambda^p\right\}=\left\{\frac{\partial f^p}{\partial\boldsymbol{\varepsilon}}\right\}:\dot{\boldsymbol{\varepsilon}} \tag{3.37}$$

It follows the column of plastic multipliers containing all sliding planes under consideration

$$\left\{\mathrm{d}\lambda^p\right\} = [\mathbf{M}^p]^{-1}\left\{\frac{\partial f^p}{\partial \boldsymbol{\varepsilon}}\right\} : \dot{\boldsymbol{\varepsilon}}\,. \tag{3.38}$$

The rate form of stress-strain relation in stationary damage state reads

$$\dot{\boldsymbol{\sigma}} = \mathbb{C}(\mathbf{d},\mathbf{n}) : \left(\dot{\boldsymbol{\varepsilon}} - \sum_{r=1}^{15} \varpi^r \dot{\boldsymbol{\varepsilon}}^{p,r}\right) \tag{3.39}$$

Finally, the tangential elastoplastic operator is obtained by combination of (3.31), (3.38) and (3.39)

$$\mathbb{C}^{ep}\left(\boldsymbol{\gamma}^p, \mathbf{d}, \mathbf{n}\right) = \mathbb{C}(\mathbf{d},\mathbf{n}) - \left\{\varpi\mathbb{C} : \frac{\partial g^p}{\partial \boldsymbol{\sigma}}\right\}^T [\mathbf{M}^p]^{-1}\left\{\frac{\partial f^p}{\partial \boldsymbol{\varepsilon}}\right\} \tag{3.40}$$

where the component of the column matrix $\left\{\varpi\mathbb{C} : \dfrac{\partial g^p}{\partial \boldsymbol{\sigma}}\right\}^T$ is $\varpi^r\mathbb{C} : \dfrac{\partial g^{p,r}}{\partial \boldsymbol{\sigma}}$.

3.1.4 Characterization of damage flow

In this study, we are interested in the case of the solid matrix weaken by weakness sliding planes in compression regime and we neglect unilateral effects related to opening/closure of defect planes. In the classic isotropic damage theory using one scalar damage variable d_0, let $k(d_0)$ and $\mu(d_0)$ being the bulk and shear modulus of damaged material, respectively, their evolution with damage growth generally takes following linear form

$$k(d) = k^0(1-\kappa_1 d_0), \quad \mu(d) = \mu^0(1-\kappa_2 d_0) \tag{3.41}$$

where the parameters κ_1 and κ_2 are used to control the degradation rate of the bulk and shear modulus, respectively. Correspondingly, the effective elastic stiffness tensor of damaged material is written in the form:

$$\mathbb{C}(d_0) = 3k^0(1-\kappa_1 d_0)\mathbb{J} + 2\mu^0(1-\kappa_2 d_0)\mathbb{K} = \mathbb{C}^0 - 3k^0\kappa_1 d_0\mathbb{J} - 2\mu^0\kappa_2 d_0\mathbb{K} \tag{3.42}$$

where $\mathbb{C}^0$ denotes the initial elastic tensor of undamaged (sound) material. The two fourth order isotropic tensors $\mathbb{J}$ and $\mathbb{K}$, verifying the relation $\mathbb{J}+\mathbb{K}=\mathbb{I}$, have the components

$$I_{ijkl} = \frac{1}{2}\left(\delta_{ik}\delta_{jl} + \delta_{il}\delta_{jk}\right), \quad \text{and} \quad J_{ijkl} = \frac{1}{3}\delta_{ij}\delta_{kl} \tag{3.43}$$

where $\mathbb{I}$ is the fourth order identity tensor. In the case of random distribution of weakness sliding planes, the damage state is generally anisotropic in nature due to propagation of microcracks in some preferred orientations. For the description of this anisotropic damage, we have replaced the isotropic damage variable d_0 by the set $\mathbf{d}$ of discrete damage variables. In addition, it is shown that the fourth order tensor $\mathbb{T}(\underline{n})$ is suitable for description of shear behaviors in weakness planes (Walpole, 1981). The isotropic term $(d_0\mathbb{K})$ is thus generalized into the following integral form:

$$d_0\mathbb{K} = \zeta\frac{1}{4\pi}\int_{S^2} d(\underline{n})\mathbb{T}(\underline{n})\mathrm{d}S \tag{3.44}$$

Note that $\frac{1}{4\pi}\int_{S^2}\mathbb{T}(\underline{n})\mathrm{d}S = \frac{2}{5}\mathbb{K}$; it is derived from the consideration of isotropic damage distribution, i.e. $d(\underline{n}) = d_0$ that $\zeta = \frac{5}{2}$, and it follows

$$d_0\mathbb{K} = \frac{5}{2}\frac{1}{4\pi}\int_{S^2} d(\underline{n})\mathbb{T}(\underline{n})\mathrm{d}S \tag{3.45}$$

Similarly, the term $(d_0\mathbb{J})$ can also be approximated by the following integral form

$$d_0\mathbb{J} = \xi\frac{1}{4\pi}\int_{S^2} d(\underline{n})\left[3\mathbb{N}(\underline{n}) - \mathbb{T}(\underline{n})\right]\mathrm{d}S \tag{3.46}$$

Then, it is determined by the same procedure as that for ζ that $\xi = 1.0$. By insertion of (3.45) and (3.46), the effective elastic stiffness tensor $\mathbb{C}$ is finally written in continuous form

$$\mathbb{C}\left(d(\underline{n})\right) = \mathbb{C}^0 - \frac{1}{4\pi}\int_{S^2} d(\underline{n})\left[9\kappa_1 k^0\mathbb{N}(\underline{n}) + (5\kappa_2\mu^0 - 3\kappa_1 k^0)\mathbb{T}(\underline{n})\right]\mathrm{d}S \tag{3.47}$$

and in discrete form:

$$\mathbb{C}\left(\mathbf{d},\mathbf{n}\right) = \mathbb{C}^0 - \sum_{r=1}^{15}\varpi^r d^r\left(9\kappa_1 k^0\mathbb{N}^r + (5\kappa_2\mu^0 - 3\kappa_1 k^0)\mathbb{T}^r\right) \tag{3.48}$$

As aforementioned, damage evolution is physically related to propagation of microcracks and defects in various orientations. In general, the propagation is not uniform in space. Therefore, the induced damage is usually anisotropic. It is assumed that the damage evolution in each sliding plane is completely controlled by plastic shearing within this plane, which

means that interactions between different families are neglected in this version.

Inspired by the damage criterion proposed by Mazars (1986) for concrete, we use the following exponential function as damage criterion

$$f^{\omega,r} = \omega^r - \left[1 - e^{-a_4 \gamma^{p,r}}\right] \leq 0 \tag{3.49}$$

where a_4 is used to control the kinetics of damage evolution.

3.2 Numerical application

The proposed model is now applied to simulate mechanical tests on dry Vosges sandstone reported by Khazraei (1995). We will first present the procedure of parameter determination and then the comparisons between numerical simulation and test data. The evolution of damage variable and plastic hardening variables will also be discussed in triaxial compression tests.

3.2.1 Parameter identification

There are totally 13 parameters involved in the coupled discrete plastic damage model: two elastic constants for initial (undamaged) state of material, E^0 and ν^0; six parameters involved in plastic yield function c_0, a_1,α_f^p,α_0^p, a_2 and H_1; three parameters in plastic potential function η_f^p, η_0^p and a_3; one parameter charactering the damage evolution a_4; and the parameters κ_1 and κ_2 for describing the degradation of the bulk and shear modulus.

These model parameters can be determined from conventional triaxial compression tests and direct shear tests. The initial elastic constants can be identified from cycles of loading-unloading performed during the stage of elastic deformation. From the triaxial compression tests (Khazraei, 1995) with various confining pressure, the average value of the initial Young's modulus and the Poisson's ratio are: $E^0 = 26000\mathrm{MPa}$ and $\nu^0 = 0.26$.

We now discuss how to determine these parameters involved in plastic yield function. Schmertmann and Osterberg (1960) used a special test and curve fitting techniques to study the cohesive and frictional contributions to the strength of cohesive soil sample. Using their testing method, they could isolate the effect of basic frictional strength from the effects of other

variables and obtain the evolution of cohesive and frictional components of strength as a function of strain. Martin and Chandler (1994) conducted a damage controlled test on samples of Lac du Bonnet granite. The strength of intact rock is divided into two components: the intrinsic strength, or cohesion; and the evolution of cohesion and friction strength are modelled using the Griffith locus based on a sliding-crack model. The parameters c_0, a_1,α_f^p,α_0^p, a_2 and H_1 can be determined by the aforementioned methods. However, for the sake of simplicity, the method based on a best fitting algorithm is used by a series of conventional triaxial compression tests performed under different confining pressures. The parameters in plastic potential function η_f^p, η_0^p and a_3 could be determined from the curves of volume strain versus stress.

The parameter κ_1 and κ_2 can also be obtained with the help of micromechanical analysis. For example, the dilute homogenization scheme, used for an elastic solid weakened by an isotropic distribution of non-interacting closed microcracks, yields the following theoretical values of degradation rate (Budiansky and O'Connell, 1976):

$$\kappa = \frac{32}{15}\frac{1-\nu^0}{2-\nu^0} \tag{3.50}$$

where ν^0 is the initial Poisson's ratio of undamaged material. The value given by (3.50) can be used as a first estimation before further experimental determination. However, in the present work, the parameters a_4, κ_1 and κ_2 is fitted by comparing the effective module in unloading path with its initial one. Typical values of model parameters are summarized in Table 3.1. With these parameters' values, the validation of the developed model is conducted for triaxial compression tests with different confining pressures, lateral extension and proportional compression tests.

Table 3.1 Typical values of model parameters for Vosges sandstone

yield function						potential function			damage function		
c_0 (MPa)	H_1 (MPa)	a_1	α_0^p	α_f^p	a_2	η_0^p	η_f^p	a_3	a_4	κ_1	κ_2
4.0	804	30	0.1	0.67	1000	-0.1	0.3	600	200	0.5	1.0

3.2.2 Triaxial compression tests

In Fig. 3.2(a)-(d), comparisons between numerical values and test data for four triaxial compression tests under confining pressures of 5MPa, 10MPa, 20MPa and 40Mpa are presented. A good agreement is observed and the mains features of typical mechanical behaviours common to most brittle geomaterials are correctly predicted, for instance, nonlinear stress-strain relations after linear phase, dependence of material strength on confining pressure, volumetric dilatancy, strain softening, and induced anisotropy of material.

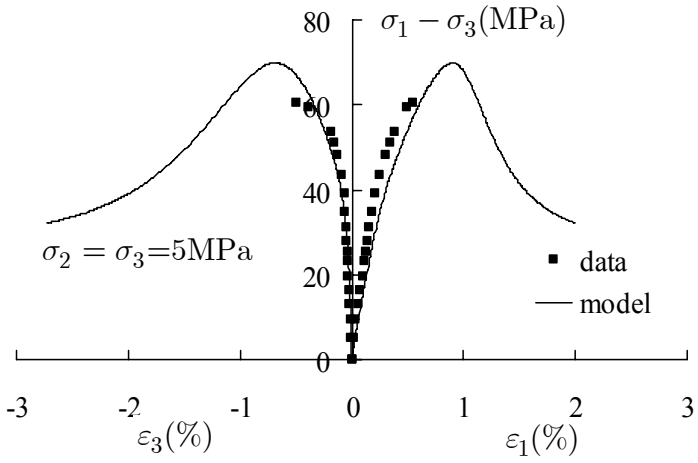

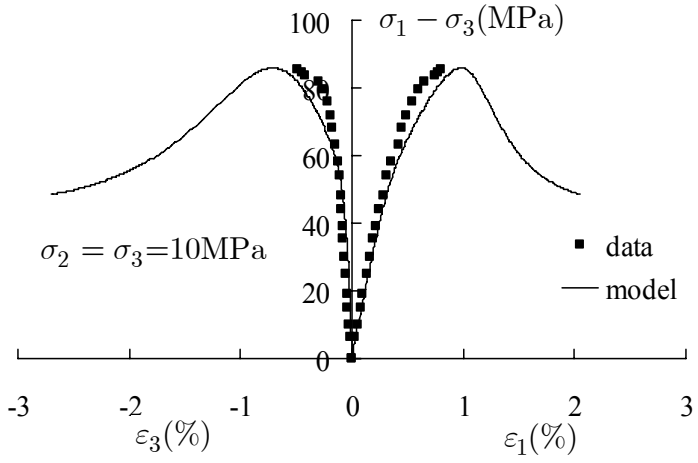

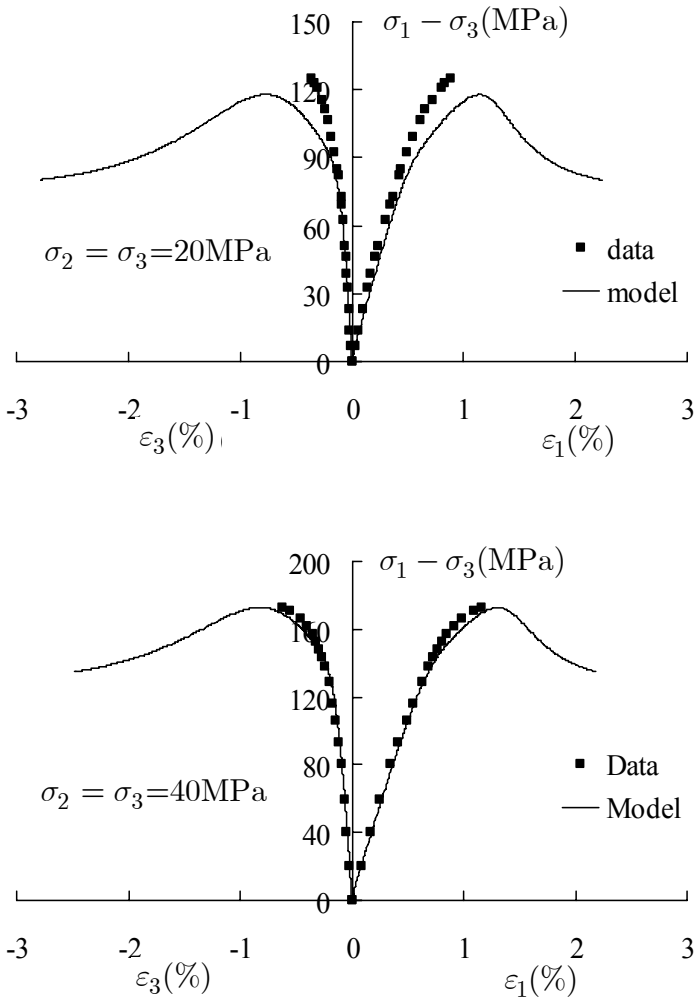

Fig. 3.2 *Comparisons between simulation results and test data for compression tests with different confining pressures*

The spatial evolution of damage and plastic hardening variables at various axial strains under confining pressures of 10MPa, 20MPa and 30MPa are illustrated in the figures 3.3, 3.4 and 3.5, respectively. Three groups of distribution rosette are very similar. Moreover, both the damage and plastic hardening variables are obviously anisotropic, orientation-dependent, and mainly locate in the weakness planes inclined at the angles between 20° and 40° with respect to the axial direction. This simulation result coincides well with experimental observation for most geomaterials. Further studies show that the biggest values of plastic strains and damage variables locate steadily at the plane inclined at about 30° with respect to the axial direction for all considered confining pressures, which can be interpreted by the fact that for each WSP

family, the plastic yield function (3.22) is defined in its own planes and that no interactions between different WSP families have been accounted for.

On the other hand, the difference between the evolution of damage variable and that of plastic hardening variable are obvious. As aforementioned, at post-peak stage, microcracks begin to be localized into a narrow shear band on macroscopic scale, leading to significant plastic deformation in few planes.

- As the axial strain increases from 0.006 for Fig.3.3(a) to 0.011 for Fig.3.4(a), the damage in the planes inclined at angles ranging from 20° and 40° with respect to the axial direction are increased significantly while the values in the other zones are increased only in a small amount.
- As the axial strain varies from 0.011 to 0.014, the damage variables in entire zone are increased in small quantities. It is noted that the axial strain values 0.006, 0.011 and 0.014 for confining pressure 20MPa corresponded to 70% peak deviatoric stress, peak deviatoric stress and residual strength, respectively. Therefore, we can find that as axial stress increases, the damage as well as plastic deformation evolve in some preferential orientation; at peak stress, the damage has fully developed; at post-peak stage, the damage in entire zone increases slowly and approaches to its asymptotic value 1. Unlike damage, the plastic strains continue to develop in some preferential orientation during failure process.
- In Fig.3.4, as the axial strain increases from 0.006 to 0.011, the damage and plastic hardening variables show similar propagation pattern; as the axial strain increased from 0.011 to 0.014, the plastic hardening variables continue to increase in a considerable amount in the weakness planes inclined at 20°-40° with respect to the axial direction, but in a very limited amount in the other zones. As a consequence, the material anisotropy becomes more pronounced, which is consistent with laboratory observation on formation of shear band.

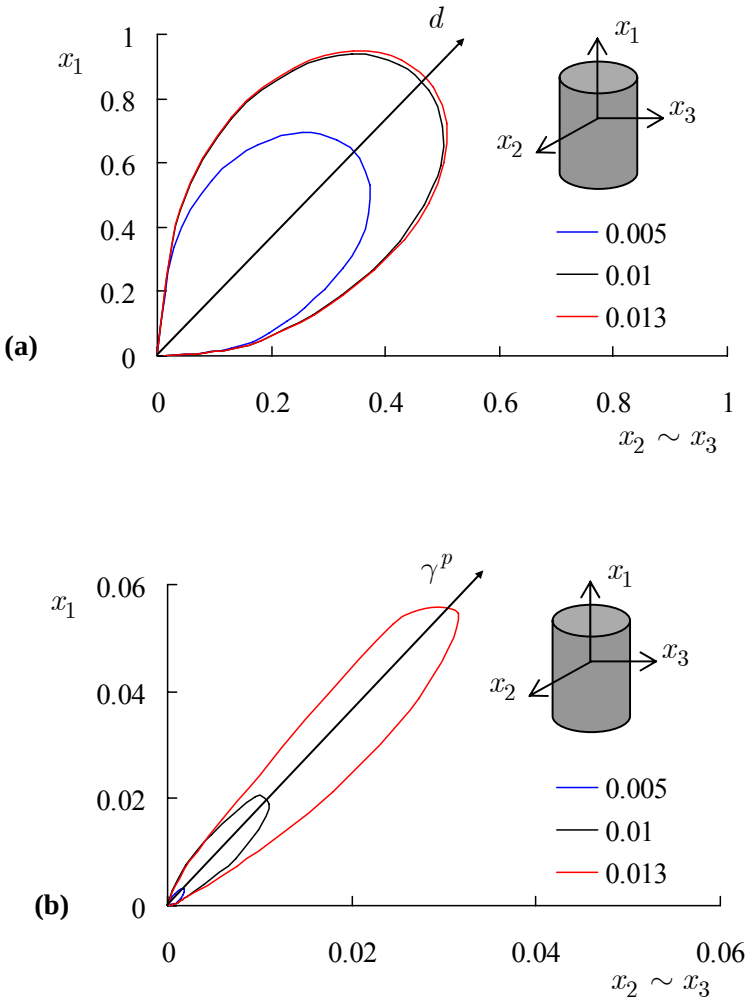

Fig. 3.3 *Spatial distribution of damage and plastic hardening variables at axial strains of 0.005, 0.01 and 0.013 under confining pressure 10MPa: (a) damage variable, (b) plastic hardening variable*

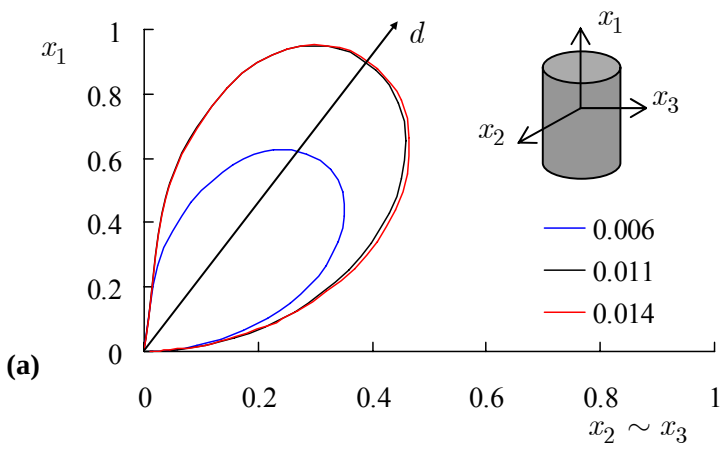

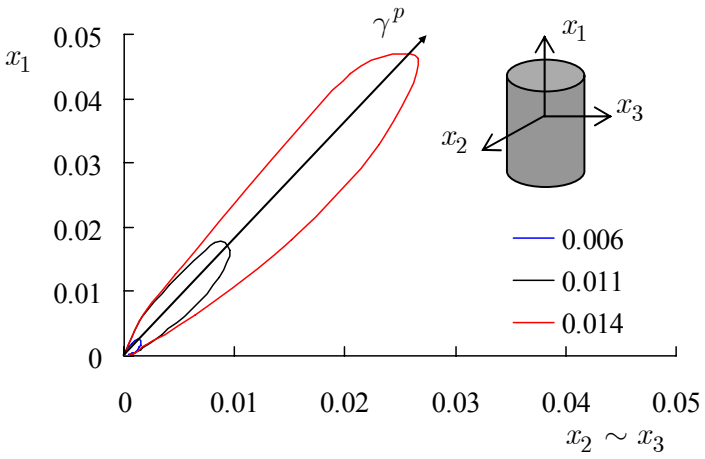

Fig. 3.4 *Spatial distribution of damage and plastic hardening variables at axial strains of 0.006, 0.011 and 0.014 with confining pressure 20MPa: (a) damage variable, (b) plastic hardening variable*

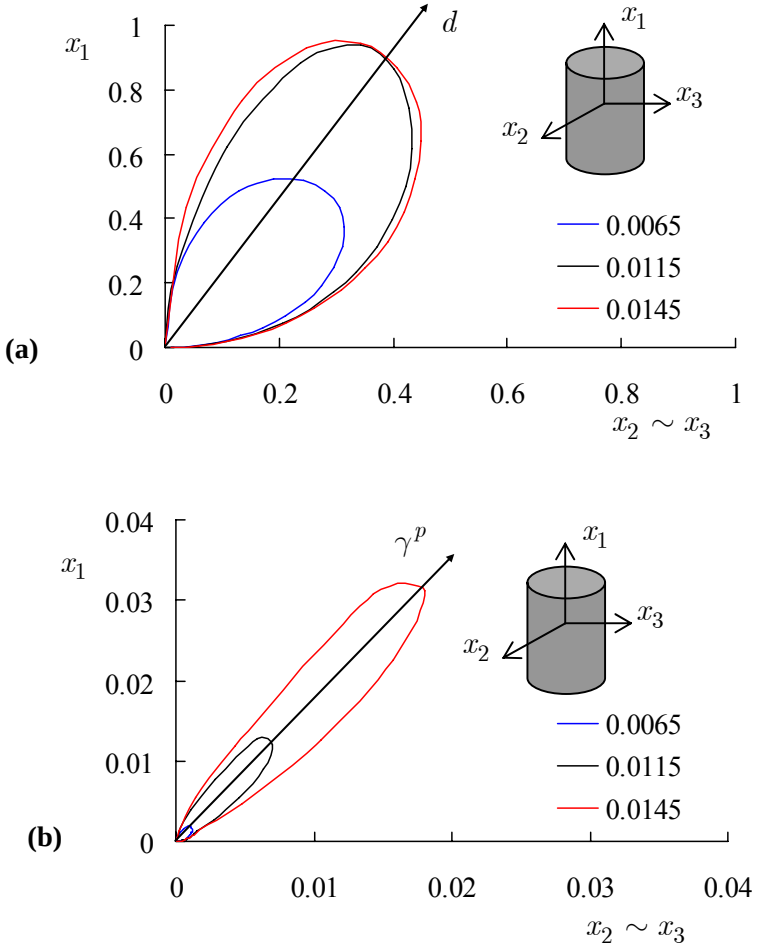

Fig. 3.5 *Spatial distribution of damage and plastic hardening variables at axial strains of 0.0065, 0.0115 and 0.0145 with confining pressure 30MPa: (a) damage variable, (b) plastic hardening variable*

It is shown on Fig. 3.6(a) that at peak stresses for all the three confining pressures, the damage values in the planes inclined at angles of 20°-40° with respect to the axial direction are almost identical and closed to the asymptotic value 1, while the damage state in the other zone are dependent on the level of confining pressures with the clear tendency that the damage zone decreases as confining pressures increase, However, we note on Fig. 3.6 (b) that the plastic hardening variables in all orientations decrease as confining pressures increase. In summary, a higher confining pressure leads to lower level of both damage and plastic hardening variables. Such observations are consistent with the usually recorded effects of confining pressures in cohesive frictional geomaterials.

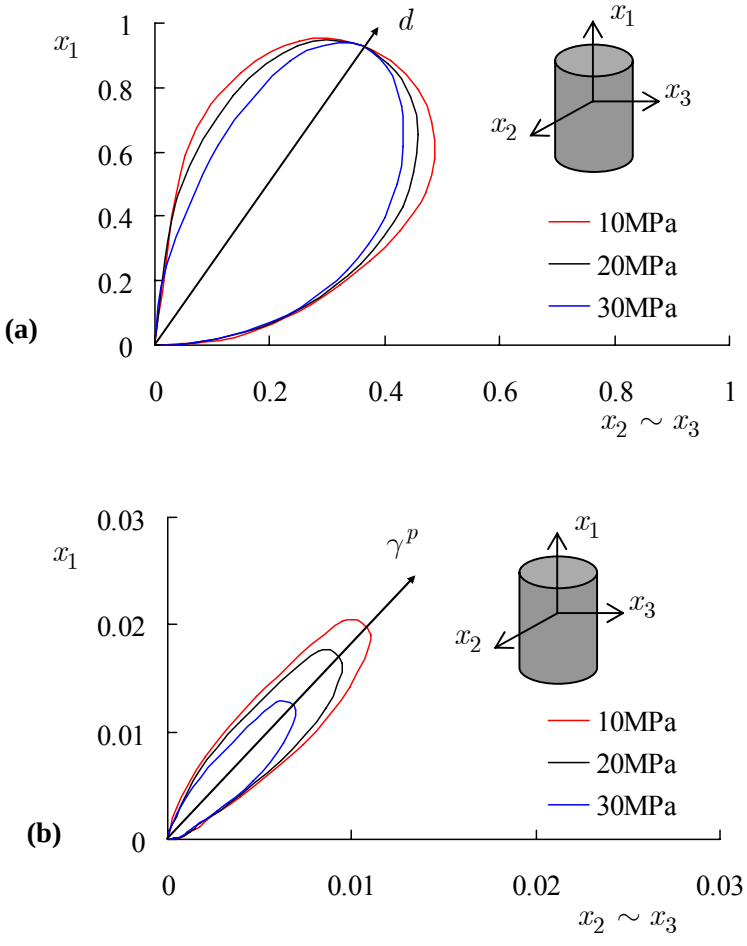

Fig.3.6 *Damage and plastic hardening variables in different orientations at peak stress under different confining pressures: (a) damage variable, (b) plastic hardening variable*

3.2.3 Lateral extension and proportional compression tests

We are now interested in checking the validity of the proposed model for lateral extension and proportional triaxial compression tests. These loading paths are different from those conventional triaxial ones, which have also been applied to identify the model parameters.

In Fig. 3.7(a) and (b), after the stage of hydrostatic stresses respectively at 40MPa and 60MPa, the lateral confining stresses suffer gradually a decrease (lateral extension by unloading) with the axial stresses remained constant. Such loading paths frequently arise in underground excavations in rock formation. Therefore, comparing with the conventional triaxial compression tests, the lateral extension tests are of more interests to practical applications. We notice that there are satisfactory agreements between the numerical simulation and experimental data.

In proportional compression tests, the axial and confining stresses are simultaneously increased with a constant proportion $k = \sigma_{11} / \sigma_{33}$. In the tests shown in Figs. 3.8(a) and (b), the proportions are fixed at $k = 7$ and $k = 12$, respectively. Again, the numerical prediction of strength, axial and lateral strain is satisfactory.

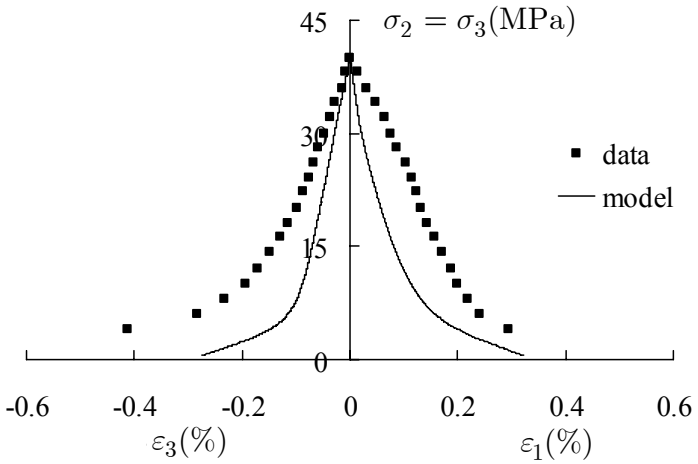

(a) Initial hydrostatic pressure is 40MPa

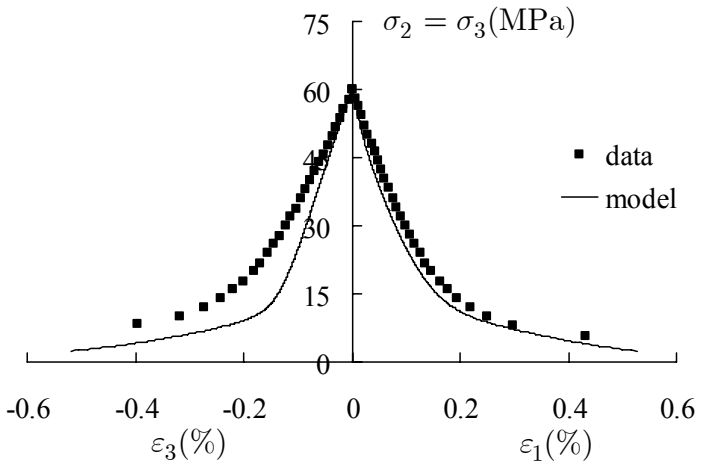

(b) Initial hydrostatic pressure is 60MPa

Fig. 3.7 *Comparisons between simulation and experimental data in lateral extension tests*

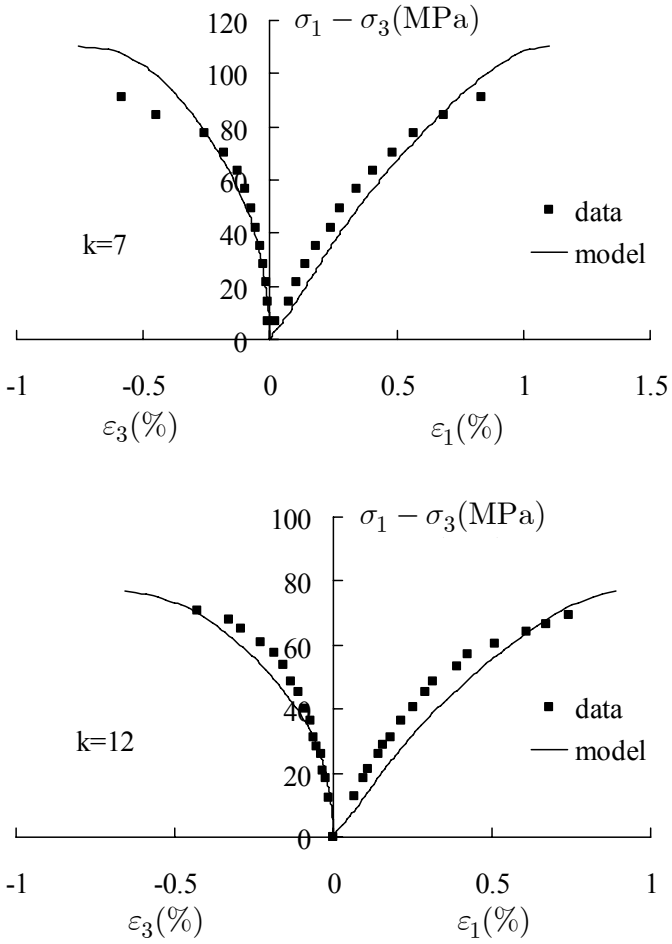

Fig. 3.8 *Comparisons between simulation and experimental data in proportional compression tests*

3.3 Conclusions

An anisotropic plastic damage model has been developed within the discrete thermodynamic framework for modelling stress-induced anisotropic mechanical behaviors in cohesive-frictional geomaterials. Compared with classic isotropic plasticity damage models, the discrete model formulation allows taking into account physical mechanisms involved in geomaterials.

The proposed model was used to simulate the mechanical tests including triaxial compression tests, lateral extension tests and proportional loading tests. A good agreement between numerical predictions and experimental data is obtained. The proposed model is proved capable of describing the main features observed in most brittle geomaterials under mechanical loading. It is more important to note that induced anisotropy both in plastic flow and damage evolution can be easily described.

This basic mechanical model will be extended within the discrete thermodynamic framework in the following chapters to account for poromechanical behaviors in geomaterials. The evolution of permeability and that of Biot's coefficients during stress loading will be modelled.

Chapter 4 Modelling of poromechanical behaviours of saturated sandstone

In the previous chapter, the basic coupled anisotropic plastic damage model has been developed in the discrete thermodynamic framework and applied to modelling mechanical behaviours of dry sandstone under various loading paths. This basic model is here extended to model poromechanical behaviours of sandstone, such as basic triaxial mechanical behaviours, evolution of Biot's coefficients and permeability in saturated sandstones. Detailed experimental data used for numerical simulations have been reported in Chapter 2. The formulation of Boit's coefficients is derived from micromechanical analysis and that of the axial permeability is divided into two parts, i.e., permeability in solid matrix and permeability induced by cracks. Some comparisons between numerical results and test data are presented.

4.1 Modelling of mechanical behaviour

The mechanical parameters for saturated sandstone can be determined by following the same procedure as that for dry samples studied in the previous chapter. The initial (undamaged) elastic constants are derived from cyclic loading at elastic stage: $E^0 = 10000\text{MPa}$ and $\nu^0 = 0.16$. Typical values of other mechanical model parameters are provided in Table 4.1.

Table 4.1 Typical values of parameters of discrete plastic damage model

yield function						potential function			damage function		
c_0(MPa)	H_1(MPa)	a_1	α_0^p	α_f^p	a_2	η_o^p	η_f^p	a_3	a_4	κ_1	κ_2
6.0	354	35	0.1	0.67	1000	-0.1	0.3	300	70	0.5	1.0

Comparisons between numerical simulations and experimental data obtained from triaxial

compression tests on sandstone are presented in Fig.4.1. It is observed that the basic mechanical model is able to describe the main mechanical behaviors of geomaterials, including nonlinear stress-strain relations, dependence of material strength on confining pressure, brittle-ductile transition with the increase of confining pressure, volumetric dilatancy during shear sliding, degradation of elastic modulus, and induced anisotropy of material.

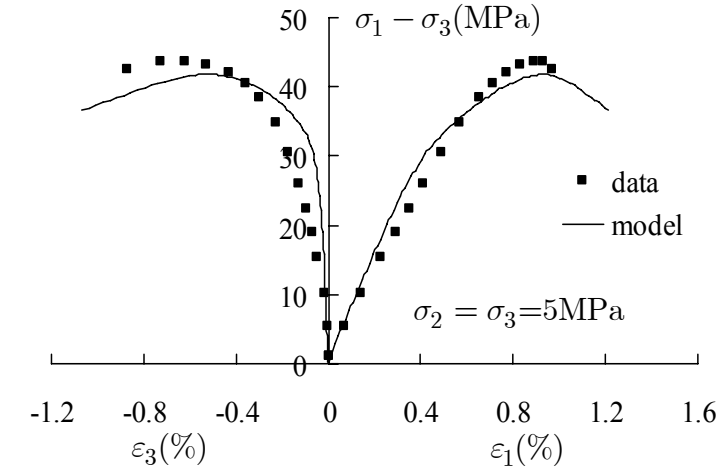

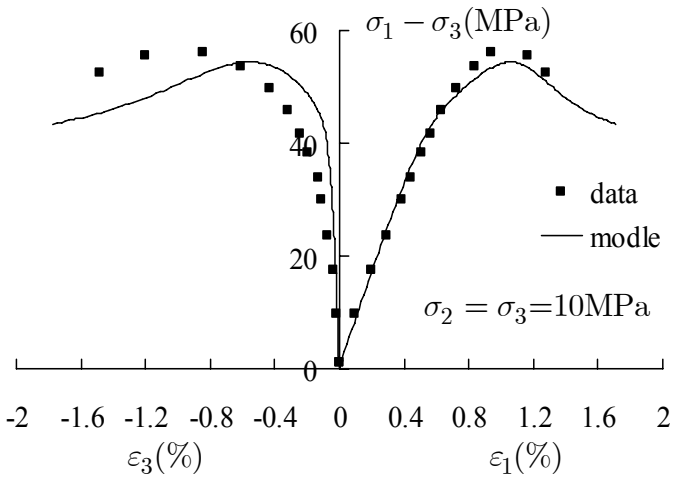

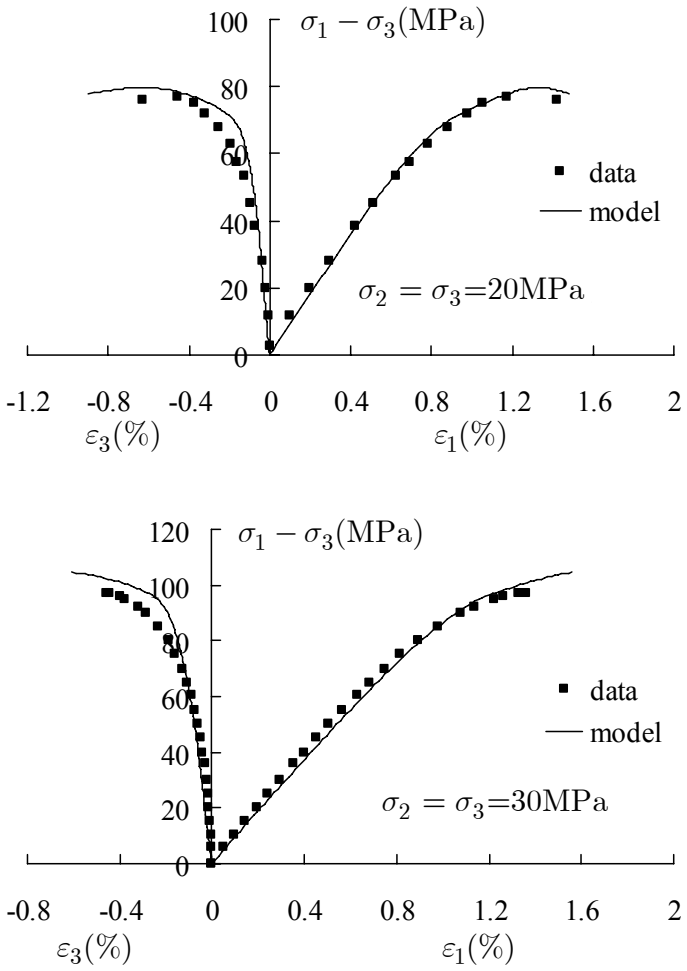

Fig. 4.1 *Numerical results of triaxial compression tests with confining pressures of 5, 10, 20 and 30MPa*

The predicted variation of the axial and radial elastic modulus (E_1 and $E_r = E_1 / \nu_{31}$, respectively) is compared with test data in Fig.2. Globally satisfactory agreements have been observed. It is clearly shown that for all levels of confining pressures (5MPa, 10MPa, 20MPa and 30MPa), the degradation of elastic stiffness in radial directions is much greater than that in the axial direction, which can be interpreted by the facts that microcracks with their shearing planes nearly parallel to the axis x_1 gain more growth than others. Consequently, final fracture zone(s) induced by strain localization is generally inclined at less than 45° with respect to the symmetry axis x_1.

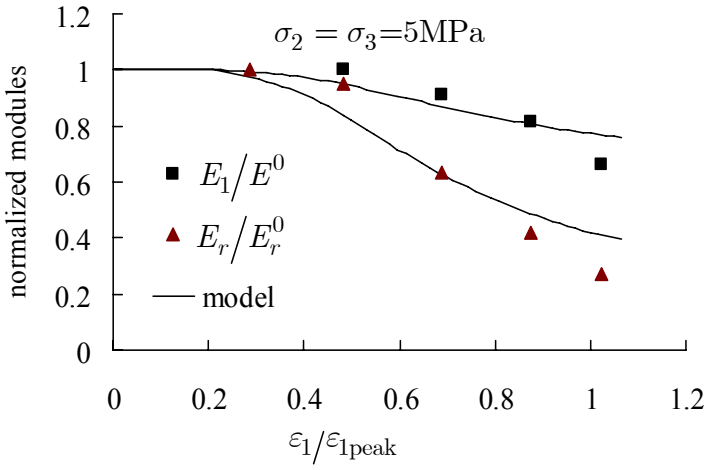

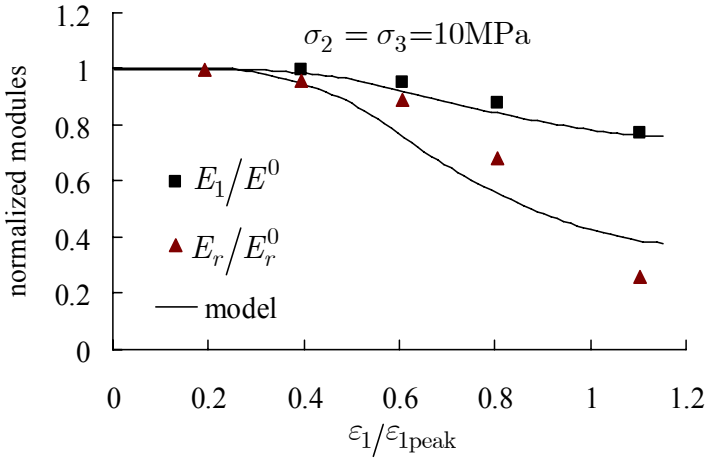

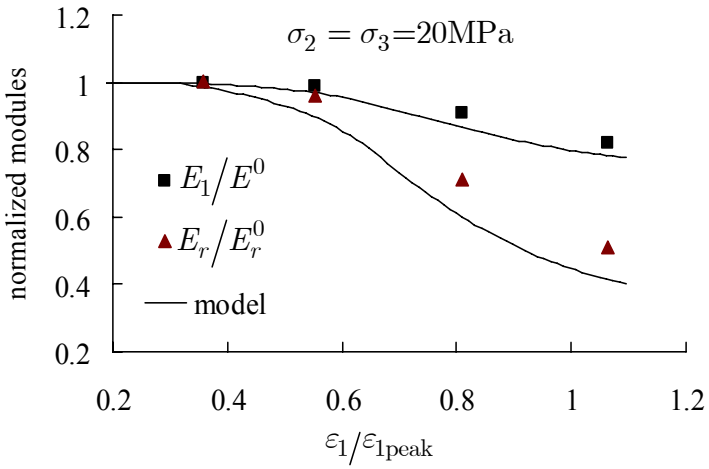

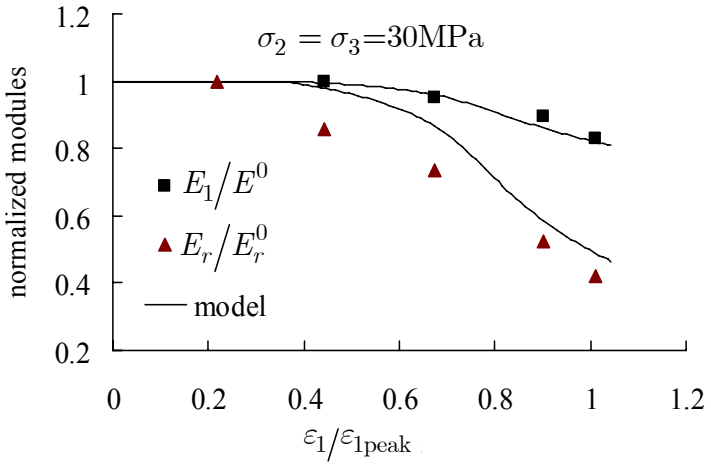

Fig. 4.2 *Variations of the normalized effective elastic constants as function of the normalized axial strain for four triaxial compression tests with confining pressures of 5, 10, 20 and 30MPa*

4.2 Modelling of Biot's coefficients

Laboratory investigations on Biot's coefficients (see Fig.2.14) show that: (a) Biot's coefficients in axial and radial directions exhibit abvious anisotropy, more precisely, the value in axial direction is generally smaller than that in radial one, which is mainly due to the preferential propagation of microcracks; (b) Biot's coefficients are affected significantly by stress-induced damage during deformation process. Damage propagation leads to the increase in Biot's coefficients; (c) Biot's coefficients are dependent on confining pressures, that is, the value of Biot's coefficients decrease with increase of confining pressures. Based on physical interpretation of Biot's coefficients, a micromechanics-based model will be proposed to describe such anisotropic characteristics of Biot's coefficients. We first introduce the method proposed by Cheng (1997) for description of anisotropic Biot's coefficients from micromechanical viewpoints. This method is then incorporated into the previously-established discrete plastic damage model. Finally, the numerical prediction of Biot's coefficients is compared with experiment data in both axial and radial directions.

4.2.1 Determination of Biot's coefficients

According to the micromechanical analyses conducted by Thompson and Willis (1991)

and Cheng (1997) on initially anisotropic porous media, the macroscopic poroelastic constants can be deduced from the microscopic properties of the constituents of porous medium. From the viewpoint of material microstructure, such micro-macro analysis is also applicable for damage-induced anisotropic porous materials in given damage state. By considering the deformation of saturated porous medium on microscopic scale, the following relationship has been established (for more details, see Thompson and Willis, 1991; Cheng , 1997):

$$\boldsymbol{b}(\mathbf{d}) = \boldsymbol{\delta} - \mathbb{C}(\mathbf{d}) : \mathbb{S}^s : \boldsymbol{\delta} \tag{4.1}$$

where we recall $\boldsymbol{b}$ denotes the second rank anisotropic tensor of Biot's coefficients; $\mathbb{C}(\mathbf{d})$ represents the fourth rank elastic stiffness tensor of material in its damaged state and under drained condition; $\mathbb{S}^s = (\mathbb{C}^s)^{-1}$ is the fourth rank elastic compliance tensor of solid grains, which is assumed to be constant. For the sake of simplification, two fundamental assumptions are commonly adopted: the first one, called *micro-homogeneity*, states that the skeleton of porous material is homogeneous on the pore (microscopic) scale, although the material is most often heterogeneous on the macroscopic scale due to non uniform spatial distribution of these micro-homogeneous materials (Nur and Byerlee, 1971); the second one, named *micro-isotropy*, assumes that the solid constituent in the porous medium is isotropic at the microscopic (pore and grain) level, and the macroscopic material anisotropy is of structural origin, mainly resulting from oriented pore and fissure arrangement. These assumptions allow us to simplify the above equation into the form (Cheng, 1997):

$$\boldsymbol{b}(\mathbf{d}) = \boldsymbol{\delta} - \frac{1}{3k^s}\mathbb{C}(\mathbf{d}) : \boldsymbol{\delta} \tag{4.2}$$

where k_s is the bulk modulus of the solid matrix.

When damaged porous material exhibits orthotropic behaviour and all the three material symmetry planes are parallel to the principal directions of the second order damage tensor defined by discrete damage variables

$$d_{ij} = \sum_{r=1}^{15} \varpi^r d^r n_i^r n_j^r , \tag{4.3}$$

the matrix form of Biot's coefficients is then given by

$$b_{ij} = \begin{bmatrix} b_{11} & 0 & 0 \\ 0 & b_{22} & 0 \\ 0 & 0 & b_{33} \end{bmatrix} \tag{4.4}$$

The three principal components of the above tensor are determined from (4.2):

$$\begin{cases} b_{11} = 1 - \dfrac{C_{1111} + C_{1122} + C_{1133}}{3k_s} \\ b_{22} = 1 - \dfrac{C_{2211} + C_{2222} + C_{2233}}{3k_s} \\ b_{33} = 1 - \dfrac{C_{3311} + C_{3322} + C_{3333}}{3k_s} \end{cases} \tag{4.5}$$

In the case of cylindrical triaxial loading where samples are subjected to axisymmetric stresses with $\sigma_{22} = \sigma_{33}$, we have accordingly $\varepsilon_{22} = \varepsilon_{33}$ and $d_{22} = d_{33}$. By setting $C_{2222} = C_{3333}$ and $C_{1122} = C_{1133}$ in (4.5), the Biot's coefficients in axial and lateral directions can then be written as follows:

$$\begin{cases} b_{11} = 1 - \dfrac{C_{1111} + 2C_{1133}}{3k_s} \\ b_{22} = b_{33} = 1 - \dfrac{C_{3311} + C_{3322} + C_{3333}}{3k_s} \end{cases} \tag{4.6}$$

Recall that the bulk modulus k_s of the solid grains is measured by hydrostatic compression test under partially drained condition, and the value $k_s = 50548\mathrm{MPa}$ has been determined from laboratory investigations in Section 2.5 of Chapter 2. The components of the elastic stiffness tensor for any damage state can easily be derived from the discrete plastic damage model. Therefore, with the help of (4.6), it is then possible to predict the evolution of Biot's coefficients with damage in both the axial and radial directions in drained conventional triaxial compression tests.

4.2.2 Simulation results

Fig.4.3 shows the comparison of Biot's coefficients between numerical simulation and test data under different confining pressures. It is noted that the change of the Biot's coefficient in the radial directions is much more significant than that in the axial one. However, the

numerical values of Biot's coefficients in axial direction are smaller than the experimental one near the peak stresses. Microcracks gradually propagate under deviatoric compressive stress and suffer a phase of coalescence as plastic flow, leading to some macroscopic cracks at final stage. Therefore, the above *micro-homogeneity* and *micro-isotropy* assumptions are not reliable any more near peak stresses, which causes the difference of Biot's coefficients between numerical prediction and test data.

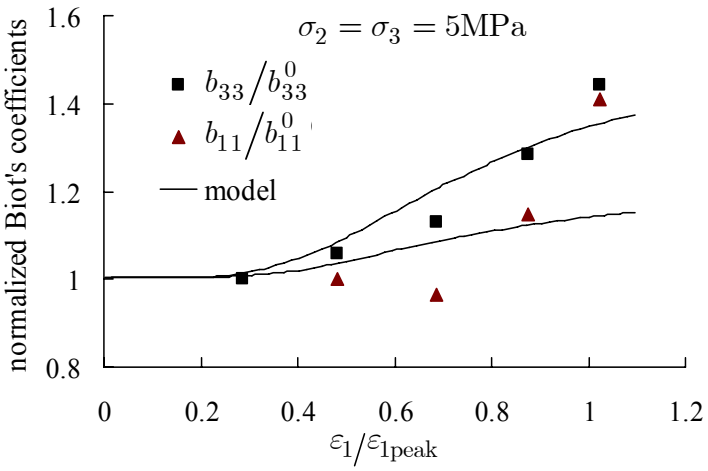

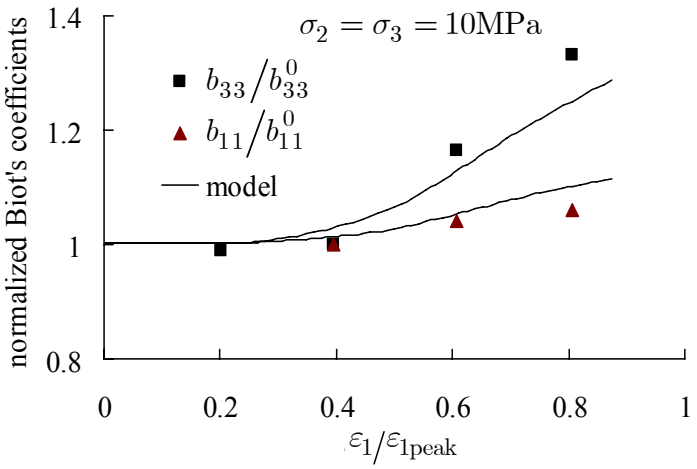

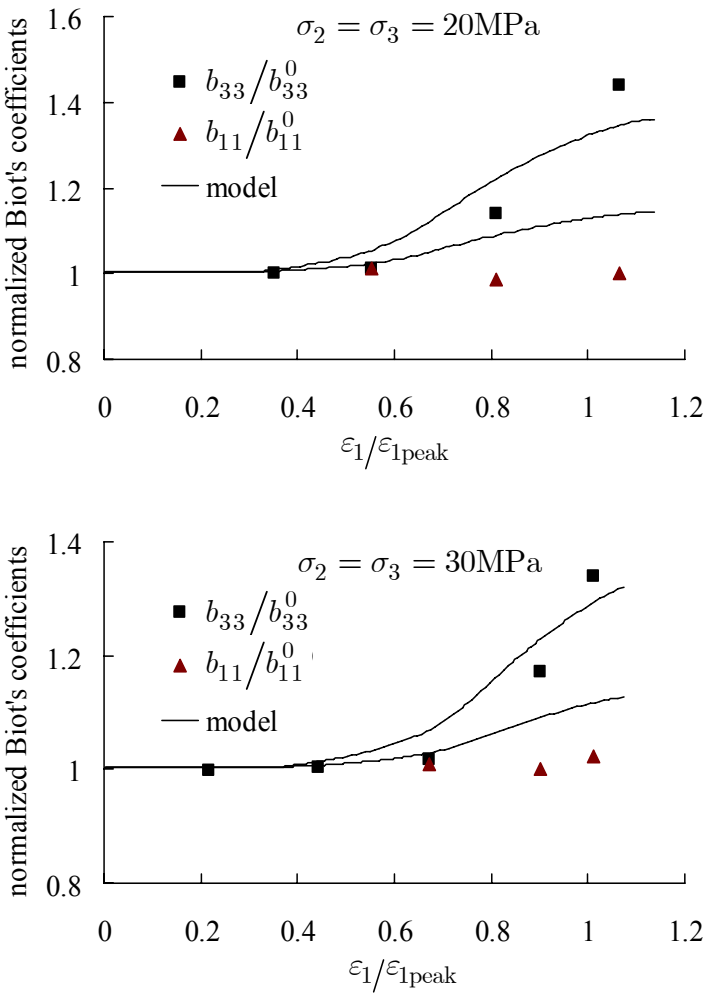

Fig. 4.3 *Evolution of normalized Biot's coefficients in axial (b_{11}) and radial (b_{33}) directions versus the normalized axial strain from triaxial tests with different confining pressures (5, 10, 20 and 30MPa)*

4.2.3 Modelling of evolution in permeability

Laboratory investigations show that permeability in sandstone decreases quite quickly during the first two stages of rock deformation, that is, the closure phase of initial bedding planes and microcracks and the elastic linear phase of stress-strain curves. Then, after the onset of microcracks propagation, the decrease in permeability is attenuated and even an increase phase is often captured at low confinements. When the effects of volume compaction in porous matrix (induced by mean stress) and of volumetric dilatancy induced by microcrack growth are taken into account, it is convenient to divide the permeability variable into two parts, respectively associated with the porous matrix phase and microcracks, i.e.

$$\boldsymbol{K} = \boldsymbol{K}^m + \boldsymbol{K}^c \tag{4.7}$$

where $\boldsymbol{K}^m$ denotes the permeability of porous matrix and $\boldsymbol{K}^c$ the permeability induced by microcracks growth. Correspondingly, the Darcy law already defined in (4.8) also adopts the following two-part decomposition

$$\underline{v} = -\frac{\boldsymbol{K}}{\mu}\cdot\nabla p = -\frac{\boldsymbol{K}^m}{\mu}\cdot\nabla p - \frac{\boldsymbol{K}^c}{\mu}\cdot\nabla p \tag{4.9}$$

An empirical relationship between $\boldsymbol{K}^m$ and mean stress σ_m is used to describe the influence of the mean stress on permeability.

$$\boldsymbol{K}^m = e^{-a_5\sigma_m}\boldsymbol{K}^0 \tag{4.10}$$

where $\boldsymbol{K}^0$ is the permeability of sandstone in its initial state and a_5 is a model parameter controlling the evolution rate. Under isotropic assumption of the initial state of sandstone, $\boldsymbol{K}^0$ is written in the form:

$$\boldsymbol{K}^0 = K^0\boldsymbol{\delta} \tag{4.11}$$

where K^0 is a scalar-valued parameter representing the initial isotropic permeability of material. The values of K^0 and a_5 can be determined by fitting the permeability evolution under hydrostatic loading. A typical evolution of the permeability under hydrostatic pressures is plotted in Fig.4.4 and the values of the above two parameters are determined as $K^0 = 3.6\times10^{-16}m^2$ and $a_5 = 0.024$.

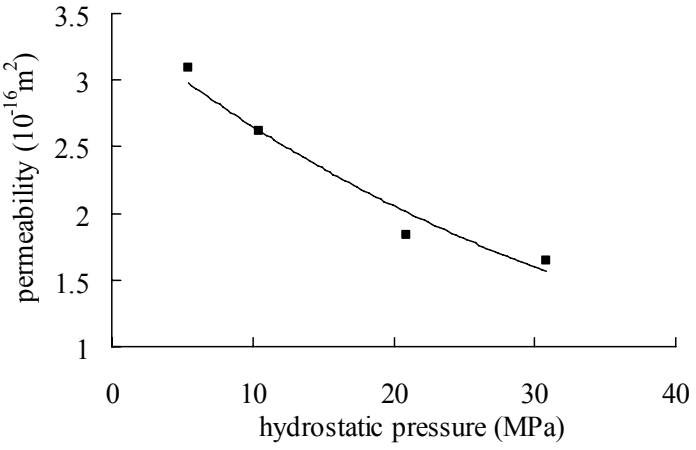

Fig. 4.4 *Experiments (points) and fitting curve (solid line) of permeability with hydrostatic pressures*

Since the term $\boldsymbol{K}^c$ is induced by crack nucleation and growth, it should be described by basic variables of microcracks, such as the normal vector $\underline{n}$, the radius $r(\underline{n})$ and aperture $e(\underline{n})$ of crack surface. For the sake of simplicity, microcracks are here assumed to be penny-shaped and propagate in a self-similar way. Under the initially isotropic assumption, the number of weakness sliding planes in all WSP families is assumed to be identical and denoted by N. From the usual definition of the damage variable $d(\underline{n})$ (Budiansky and O'Connell, 1976)

$$d(\underline{n}) = \frac{Nr^3(\underline{n})}{\Omega}, \tag{4.12}$$

one derives the radius $r(\underline{n})$

$$r(\underline{n}) = \left[\frac{\Omega d(\underline{n})}{N(\underline{n})}\right]^{1/3} \tag{4.13}$$

where N/Ω is the WSP density per family per unit volume. In addition, we note the averaging aperture $e(\underline{n})$ can be linked to the normal component of the displacement jump $[u_n]$:

$$e(\underline{n}) = \frac{1}{\pi[r(\underline{n})]^2}\int_{\omega^+}[u_n]\mathrm{d}S \tag{4.14}$$

where ω^+ and $\mathrm{d}S$ denote the crack surface and a small integration area on crack surface, respectively. On the other hand, the definition of the variable $\beta(\underline{n})$ (Pensee et al., 2002; Zhu et al, 2008a) allows to set up the following relation tween the aperture $e(\underline{n})$ and normal strain $\beta(\underline{n})$, i.e.:

$$e(\underline{n}) = \frac{1}{\pi[r(\underline{n})]^2}\frac{\beta(\underline{n})\Omega}{N} \tag{4.15}$$

Furthermore, it is also assumed that fluid flow takes place only in the direction parallel to the crack plane and can be described by the Navier–Stokes equation for laminar flow between two parallel plates (Shao et al, 2005). The local flow velocity, denoted by $\underline{v}^c(\underline{n})$, is thus expressed as follows:

$$\underline{v}^c(\underline{n}) = -\frac{\lambda}{12}\frac{1}{\mu}[e(\underline{n})]^2\left(\boldsymbol{\delta} - \underline{n}\otimes\underline{n}\right)\cdot\left(\nabla p\right)^c \tag{4.16}$$

where $(\nabla p)^c$ denotes the local pressure gradient vector applied to the crack. The positive scalar λ, less than the unity, is introduced to take into account the fact that every part of a crack does not work as a conduit but some parts may be left as dead end. When $\lambda = 1$, the classic cubic law is recovered. The local pressure gradient may be related to the macroscopic gradient by an appropriate localization law (Dormieux and Kondo, 2004). In this model, we have used a simplified law by assuming that $(\nabla p)^c = \nabla p$, implying that the local pressure gradient is equal to the macroscopic one. The macroscopic fluid flow velocity $\underline{v}$ is obtained from the averaging of local velocity field $\underline{v}^c(\underline{n})$ over the crack volume:

$$\underline{v} = -\frac{\boldsymbol{K}^m}{\mu}\cdot\nabla p + \frac{1}{\Omega}\int_{\Omega}\underline{v}^c(\underline{x})\mathrm{d}\Omega = -\frac{\boldsymbol{K}^m}{\mu}\cdot\nabla p + \frac{1}{\Omega}\int_{\Omega^c}\underline{v}^c(\underline{x})\mathrm{d}\Omega^c \tag{4.17}$$

where Ω^c denotes the volume occupied by microcracks. After determination of the crack space distribution at a given loading step, it is easy to calculate the volume occupied by microcracks. The crack volume occupied by a set of cracks with the unit vector $\underline{n}$ normal to their surface may be calculated by:

$$\mathrm{d}\Omega^c = N\pi[r(\underline{n})]^2 e(\underline{n}) \tag{4.18}$$

By integration over all the space orientations, the macroscopic flow velocity can be rewritten as:

$$\underline{v} = -\frac{\boldsymbol{K}^m}{\mu}\cdot\nabla p + \frac{N}{\Omega}\frac{1}{4\pi}\int_{S^2}\underline{v}^c(\underline{n})e(\underline{n})\pi[r(\underline{n})]^2\mathrm{d}S \tag{4.19}$$

Substituting the local flow velocity $\underline{v}^c(\underline{n})$ given in (4.16), the macroscopic velocity of fluid is finally determined by:

$$\underline{v} = -\frac{\boldsymbol{K}^m}{\mu}\cdot\nabla p - \frac{1}{\mu}\frac{\lambda}{12}\frac{N}{\Omega}\frac{1}{4\pi}\int_{S^2}e(\underline{n})[e(\underline{n})]^3\pi[r(\underline{n})]^2(\boldsymbol{\delta}-\underline{n}\otimes\underline{n})\mathrm{d}S\cdot\nabla p \tag{4.20}$$

Comparison of (4.20) with the macroscopic Darcy law (4.9) allows to derive the overall crack permeability tensor as follows

$$\boldsymbol{K}^c = \frac{\lambda\pi}{12}\frac{N}{\Omega}\frac{1}{4\pi}\int_{S^2}[e(\underline{n})]^3[r(\underline{n})]^2(\boldsymbol{\delta}-\underline{n}\otimes\underline{n})\mathrm{d}S \tag{4.21}$$

Next, inserting (4.12) and (4.15) into (4.21) leads to the formulation of $\boldsymbol{K}^c$ in integration

form

$$\boldsymbol{K}^c = \left(\frac{\lambda\pi}{12}\right)\left(\frac{N}{\Omega}\right)^{-2/3} \frac{1}{4\pi}\int_{S^2} \pi^{-3}[\beta(\underline{n})]^3[d(\underline{n})]^{-4/3}(\boldsymbol{\delta} - \underline{n}\otimes\underline{n})\mathrm{d}S \tag{4.22}$$

and in discrete form

$$\boldsymbol{K}^c = \pi^{-2}\frac{\lambda}{12}\left(\frac{N}{\Omega}\right)^{-2/3} \sum_{r=1}^{15} \varpi^r(\beta^r)^3(d^r)^{-4/3}(\boldsymbol{\delta} - \underline{n}\otimes\underline{n}) \tag{4.23}$$

The total permeability finally reads:

$$\boldsymbol{K} = e^{-a_5\sigma_m}\boldsymbol{K}^0 + \pi^{-2}\frac{\lambda}{12}\left(\frac{N}{\Omega}\right)^{-2/3} \sum_{r=1}^{15} \rho^r(\beta^r)^3(d^r)^{-4/3}(\boldsymbol{\delta} - \underline{n}^r\otimes\underline{n}^r) \tag{4.24}$$

In the above equation, the variables σ_m, β^r and d^r can be obtained from the mechanical model developed in the previous section. The density parameter N/Ω takes the value $N = 1\times10^{11}$ for all chosen families of WSPs. For the sake of simplicity, λ is fixed at $\lambda = 1$. The comparisons between the numerical result and experimental data of axial permeability evolution are shown in Fig. 4.5. It is obviously shown that the evolution of permeability during stress loading can be decomposed into two stages: at the first one, the permeability decreases with stress loading, corresponding to the pre-peak phase of the stress-strain curves. For all confining pressures, the smallest values occur at the stress-peak, beyond which the permeability augments again due to the growth and nucleation of cracks. This two-phase separation seems more obvious at low confining pressures, which can be interpreted by the face that the post-peak reduction in permeability is enhanced by the decrease of the mean stress σ_m for relatively low confining pressures.

4.3 Conclusions

In this chapter, the discrete plastic damage model has been applied to simulate the mechanical behaviour, poroelastic properties and permeability of saturated sandstones. For mechanical model, the modified Coulomb-type plastic yield and plastic potential function, damage evolution criterion of Mazars type are used for each family of weakness planes. It is observed

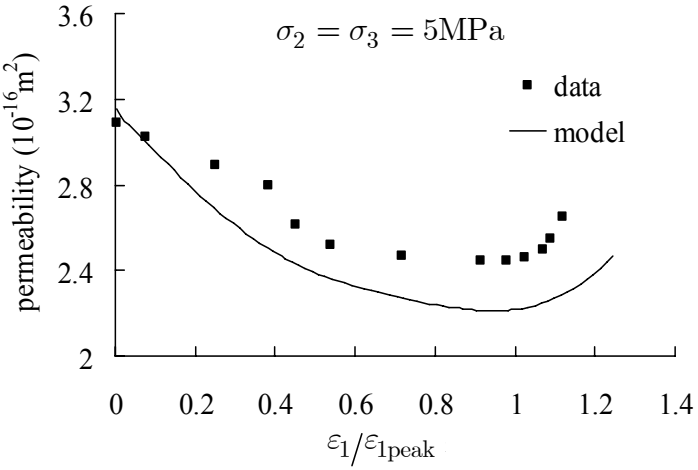

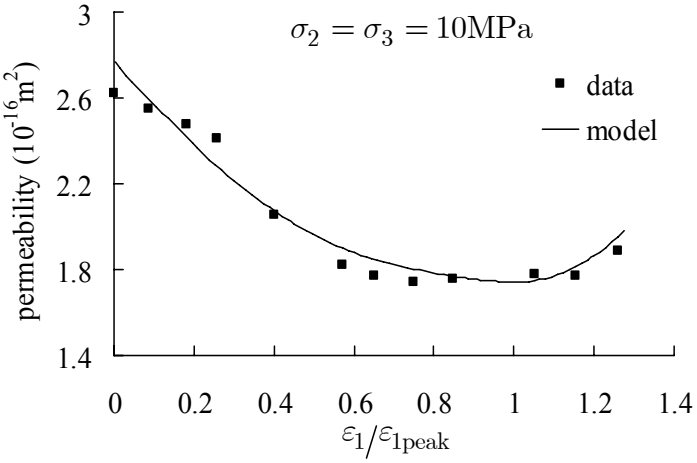

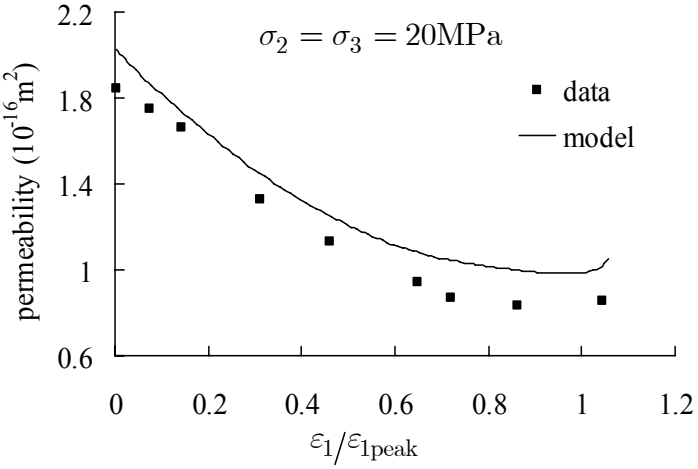

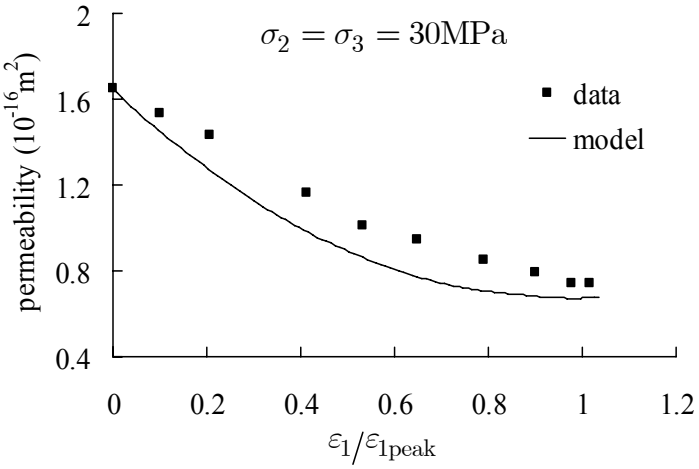

Fig. 4.5 *Evolution of axial permeability as function of the normalized axial strain in four triaxial tests with different confining pressures (5, 10, 20 and 30MPa)*

that the model is able to describe the main mechanical behaviour including nonlinear stress strain relations, brittle-ductile transition with confining pressure, volumetric dilatancy, elastic modulus degradation and induced anisotropy. Biot's coefficients is written as function of effective elastic stiffness tensor and bulk modulus of the solid matrix, the comparisons between the numerical simulation and test data shows that the proposed model is able to describe the anisotropic property of Biot's coefficients in axial and radial directions. In permeability characterization, rock permeability is divided into permeability in matrix phase and permeability induced by crack, the evolution of axial permeability is well simulated during triaxial compression tests with different confining pressures.

Chapter 5 Modelling of anisotropic poroplastic damage behaviors

In the previous chapters, some poroelastic behaviors in geomaterials have been simulated. This final chapter is devoted to formulate an anisotropic poroplastic damage model to describe poromechanical behaviour of saturated rocks. The determination of Biot's coefficients is performed in elastic regime. As for the plastic yield and potential functions of saturated porous media, the so-called *stress equivalence principle* is employed to define the effects of pore pressure on the normal component of local traction vector for each family of weakness planes. The complementary plastic porosity variable is introduced and related to the variation in volume plastic deformation. The proposed anisotropic model is applied to simulate undrained compression tests and strain response induced by increase of pore pressure.

5.1 Presentation of model

5.1.1General framework

The general framework is formulated under the assumption of small strains and isothermal condition. Considering a porous material sample subjected to current stress $\boldsymbol{\sigma}$ and current pore pressure p and from this current state, let $\mathrm{d}\boldsymbol{\sigma}$ and $\mathrm{d}p$ be the incremental loading in stress and fluid pressure, and $\mathrm{d}\boldsymbol{\varepsilon}$ and $\mathrm{d}m$ denote the incremental strain and the change of fluid mass induced by the incremental loading. The incremental strain and the change of fluid mass can be respectively decomposed into elastic increment $\mathrm{d}\boldsymbol{\varepsilon}^e$ and $\mathrm{d}m^e$ and plastic increment $\mathrm{d}\boldsymbol{\varepsilon}^p$ and $\mathrm{d}m^p$, i.e. (Coussy, 1995, 2004):

$$\mathrm{d}\boldsymbol{\varepsilon} = \mathrm{d}\boldsymbol{\varepsilon}^e + \mathrm{d}\boldsymbol{\varepsilon}^p, \quad \mathrm{d}m = \mathrm{d}m^e + \mathrm{d}m^p \tag{5.1}$$

In practice, a non-dimensional variable $\mathrm{d}\phi^p$ is usually used instead of $\mathrm{d}m^p$, denoting the incremental plastic porosity and defined as:

$$\mathrm{d}\phi^p = \frac{\mathrm{d}m^p}{\rho_f^0} \tag{5.2}$$

where ρ_f^0 is the fluid mass density. Within the elastoplastic damage framework as mentioned in Chapter 1, a thermodynamic state of porous material is characterized by the external state variables ε, ϕ and the internal state variables ε^p, ϕ^p, $\mathbf{d}$ and γ^p, among which $\mathbf{d}$ represents the set of discrete damage variables, γ^p is plastic hardening variable used to control the plastic evolution. The thermodynamic potential of elastoplastic damaged porous material takes the following general form:

$$\psi = \psi^e\left((\varepsilon - \varepsilon^p),(\phi - \phi^p),\mathbf{d}\right) + \psi^p(\mathbf{d},\gamma^p) \tag{5.3}$$

where the second term on the right side $\psi^p(\mathbf{d},\gamma^p)$ is the total locked plastic energy, assumed to be a function of internal hardening variables $\mathbf{d}$ and γ^p.

According to the physic linear assumption, only the linear and second order terms of the internal and external variables are taken into account and the following potential function ψ is then adopted:

$$\begin{aligned}\psi = &\frac{1}{2}(\varepsilon - \varepsilon^p) : \mathbb{C}^b(\mathbf{d}) : (\varepsilon - \varepsilon^p) + \psi^p(\mathbf{d},\gamma^p) \\ &- M(\mathbf{d})(\phi - \phi^p)\boldsymbol{b}(\mathbf{d}) : (\varepsilon - \varepsilon^p) + \frac{1}{2}M(\mathbf{d})(\phi - \phi^p)^2\end{aligned} \tag{5.4}$$

where $\mathbb{C}^b(\mathbf{d})$ is the fourth order elastic stiffness tensor of the damaged skeleton frame under drained conditions; $M(\mathbf{d})$ is the Biot's moduli depending on the damage variable; the symmetric second rank tensor $\boldsymbol{b}(\mathbf{d})$ defines the anisotropic Biot's coefficients of the damaged porous material. The first term on the right side of the above equation represents the elastic strain energy of the dry skeleton frame and the second one is the locked plastic energy of the dry skeleton frame. Therefore, the first two terms denote the total energy of the dry skeleton frame. The third and fourth terms represent coupling energy in the saturated damaged porous system.

The standard derivative of the thermodynamic potential leads to the constitutive laws of saturated porous medium:

$$\boldsymbol{\sigma} = \mathbb{C}^b(\mathbf{d}) : (\varepsilon - \varepsilon^p) - \boldsymbol{b}(\mathbf{d})p \tag{5.5}$$

$$p = M(\mathbf{d})[-\boldsymbol{b}(\mathbf{d}) : (\varepsilon - \varepsilon^p) + (\phi - \phi^p)] \tag{5.6}$$

5.1.2 Plastic yield, potential functions and damage criterion

It has been assumed that the material under consideration is initially linear isotropic, and that the anisotropic plastic deformation is induced by preferential slipping in some weakness orientations due to deviatoric stress. The structure (inherent) anisotropy is not considered in the present work. Therefore, a same form of plastic yield and potential function can be employed for all material orientations.

The extension of plastic yield and potential functions from dry material to saturated porous media needs to take into account the effect of pore pressure. The concept of effective stress provides a possibility to extend the plastic laws by using the strain or stress equivalence principles. Some studies have been carried out to verify the concept both in elastic and inelastic domain (Rice and Cleary, 1976; P. De Buhan et al, 1992; Lydzba and Shao, 2000).

In the present work, a mobilized coefficient b^r for the r^{th} family is introduced to define the effect of the pore pressure on the local normal stress for each family of weakness sliding planes saturated by water and written in the from:

$$b^r = 1 - (1 - b_0)e^{-a_6\gamma^{p,r}} \tag{5.7}$$

where b_0 represents the initial value of effective stress coefficient, a_6 denotes the evolution rate from b_0 to 1 with the shear deformation increasing along the weakness sliding planes.

Therefore, the local equivalent normal stress of each family of weakness sliding planes saturated by water is written in the form:

$$\tilde{\sigma}_n^r = \sigma_n^r + b^r p \tag{5.8}$$

Based on the so-called stress equivalence principle, the basic idea is to extend the plastic yield and potential functions for dry materials to saturated porous media by simply replacing the nominal local normal stress σ_n^r by the equivalent local normal stress $\tilde{\sigma}_n^r$. The Coulomb-type plastic yield function for dry material in Chapter 3 is updated for each family of weakness sliding planes saturated by water by:

$$f^{p,r}(\sigma_n^r, \sigma_t^r, \gamma^{p,r}, p) = \sigma_t^r + \alpha^{p,r}\tilde{\sigma}_n^r - c \leq 0, \tag{5.9}$$

and in a similar way, the plastic flow rule using the equivalent local normal stress is now given as:

$$g^{p,r}\left(\sigma_t^r, \sigma_n^r, \gamma^{p,r}, p\right) = \sigma_t^r + \eta^{p,r}\tilde{\sigma}_n^r = 0 \tag{5.10}$$

As mentioned in Chapter 3, plastic flow and damage evolution are inherently coupled each other. Precisely, the damage evolution is mainly induced by cumulated plastic sliding along surfaces of defects. Therefore, the damage criterion for saturated porous media is the same as the one for dry material, i.e.:

$$f^{\omega,r} = d^r - \left(1 - e^{-a_4\gamma^{p,r}}\right) \leq 0 \tag{5.11}$$

5.1.3 Characterization of coupling porous system

The two internal state variables ε_{ij}^p and ϕ^p are independent. However, for the sake of simplicity, it is assumed that the plastic porosity is proportional to plastic deformation (Coussy, 2004):

$$\phi^p = \mu_{ij}\varepsilon_{ij}^p \tag{5.12}$$

Further, from purely macroscopic considerations, some (unproven) kinematical hypotheses may be formulated. The plastic porosity is then simplified by taking an isotropic form for μ_{ij}:

$$\phi^p = \mu\delta_{ij}\varepsilon_{ij}^p = \mu\, tr(\varepsilon^p) \tag{5.13}$$

where μ is used to define the ratio between the volume plastic deformation and plastic porosity. The case that μ=1 corresponds to a plastically incompressible matrix while the case that μ approaches to the initial porosity ϕ_0 corresponds to a volumetric plastic strain of the skeleton frame only due to the solid matrix. It is then consistent to require μ satisfying the inequalities $\phi_0 \leq \mu \leq 1$. Kerbouche et al. (1995) have performed some coupling hydrostatic compression tests in order to determine the value of μ and found that the coefficient μ is changed in the process of plastic deformation. For simplicity, a constant scalar is used in the present model. Therefore, the constitutive laws (5.5) and (5.6) is recast into the following form:

$$\boldsymbol{\sigma} = \mathbb{C}^u(\mathbf{d}) : (\varepsilon - \varepsilon^p) - M(\mathbf{d})\boldsymbol{b}(\mathbf{d})[\phi - \mu \operatorname{tr}(\varepsilon^p)] \tag{5.14}$$

$$p = M(\mathbf{d})\left[-\boldsymbol{b}(\mathbf{d}) : (\varepsilon - \varepsilon^p) + \left(\phi - \operatorname{tr}(\varepsilon^p)\right)\right] \tag{5.15}$$

where $\mathbb{C}^u(\mathbf{d})$ is the fourth rank effective elastic tensor under undrained condition, which is linked to the drained effective elastic tensor by the following expression (Thompson and wills, 1991):

$$\mathbb{C}^u(\mathbf{d}) = M(\mathbf{d})\boldsymbol{b}(\mathbf{d}) \otimes \boldsymbol{b}(\mathbf{d}) \tag{5.16}$$

Note that the effective elastic tensor under undrained condition exhibits the same symmetries as the drained one, i.e. $C^u_{ijkl} = C^u_{jikl} = C^u_{ijlk} = C^u_{klij}$. Further, we deduce the classic definition of Biot's effective stress tensor by moving the second term of the right-hand side of Eq. (5.5) to the left-hand side:

$$\tilde{\boldsymbol{\sigma}} = \boldsymbol{\sigma} - \boldsymbol{b}(\mathbf{d})p \tag{5.17}$$

and the constitutive stress-strain relation under the drained condition becomes:

$$\tilde{\boldsymbol{\sigma}} = \mathbb{C}(\mathbf{d}) : (\varepsilon - \varepsilon^p) \tag{5.18}$$

For any stationary damage state, the effective elastic tensor of skeleton frame is obtained in the proceeding part. Following the micromechanical analyses conducted by Thompson and Willis (1991) and Cheng (1997) for initially anisotropic porous media, the macroscopic poroelastic constants can be deduced from the microscopic properties of the constituents of porous medium. Similar analyses can be employed for a damaged induced anisotropic porous material in a given damage state. By considering the deformation of the saturated porous medium on microscopic scale within the appropriate representative elementary volume, the following relationships have been obtained (for more details, see Thompson and Willis (1991) and Cheng (1997)):

$$b_{ij}(\mathbf{d}) = \delta_{ij} - C_{ijkl}(\mathbf{d})S^s_{klmm}, \tag{5.19}$$

$$M(\mathbf{d}) = \frac{1}{2C_{ijmn}(\mathbf{d})S^s_{mnll}\left[S_{ijkk}(\mathbf{d}) - S^s_{ijkk}\right] + \phi(c_f - \lambda^s_{ii})} \tag{5.20}$$

In the above equations, S^s_{ijkl} is the fourth rank elastic compliance tensor of solid grains, which is assumed to be constant.; the second rank symmetric tensor λ^s_{ij} is introduced to describe

heterogeneous strains of solid grains under pore pressure; c_f denotes the compressibility coefficient of the fluid and ϕ the porosity of material. To simplify the above relations, two fundamental assumptions are customarily used. The first called 'micro-homogeneity', assumes that the skeleton of porous material is homogeneous on the pore (microscopic) scale and the material can be heterogeneous on the macroscopic scale due to different micro-homogeneous materials distributed in space (Nur and Byerlee, 1991). The second one named 'micro-isotropy' argues that the solid constituent of the porous medium is isotropic at the microscopic (pore and grain) level and the macroscopic material anisotropy is of structural origin, mainly resulting from oriented pore and fissure arrangement. By adopting these assumptions, the above relationships are simplified as follows (Cheng, 1997):

$$b_{ij}(\mathbf{d}) = \delta_{ij} - \frac{C_{ijkk}(\mathbf{d})}{3k_s} \tag{5.21}$$

$$M(\mathbf{d}) = \frac{k_s}{(1 - k^*(\mathbf{d}) / k_s) - \phi(1 - k_s / k_f)} \tag{5.22}$$

$$k^*(\mathbf{d}) = \frac{\mathbf{C}^b_{iijj}(\mathbf{d})}{9} \tag{5.23}$$

where k_s and k_f are respectively the bulk modulus of the solid grains and pore fluid.

5.2 Identification of the model parameters

The anisotropic poroplastic damage model is applied to maroon sandstone (Karami, 1998) sampled from the region of the Vosges Mountain in France. It is a typical brittle rock with the average density at about 2.06g/cm^3 and the initial average porosity about $\phi_0 = 20\%$. Hydrostatic compression tests have shown that it is initially quasi-isotropic. The initial elastic constants are: $E^0 = 24000\mathrm{MPa}$ and $\nu^0 = 0.20$. The bulk modulus of the solid grains k_s is determined by hydrostatic compression test under partially drained condition. The bulk modulus of the pore fluid k_f can not be measured directly; we can calculate its value by the following equation:

$$k_f = \frac{\phi_0 B^s k^s}{(1-B^s)k^s / k^0 + (1+\phi_0)B^s - 1}, \quad k^0 = \frac{E^0}{3(1-2\nu^0)} \tag{5.24}$$

The value of Skempton coefficient B_s can be determined by hydrostatic compression under undrained condition. The values of bulk modulus of the solid grain and pore fluid are $k_s = 52300\text{MPa}$ and $k_f = 1790\text{MPa}$, respectively.

The determination of the 12 model parameters c_0, H_1, a_1, α_f^p, α_o^p, a_2, η_f^p, η_0^p, a_3, a_4, κ_1 and κ_2 for dry material has been clarified in Section 2. There are still 3 model parameters b^0, a_6 and μ involved in coupling system, among which b^0 and a_6 are used to define the effect of the pore pressure on the local normal stress. It is then possible to let the value of b^0 equal to the initial Biot's coefficient of sound porous material. b_5 can be determined by back analysis on the evolution from the initial value to its maximum one. According to the experimental study (Kerbouche et al., 1995), $\mu = 0.3$ is used in this work. Typical values of model parameters are summarized in Table 5.1.

Table 5.1 Typical values of parameters of coupled poroplastic damage model

dry material												coupling system		
c_0(MPa)	H_1(MPa)	a_1	α_0^p	α_f^p	a_2	η_o^p	η_f^p	a_3	a_4	κ_1	κ_2	b^0	a_6	μ
10.0	464	30	0.1	0.78	600	-0.1	0.28	300	100	0.5	1.0	0.5	50	0.3

5.3 Simulation results

In cylindrical triaxial loading, samples are subjected to axisymmetric compression stresses $\sigma_{22} = \sigma_{33}$, accordingly we have $\varepsilon_{22} = \varepsilon_{33}$. In the following part, drained triaxial tests, undrained triaxial tests and tests of strain response to pore pressure change on saturated Vosges sandstone are simulated.

5.3.1 Drained triaxial tests

In the case of drained triaxial compression tests, the stress loading is applied and the pore pressure keeps equal to atmospheric pressure and is considered as zero. Therefore, the constitutive (5.5) for skeleton frame becomes:

$$\boldsymbol{\sigma} = \mathbb{C}(\mathbf{d}) : (\varepsilon - \varepsilon^p) \tag{5.25}$$

In Fig.5.1, comparisons between numerical predictions and test data for triaxial compression tests with different confining pressures under drained condition are performed and a satisfactory agreement is observed. We can find that the proposed model is able to reproduce the basic mechanical behaviours.

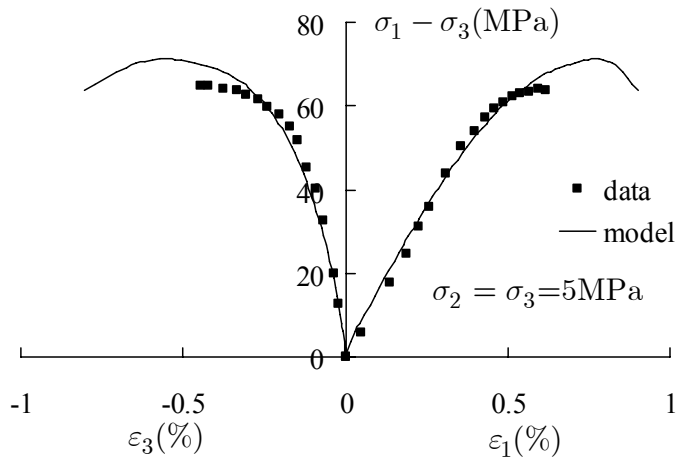

(a) Pc=5MPa

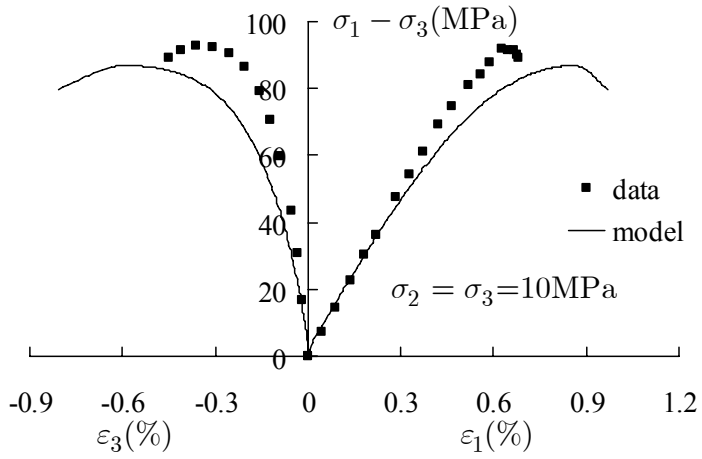

(b) Pc=10MPa

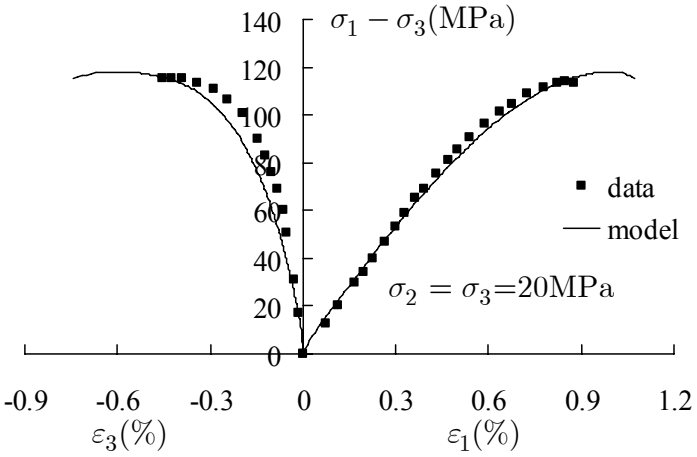

(c) Pc=20MPa

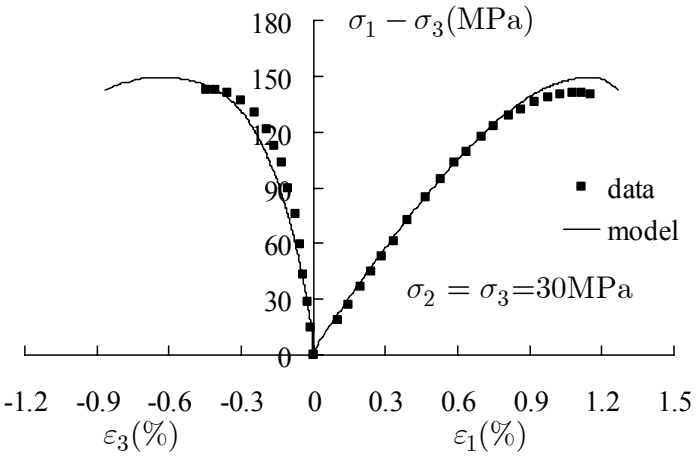

(d) Pc=30MPa

Fig. 5.1 *Triaxial drained tests (continuous lines are numerical values) with different confining stress, (a) Pc=5MPa, (b) Pc=10MPa, (c) Pc=20MPa,(d)Pc=30MPa*

5.3.2 Undrained triaxial tests

In undrained compression tests, there is no fluid injecting into or squeezing out of the sample; hence, we have $\phi = m / \rho_f^0 = 0$ in (5.15). The constitutive equations for coupling system are written as following:

$$\boldsymbol{\sigma} = \mathbb{C}^b(\mathbf{d}) : (\varepsilon - \varepsilon^p) - \boldsymbol{b}(\mathbf{d})p \tag{5.26}$$

$$p = M(\mathbf{d})[-\boldsymbol{b}(\mathbf{d}) : (\varepsilon - \varepsilon^p) - \mu \mathrm{tr}(\varepsilon^p)] \tag{5.27}$$

where both the Biot's coefficient $\boldsymbol{b}(\mathbf{d})$ and the Biot's modulus $M(\mathbf{d})$ are functions of damage variables and determined by (5.21) and (5.22), respectively.

In Fig.5.2, comparisons between numerical values and test data for triaxial compression tests under undrained condition are presented. There are good agreements in both strain-stress and pore pressure-stress relationship. Moreover, the behaviour called *'dilatancy hardening'* (Rudnicki, 1984) can also be described, especially under higher confining pressure. During the process from compaction to dilatancy under undrained condition, the pore pressure is first increased and then decreased due to the shear dilatancy. The decrease in pore pressure leads to the increase in local equivalent normal stress (see equation (5.8)) in all families of saturated weakness sliding planes and hence the sample exhibits hardening behaviour.

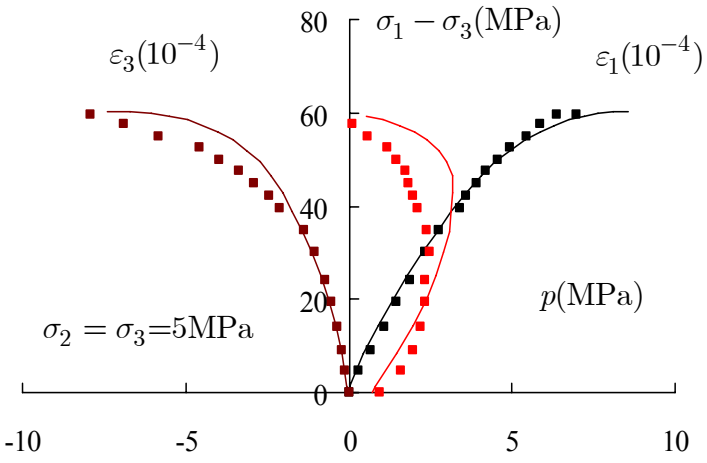

(a) Pc=5MPa

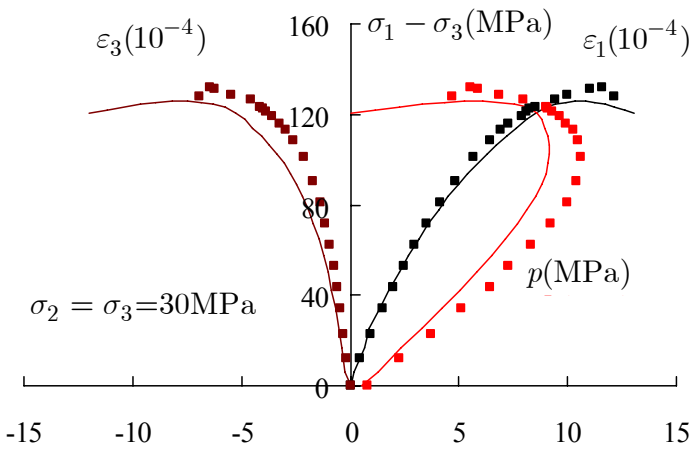

(a) Pc=30MPa

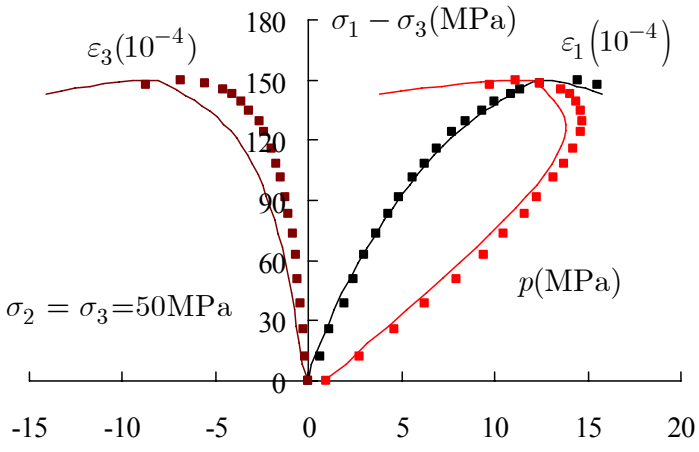

(a) Pc=50MPa

Fig. 5.2 *Undrained compression tests with different confining pressures (5, 30 and 50MPa)*

5.3.3 Strain responses to pore pressure

As mentioned in Chapter 1, in the test of strain response to the variation in pore pressure, saturated samples are first subjected to a classic triaxial compressive loading until a certain stress level, corresponding to a certain plastic deformation and damage level. Then, maintain the external stress state but inject water into the sample in order to increase the pore pressure. The axial and radial strains are measured as the pore pressure increases. Note that in the second phase there is no stress increment, the strain variation is then totally due to the variation in pore

pressure and :

$$\Delta\varepsilon^e = \mathbb{S}^b(\mathbf{d}) : \boldsymbol{b}(\mathbf{d})\Delta p \tag{5.28}$$

$$\Delta\varepsilon = \Delta\varepsilon^e + \Delta\varepsilon^p \tag{5.29}$$

where $\Delta\varepsilon^p$ is the plastic strain increment. Under the effect of pore pressure, the microcracks may continue to propagate, consequently cause the further plastic deformation and damage in material. The plastic strain could be determined by the plastic yield and potential functions.

Fig. 5.3 shows numerical simulation on the test of strain response to the change of pore pressure at three different deviatoric stresses under the same confining pressure of 40MPa, there is good agreement between the numerical result and the test data. It is easily seen that the strains induced by variation in pore pressure are significantly anisotropic. More precisely, the extent in the radial one is much greater than that in the axial one. Moreover, at higher damage levels (deviatoric stress values), the change of axial strain due to positive variation in pore pressure may be compressive (positive sign in figure).

Complementary numerical simulations on the test of strain response to pore pressure increment under confining pressures of 10, 20, 30 and 50MPa are provided in Appendix B.

5.4 Conclusions

Based on the discrete plastic damage model, a coupled anisotropic poroplastic damage model has been developed for modelling poromechanical behaviours in porous geomaterials under undrained condition. The known stress equivalence principle is employed to define the effect of pore pressure on the local stress for each family of weakness sliding planes. The plastic yield and potential functions formulated for dry materials are extended to the saturated undrained case; the complementary variable of plastic porosity is introduced and linked to the volume plastic deformation. This model is applied to Vosges sandstone. Simulations on undrained compression tests and strain response to the variation in pore pressure show good agreement. Finally, the ‘dilatancy hardening’ effect, commonly appeared in undrained compression tests, has been numerically reproduced.

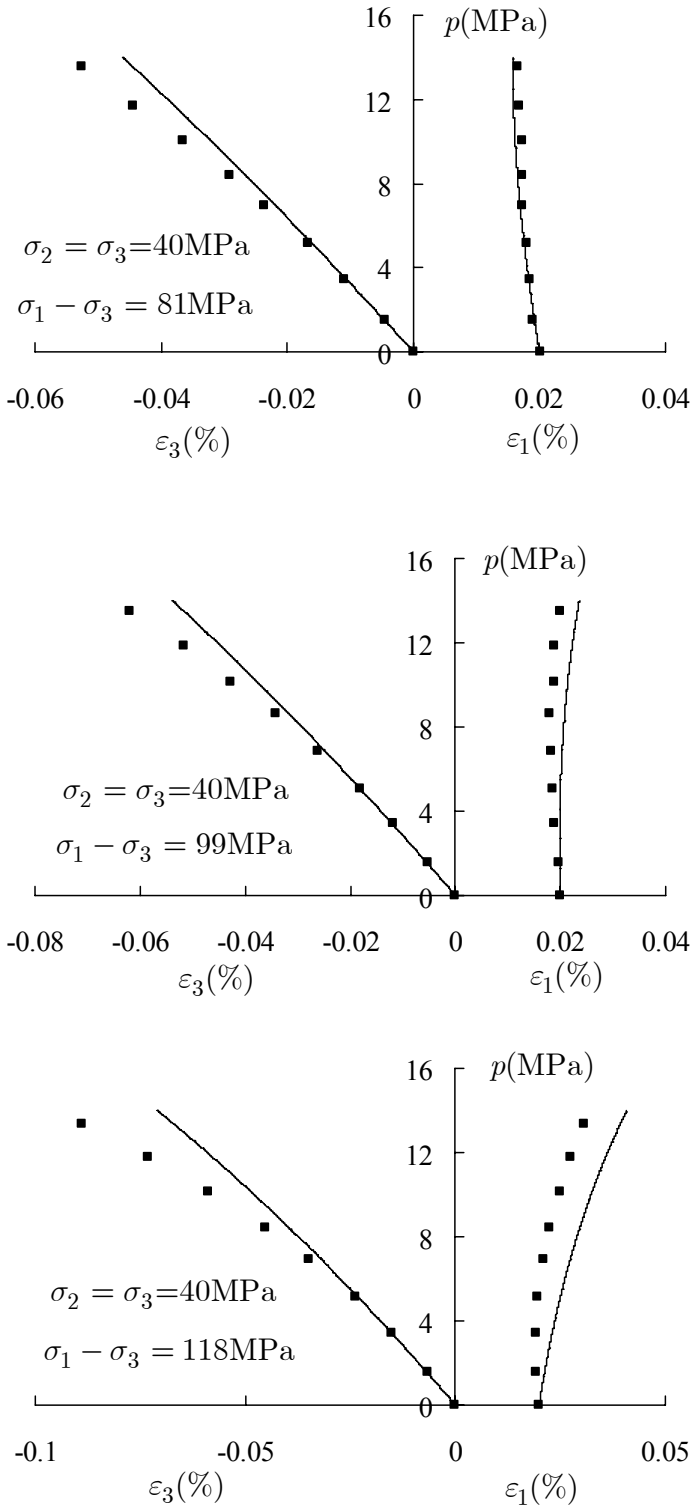

Fig. 5.3 *Strain response to pore pressure increment at different deviatoric stress (81, 99 and 118MPa) with confining pressure 40MPa*

Conclusions and Perspectives

The main objective of the work presented consists in systematic experimental and numerical investigations on mechanical and especially poromechanical behavior of brittle geomaterials. It consists of the following 4 parts: (i) experimental studies on mechanical behaviours, Biot's coefficient and intrinsic permeability of sandstone in saturated conditions, (ii) development of discrete plastic damage model and numerical simulation of mechanical behavior for dry sandstone, (iii) modeling of poroelastic behaviours under compressive loading, including the variation of Biot's coefficients and permeability of saturated sandstone, (iv) presentation of anisotropic poroplastic damage model and numerical simulation of poromechanical behavior. Some details are addressed as follows:

After an introductive review on some previous experimental and numerical works on mechanical and poromechanical behaviors of brittle geomaterials, we have investigated experimentally in Chapter 2 the basic mechanical behaviours, determination of Biot's coefficients and intrinsic permeability of sandstone in saturated conditions. Hydrostatic compression tests and a serie of triaxial compression tests with different confinements have been performed. Under compressive stresses, the initial defects are progressively closed leading to non linear stress-strain relations. When deviatoric stresses are applied, propagation of existing microcracks and nucleation of new ones take place after the onset of damage criterion. Similar to existing results, the propagation of microcracks is mainly oriented in the axial direction in conventional triaxial compression tests. The oriented induced damage affects Biot's coefficient in the axial direction much more significantly than in the lateral one. It is also shown that there exists some correlation between the permeability change and volumetric deformation as well as effective mean stress. The influence of volumetric dilatancy on permeability is not significant during the diffuse regime of damage. However, in the phase of the coalescence of microcracks, induced damage can affect considerably rock permeability. All these experimental results have been successfully simulated in later numerical parts.

In chapter 3, the discrete thermodynamic approach has been adopted for modeling of anisotropic plastic damage behaviours of brittle geomaterials. The discrete formulation allows

taking into account physical mechanisms involved in plastic deformation and damage evolution. The modified Coulomb-type plastic yield and plastic potential function, as well as the damage evolution criterion proposed by Mazars, are applied to each family of weakness planes. The proposed model was used to simulate the mechanical tests, including triaxial compression tests, lateral extension tests and proportional loading tests. A good agreement between numerical predictions and experimental data is obtained. The proposed model is able to describe the main features observed in brittle geomaterials under compression-dominated stresses. It is more important to note that induced anisotropy in both plastic flow and damage evolution can be easily described.

In Chapter 4, the discrete model has been applied to simulate the mechanical behaviour, poroelastic properties and permeability of saturated sandstones. In permeability characterization, rock permeability is divided into the part of matrix permeability and that induced by cracks. The evolution of axial permeability is well simulated during triaxial compression tests under different confining pressures. Biot's coefficients is written as function of effective elastic stiffness tensor and bulk modulus of the solid matrix, the comparisons between the numerical simulation and test data shows that the proposed model is able to describe the anisotropic property of Biot's coefficients.

In the last part, in order to describe the poromechanical behaviour of saturated sandstones, the basic model is then extended to poroplastic damage one. The well-known stress equivalence principle is employed to define the effect of the pore pressure on the local normal stress for each family of weakness sliding planes. We have updated the plastic yield and potential functions for saturated media by introducing the equivalent local normal stress therein. The complementary variable of plastic porosity is adopted and related to the volume plastic deformation. This model has been applied to Vosges sandstone to simulate undrained compression tests and pore pressure controlled tests, a good agreement has been obtained including the 'dilatancy hardening' behaviour and anisotropic strain response to pore pressure increment.

In conclusion, the research purpose initiated by the present work has been completely achieved. Future extensions along this line include the following two parts:

- On experimental aspects, further laboratory researches will be dedicate to investigating the evolution of poromechancical behaviours and fluid transport properties in multi-physical coupling loading conditions. These tests are quite difficult in laboratory but of practical interests to many engineering problems, such as geological storage of nuclear wastes, sequestration of carbon and residual gas, oil and gas production in complex conditions etc.
- On numerical aspects, the developed anisotropic poroplastic damage model will be implemented into a finite element code for large validations, particularly by stability and durability analysis on engineering structures.

References

[1] Abousleiman Y., Cheng A.H.D., Cui L., Detournay E., Roegiers J.C. (1996). *Mandel's problem revisited*. Geotechnique 46 (2): 187-195.

[2] Atkin R.J., Craine R.E. (1976). *Continuum theories of mixtures: basic theory and historical development.* The Quarterly Journal of Mechanics and Applied Mathematics 29: 209-244.

[3] Bazant Z.P., Oh B.H. (1985). *Microplane model for progressive fracture of concrete and rock*. Journal of Engineering Mechanics, ASCE 11(4): 559-582.

[4] Bazant Z.P., Oh B.H. (1986). *Efficient numerical integration on the surface of a sphere*. Z.A.M.M., 66: 37-49.

[5] Bazant Z.P. and Zi G. (2003). *Microplane constitutive model for porous isotropic rocks*. International Journal for Numerical and Analytical Methods in Geomechanics 27: 25-47.

[6] Baud P., Schubnel A., Wong T.-F. (1999). *Dilatancy, compaction, and failure mode in Solnhofen limestone*. Journal of Geophysical Research, 105(B8): 19289-19303.

[7] Bear J. (1972). *Dynamics of Fluids in Porous Media*. American Elsevier, New York.

[8] Berryman JG. (1992). *Effective stress for transport properties of inhomogeneous porous rock*. Journal of Geophysical Research 97:17409-17424.

[9] Biot M.A. (1935), *Le problème de la consolidation des matières argileuses sous une charge*, Ann. Soc. Sci. Bruxelles, B55 : 110-113.

[10] Biot M.A. (1941). *General theory of three dimensional consolidation*. Journal of Applied Physics 12: 155-164.

[11] Biot M.A. (1955). *Theory of elasticity and consolidation for a porous anisotropic solid*. Journal of Applied Physics 26: 182-185.

[12] Biot M.A. (1962). Mechanics *of deformation and acoustic propagation in porous media*. Journal of Applied Physics 33: 1482-1498.

[13] Biot M.A. (1973). Non *linear and semi-linear rheology of porous solids.* J. of Geophy. Res. 78(23): 4924-493.

[14] Bossart P., Meier P.M., Moeri A., Trick T. and Mayor J.C., (2002). *Geological and hydraulic characterisation of the excavation disturbed zone in the Opalinus Clay of the Mont Terri Rock Laboratory*. Eng Geol 66 1–2, pp. 19–38.

[15] Bowen R.M. (1982). *Compressible porous media models by use of the theory of mixtures*. International Journal of Engineering Science 20: 697-735.

[16] Brace W.F., Martin RJ. (1968a). *A test of the law of effective stress for crystalline rocks of low porosity.* International Journal of Rock Mechanics and Mining Sciences 5:415-426

[17] Brace W.F., Walsh J.B., Frangos W.T. (1968b). *Permeability of granite under high pressure*. Journal of Geophysical Research 73: 2225-2236.

[18] Budiansky B., O'Connell R. (1976). *Elastic moduli of a cracked solid*. International Journal of Solids and Structures 12: 81-97.

[19] Berryman, J. G., and S. C. Blair, (1987). *Kozeny-Carman relations and image processing methods for estimating Darcy's constant*. J. Appl. Phys., 62, 2221-2228.

[20] Carman, P. C. (1956). *Flow of Gases Through Porous Media*, 182 pp., Academic, San Diego, Calif..

[21] Carrol M.M., (1979). *An effective stress law for anisotropic elastic deformation*. Journal of Geophysical Research 84: 7510-7512.

[22] Carol I., Bazant ZP. (1997). *Damage and plasticity in microplane theory*. International Journal of Solids and Structures 34(29): 3807-3835.

[23] Carol I., Jirasek M., Bazant ZP. (2001). *A thermodynamically consistent approach to microplane theory: Part I. Free energy and consistent microplane stresses*. International Journal of Solids and Structures 38: 2921-2931.

[24] Carmeliet J. (1998). *On the poro-visco-elastic and damage coupling in non saturated media*, In Proceeding of Biot Conference, Thimus et al. (eds.), Balkema, Rotterdam, 41-46.

[25] Chang C.S., Hicher P.-Y. (2005). *An elasto-plastic model for granular materials with microstructural consideration*. International Journal of Solids and Structures 42: 4258-4277

[26] Cheng, A.H.-D., (1997). *Material coefficients of anisotropic poroelasticity*. International Journal of Rock Mechanics and Mining Sciences 34 (2): 199-205.

[27] Chiarelli A.S., Shao J.F. and Hoteit N. (2003). *Modelling of elastoplastic damage behaviour of a claystone*. International Journal of Plasticity 19: 23-45

[28] Chiu HK, Johnston IW, Donald IB. (1983). *Appropriate techniques for triaxial testing of saturated soft rock*. International Journal of Rock Mechanics and Mining Sciences 20 : 107-120

[29] Coussy O. (1995). Mechanics of Porous Continua. Wiley, New York.

[30] Coussy O., Dormieux L., Detournay E. (1998). *From mixture theory to Biot's approach for porous media*. International Journal of Solids and Structures 35: 4619-4635.

[31] Coussy O. (2004). *Poromechanics*. John Wiley & Sons UK.

[32] Crochet M.J., Naghdi P.M. (1966). *On constitutive equations for flow of fluid through an elastic solid*. International Journal of Engineering Science 4: 383-401.

[33] Cudny M., Vermeer P.A. (2004). *On the modelling of anisotropy and destructuration of soft clays within the multi-laminate framework*. Computer and Geotechnics 31: 1-22

[34] Cui L., Cheng A.H.D., Kaliakin V.N., Abousleiman Y., Roegiers J.C. (1996) *Finite element analyses of anisotropic poroelasticity: A generalised Mandel's problem and an inclined borehole problem*. International Journal for Numerical and Analytical Methods in Geomechanics 20: 381-401.

[35] Lydzba D., Shao J.F. (2000). *Study of Poro-Elasticity Material Coefficients as Response of Microstructure.* Mechanics of Cohesive-frictional Materials 5: 149-171.

[36] David, C., Wong, T.-f., Zhu, W. and Zhang, J., (1994). *Laboratory measurement of compaction-induced permeability change in porous rocks: implications for the generation and maintenance of pore pressure excess in the crust*, PAGEOPH, 143, 425-456.

[37] De Buhan P., Dormieux L. and Salençon J. (1992). *A theoretical approach to the ultimate limit state design*. Int. Symp. on "Limit State Design in Geotechnical Engineering", Copenhagen, Danish Geotechnical Society, 429-438.

[38] Detournay E., Cheng A.H.-D. (1993). *Fundamentals of poroelasticity*. In: Fairhurst, C. (Ed.), Comprehensive Rock Engineering: Principles, Practice and Projets, 2, Analysis and Design Methods. Pergamon Press, Oxford, pp.113-171.

[39] Dormieux L, Kondo D. (2004). *Approche micromécanique du couplage perméabilité-endommagement*. Comptes Rendus Mécanique 332: 135-140.

[40] Dormieux L., Kondo D. (2005). *Poroelasticity and damage theory for cracked media*, in Applied Micromechanics of Porous Media, CISM lecture notes, L. Dormieux and F.J. Ulm (eds.), Springer, 153-183.

[41] Dormieux L., Kondo J. and Ulm F.-J., (2006). *Microporomechanics*. J. Wiley, Chichester, UK.

[42] Dragon A. and Mroz Z. (1979). *A continuum model for plastic-brittle behaviour of rock and concrete.* International Journal of Engineering Science 17: 121-137

[43] Dropek R.K., Johnson J.N., Walsh J.B. (1978). *The influence of pore pressure on the mechanical properties of Kayenta sandstone*. Journal of Geophysical Research 83: 2817-2824

[44] Elata D., Rubin M.B. (1995). *A new representation for the strain energy of anisotropic elastic materials with application to damage evolution in brittle materials*. Mechanics of Materials 19: 171-192.

[45] Fabre D., Gustkiewicz J. (1997). Poroelastic Properties of Limestones and Sandstones under Hydrostatic Conditions, Int. J. Rock Mech. Min. Sci. 34(1), 127-134

[46] Fauchet B. (1991). *Analyse poroplastique des barrages en béton et de leur fondation, Rôle de la pression interstitielle*. Doctoral thesis, Ecole National des Ponts & Chaussées.

[47]Fredrich, J.T., Evans, B., Wong, T.F., (1989). *Micromechanics of the brittle to plastic transition in Carrara marbe*. J. Geophys. Res. 94, 4129-4145

[48] Gambarotta L., Lagomarsino S. (1993). *A microcrack damage model for brittle materials*. International Journal of Solids and Structures 30(2): 177-198.

[49] Gatto, H.G. (1984). *The effect of various states of stress on the permeability of Berea sandstone*, M.S. thesis, Texas A&M Univ., College Station.

[50] Ghabezloo S., Sulem J., Guedon S., Martineau F. (2009). *Effective stress law for the permeability of a limestone*, International Journal of Rock Mechanics & Mining Sciences 46, 297–306

[51] Green D.H., Wang H.F. (1986). *Fluid pressure response to undrained compression in saturated sedimentary rock*. Geophysics 51: 948-956

[52] Hajiabdolmajid V.R. (2001). *Mobilization of strength in brittle failure of rock*. Doctoral Thesis, Queen's University.

[53] Hallbauer D.K., Wagner H., Cook N.G.W. (1973). *Some observations concerning the microscopic and mechanical behavior of quartzite specimens in stiff, triaxial compression tests*. International Journal of Rock Mechanics and Mining Sciences & Geomechanics Abstracts 10: 713-26.

[54] Halm D. and Dragon A., (1998). *An anisotropic model of damage and frictional sliding for brittle materials*. Euro. J. Mech. A/Solids 17, pp. 439–460.

[55] Hayakawa K., Murakami S. (1997). *Thermodynamical modeling of elastic-plastic damage and experimental validation of damage potential*. International Journal of damage mechanics 6: 333-363

[56] Hart D.J., Wang H.F. (2001). *A single test method for determination of poroelastic constants and flow parameters in rocks with low hydraulic conductivities*, International Journal of Rock Mechanics & Mining Sciences 38, 577–583

[57] Heck WJ. (1972). *Development of equipment for studying pore pressure effects in rock*. In: Gray KE (ed) Basic and applied rock mechanics. Proc. 10th Symp. Rock Mech., Austin, Texas, May 1968. A.I.M.E., New York, pp 243-266.

[58] Hill R. (1965). *Continuum micromechanics of elastoplastic polycrystals*. Journal of the Mechanics and Physics of Solids 13: 89-101.

[59] Hill R. (1966). *Generalized constitutive relations for incremental deformations of metal crystals by multi-slip*. Journal of the Mechanics and Physics of Solids 14: 95-102.

[60] Horii, H., Nemat-Nasser, S. (1985). *Compression-induced microcrack growth in brittle solids: axial splitting and shear failure*. J. Geophys. Res. 90(B4), 3105-3125

[61] Hubert M.K., (1940). *The theory of groundwater motion.* J. Geol. 48: 785-944.

[62] Ismail IAH., Murrell SAF. (1976). *Dilatancy and the strength of rocks containing pore water under undrained conditions*. Geophys J Roy Astr S 44: 107-134

[63] Ju J.W. (1989). *On energy based coupled elastoplastic damage theories: constitutive modeling and computational aspects.* Int. J. Solids Structures 25(7): 803-833

[64] Kachanov M. (1982). *A microcrack model of rock inelasticity - Part I: frictional sliding on microcracks; Part II: propagation of microcraks*. Mechanics of Materials 1: 19-41.

[65] Kachanov M. (1993). *Elastic solids with many cracks and related problems*, In: Advances in applied mechanics, vol. 30, Hutchinson and Wu (eds.), NY, pp.259-445.

[66] Karami H. (1998). *Experimental investigation of poroelastic behaviour of a brittle rock*. Doctoral Thesis, University of Lille I, to appear (in French).

[67] Katsube N., Carroll M.M. (1987). *The modified mixture theory for fluid-filled porous materials: theory.* J. Appl. Mech. 54: 35-40.

[68] Kerbouche R., Shao J.F., Skozylas F., Henry J.-P. (1995). *On the poroplastic behaviour of porous rocks*. European Journal of Mechanics, A/Solids 14(4): 3577-3587.

[69] Khazraei R. (1995). *Experimental investigations and numerical modelling of the anisotropic damage of a Vosges sandstone*. Doctoral Thesis, University of Lille I (in French).

[70] Lemaitre J. (1996). *A Course on Damage Mechanics*, second edition, Springer.

[71] Lion M., Skoczylas F., Ledesert B. (2004). *Determination of the main hydraulic and poro-elastic properties of a limestone from Bourgogne, France*, International Journal of Rock Mechanics & Mining Science 41, 915–925

[72] Lydzba D. and Shao J.F., (2000). *Study of poroelasticity material coefficients as response of microstructure*. Mech. Cohesive-Frictional Materials 5, pp. 149–171.

[73] Martin C.D., Chandler N.A., *The progressive failure of Lac du Bonnet granite*. Int J Rock Mech Min Sci. 31(6) : 643-659.

[74] Mazars J. (1986). *A description of micro- and macroscale damage of concrete structures*. International Engineering Fracture Mechanics 25: 729-737

[75] Moore D.E., Lockner D.A. (1995). *The role of microcracking in shear fracture propagation in granite.* Journal of Structural Geology 17: 95-114.

[76] Morland L.W. (1972). *A simple constitutive theory for a fluid-saturated porous solid*. J. Geophys. Res. 77: 890-900.

[77] Nur A., Byerlee J.A. (1971). *An exact effective stress law for elastic deformation of rock with fluids*. J. Geophys. Res. 76: 6414-6419.

[78] Oda M, Takemura T, Aoki T. (2002). *Damage growth and permeability change in triaxial compression tests of Inada granite*. Mechanics of Materials 34: 313-331.

[79]Olsson W. (1995). *Development of anisotropy in the incremental shear moduli for rock undergoing inelastic deformation*. Mechanics of materials, 21: 231-242.

[80] Pande G.N. and Sharma K.G. (1983). *Multi-laminate model of clays: a numerical evaluation of the influence of rotation of the principal stress axes*. International Journal for Numerical and Analytical Methods in Geomechanics, 7 (4): 397-418

[81] Paterson MS. (1958). *Experimental deformation and faulting in Wombeyan marble*. Geol Soc Am Bull 69: 465-476.

[82] Paterson M S. (1983). *The equivalent channel model for permeability and resistivity in fluid-saturated rocks: A re-appraisal*. Mechanics of Materials, 2(4): 345－352.

[83] Paterson Mervyn S., Wong T.-F. (2005). *Experimental Rock Deformation - The Brittle Field*. Springer Berlin Heidelberg, New York.

[84] Peach, C.J. and Spiers, C.J. (1996). *Influence of plastic deformation on dilatancy and permeability development in synthetic salt rock*. Tectonophysics 256: 101–128.

[85] Pietruszczak S., Pande G.N. (2001). *Description of soil anisotropy based on multi-laminate framework*. International Journal for Numerical and Analytical Methods in Geomechanics 25: 197-206.

[86] Rendulic (1936). *Porenziffer und Porenwasserdrunk in Tonen*, Der Bauingenieur, 17, 559-564.

[87] Rice J.R., Cleary M.P. (1976). *Some basic btress diffusion solution for fluid saturated elastic porous media with compressible constituent*. Reviews of Geophysic & Space 14: 227-241.

[88] Rice J.R. (1970). *On the structure of stress–strain relations for time-dependent plastic deformation of metals*. Journal of Applied Mechanics ASME 37: 728-737

[89] Rice J.R. and Cleary M.P., (1976). *Some basic stress-diffusion solutions for fluid saturated elastic porous media with compressible constituents*. Rev. Geophys. Space Phys. 14: 227-241.

[90] Rice J.R., Cleary M.P. (1976). *Some basic btress diffusion solution for fluid saturated elastic porous media with compressible constituent*. Reviews of Geophysic & Space 14: 227-241.

[91] Robin P-YF, (1973). *Note on effective pressure*. Journal of Geophysical Research 78: 2434-2437.

[92] Rudnicki J.W. (1985). *Mechanics of Geomaterials: Rocks, Concretes, Soils*, John Wiley & Sons, UK.

[93] Rutter EH. (1972). *The effects of strain-rate changes on the strength and ductility of Solenhofen limestone at low temperatures and confining pressures*. Int J Rock Mech Min 9: 183-189.

[94] Schmitt DR., Zoback MD. (1992). *Diminished pore pressure in low-porosity crystalline rock under tensional failure: apparent strengthening by dilatancy*. J Geophys Res 97: 273-288

[95] Schmertmann JH., Osterberg JH. (1960). *An experimental study of the development of cohesion and friction with axial strain in saturated cohesive soils*. Research Conference on Shear Strength of Cohesive Soils. Boulder, CO, New York, American Society of Civil Engineers, pp.643-94.

[96] Schuller H., Schweiger H.F. (2002). *Application of a multi-laminate model to simulation of shear bande formation in NATM-tunnelling*. Computers and Geotechnics 7: 501-524.

[97] Schulze O., Popp T., Kern H., (2001). *Development of damage and permeability in deforming rock salt*. Engineering Geology 61: 163-180.

[98] Shao J.F. (1998). *Poroelastic behaviour of brittle rock materials with anisotropic damage*. Mechanics of Mechanics 30: 41-53.

[99] Shao J.F., Rudnicki J.W., (2000). *A microcrack-based continuous damage model for brittle geomaterials*. Mechanics of Materials 32: 607–619.

[100] Shao J.F., Zhou H., Chau K.T., (2005). *Coupling between anisotropic damage and permeability variation in brittle rocks*. International Journal for Numerical and Analytical Methods in Geomechanics 29: 1231-1247.

[101] Shao J.F., Jia Y., Kondo D., Chiarelli A.S., (2006). A *coupled elastoplastic damage model for semi-brittle materials and extension to unsaturated conditions*. Mechanics of Mechanics 38: 218-232.

[102] Simo J.C., Hughes T.J.R., (1998). *Computational Inelasticity*. Springer-Verlag, New York

[103] Skempton A.W. (1961). *Effective stress in soils, concrete and rocks*. In: Pore Pressure and suction in soils. Conference organized by Brit. National Soc. of Int. Soc. Soil Mech. Found. Eng. at Inst. of Civ. Eng., March 30-31, 1960. Butterworths, London, pp 4-16.

[104] Souley M., Homand F., Pepa S., Hoxha D. (2001). *Damage-induced permeability changes in granite: a case example at the URL in Canada*. International Journal of Rock Mechanics and Mining Sciences 38: 297-310.

[105] Steif, P.S., (1984). *Crack extension under compressive loading*. Engineering Fracture Mechanics 20(3): 463-473.

[106] Stormont, J.C. and Daemen, J.J.K. (1992). *Laboratory study of gas permeability changes in rock salt during deformation.* Int. J. Rock Mech. Min. Sci. and Geomech. Abstr. 29:325–342.

[107] Suzuki K., Oda M., Yamazaki M., Kuwahara T. (1998). *Permeability changes in granite with crack growth during immersion in hot water*. Int. J. Rock Mech. Min. Sci. 35(7): 907-921.

[108] Tapponier P., Brace W.F. (1976). *Development of stress-induced microcracks in Westerly granite*. International Journal of Rock Mechanics and Mining Sciences & Geomechanics Abstracts 13: 103-12.

[109] Taylor G.I., (1938). *Plastic strain in metals*. Journal of the Institute of Metals 62: 307-324.

[110] Terzaghi, K. (1923), *Die berechnung der durchlassigkeitsziffer des tones aus dem verlauf der hydrodynamischen spannungserscheinungen*, Sitz. Akad. Wissen., Wien Math. Naturwiss. Kl., Abt. IIa, 132, 105-124.

[111] Thompson M. and Willis J. R., (1991). *A reformulation of the equations of anisotropic poroelasticity*. Journal of Applied Mechanics ASME 58: 612-616.

[112] Trautwein U., Huenges E. (2005). *Poroelastic behaviour of physical properties in Rotliegend sandstones under uniaxial strain*, International Journal of Rock Mechanics & Mining Sciences 42, 924–932

[113] Walpole L.J. (1981). *Elastic behaviour of composite materials: theoretical foundations*. Advances in Applied Mechanics, C.S. Yih (ed.) 21: 169-242.

[114] Wang J.A., Park H.D., (2002). *Fluid permeability of sedimentary rocks in a complete stress-strain process*. Engineering Geology 63:291-300.

[115] Wong T.-F. (1982). *Micromechanics of faulting in Westerly granite*. International Journal of Rock Mechanics and Mining Sciences & Geomechanics Abstracts 19: 49-64.

[116] Wong T.-F. (1985). *Geometic probability approach to the characterization and analysis of microcracking in rocks*. Mechanics of Materials 4: 261-276.

[117] Wong T.-F., David C., Zhu W. (1997). *The transition from brittle faulting to cataclastic flow in porous sandstones: Mechanical deformation*. Journal of Geophysical Research 102(B2): 3009-3025.

[118] Zhang S. Cox S. F.&Paterson M. S. (1994). *The influence of room temperature deformation on porosity and permeability in calcite aggregates.* Journal of Geophysical Research, 9915761–15775.

[119] Zhou, J.-J. (2006). *Numerical modelling of the anisotropic damage and permeability evolution of rock*. Doctoral Thesis, University of Lille I (in French).

[120] Zhu Q.Z., Kondo D. and Shao J.F. (2008a). *Micromechanical analysis of coupling between anisotropic damage and friction in quasi brittle materials: role of the homogenization scheme*. International Journal of Solids and Structures 45: 1385–1405.

[121] Zhu Q.Z., Kondo D., Shao J.F., and Pensee V. (2008b). *Micromechanical modelling of anisotropic damage in brittle rocks and application*. International Journal of Rock Mechanics & Mining Sciences 45: 467–477.

[122] Zhu Q.Z., Shao J.F and Kondo D. (2008c) *A discrete thermodynamic approach for modeling anisotropic coupled plasticity-damage behavior in geomaterials*. Comptes rendus mecanique 336: 376-383.

[123] Zhu W., Wong T.-F. (1997a). *The transition from brittle faulting to faulting to cataclastic flow: permeability evolution*. Journal of Geophysical Research 102(B2): 3027-3041.

[124] Zhu W., Montesi L., Wong T.-F., (1997b). *Shear-enhanced compaction and permeability reduction: Triaxial extension tests on porous sandstone*. Mechanics of Materials 25: 199-214.

[125] Zoback M.D., Byerlee JD. (1975). *The effect of microcrack dilatancy on the permeability of Westerly granite.* Journal of Geophysical Research 80(B5): 752-755.

Appendix A

Selected material orientations used for numerical calculation of Eq. (3.8) are defined by the following 15 unit vectors (Elata and Rubin, 1995) and illustrated in Fig.A.1

$$\left.\begin{array}{ccc} \underline{n}^1 = \underline{e}_1 & \underline{n}^2 = \underline{e}_2 & \underline{n}^3 = \underline{e}_3 \\ \underline{n}^4 = r\underline{e}_1 + s\underline{e}_2 + t\underline{e}_3 & \underline{n}^8 = s\underline{e}_1 + t\underline{e}_2 + r\underline{e}_3 & \underline{n}^{12} = t\underline{e}_1 + r\underline{e}_2 + s\underline{e}_3 \\ \underline{n}^5 = r\underline{e}_1 - s\underline{e}_2 + t\underline{e}_3 & \underline{n}^9 = s\underline{e}_1 - t\underline{e}_2 + r\underline{e}_3 & \underline{n}^{13} = t\underline{e}_1 - r\underline{e}_2 + s\underline{e}_3 \\ \underline{n}^6 = r\underline{e}_1 - s\underline{e}_2 - t\underline{e}_3 & \underline{n}^{10} = s\underline{e}_1 - t\underline{e}_2 - r\underline{e}_3 & \underline{n}^{14} = t\underline{e}_1 - r\underline{e}_2 - s\underline{e}_3 \\ \underline{n}^7 = r\underline{e}_1 + s\underline{e}_2 - t\underline{e}_3 & \underline{n}^{11} = s\underline{e}_1 + t\underline{e}_2 - r\underline{e}_3 & \underline{n}^{15} = t\underline{e}_1 + r\underline{e}_2 - s\underline{e}_3 \end{array}\right\} \quad \text{(A.1)}$$

with $r = \frac{u}{2},\ s = \frac{1}{2},\ t = \frac{1}{2u}, u = \frac{\sqrt{5}+1}{2}$.

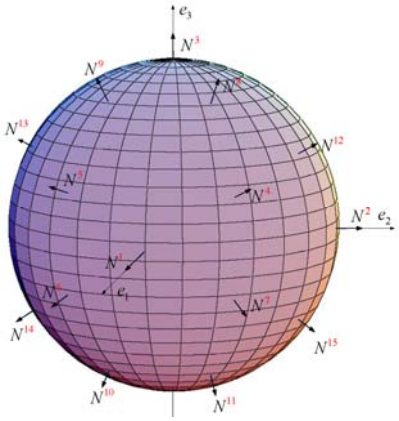

Fig. A.1 15 *integration orientations distributed on the surface of a unit sphere*

Appendix B

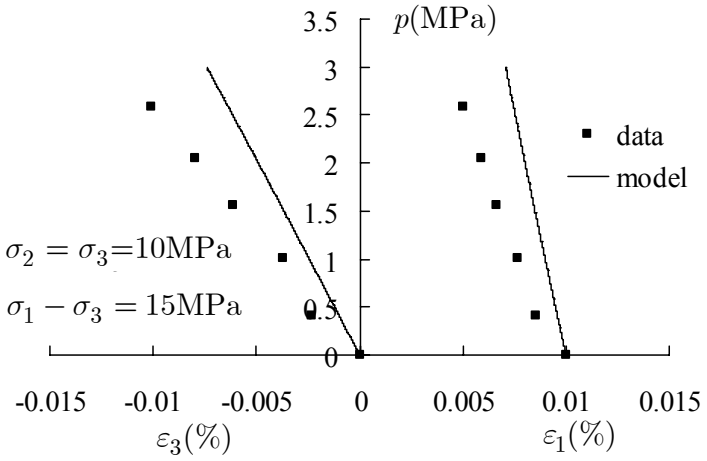

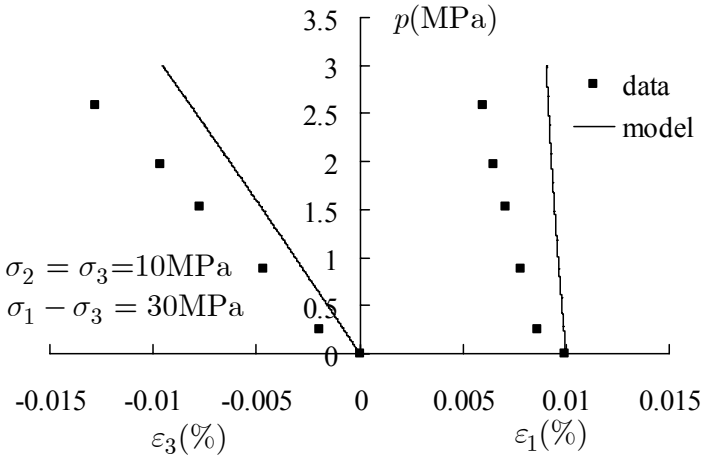

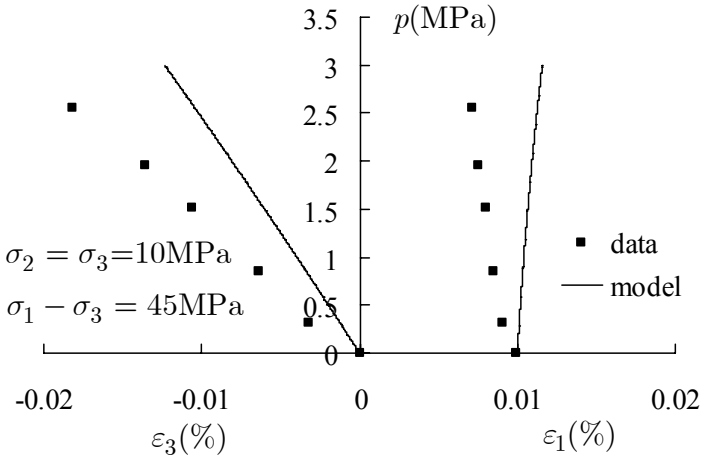

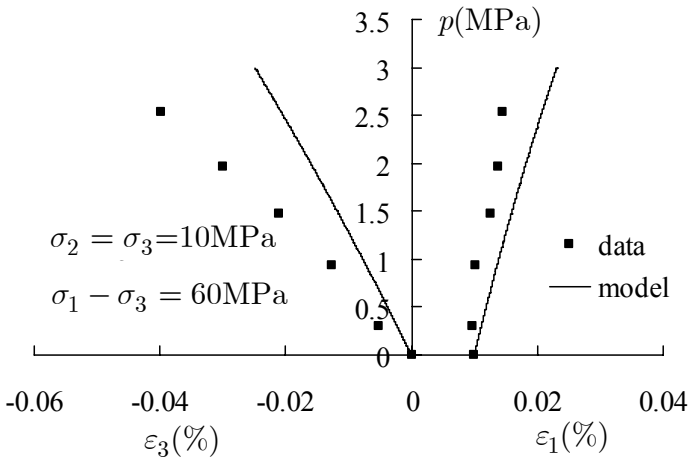

Fig. B.1 *Strain response to pore pressure increment at different deviatoric stress (15, 30, 45 and 60MPa) with confining pressure 10MPa*

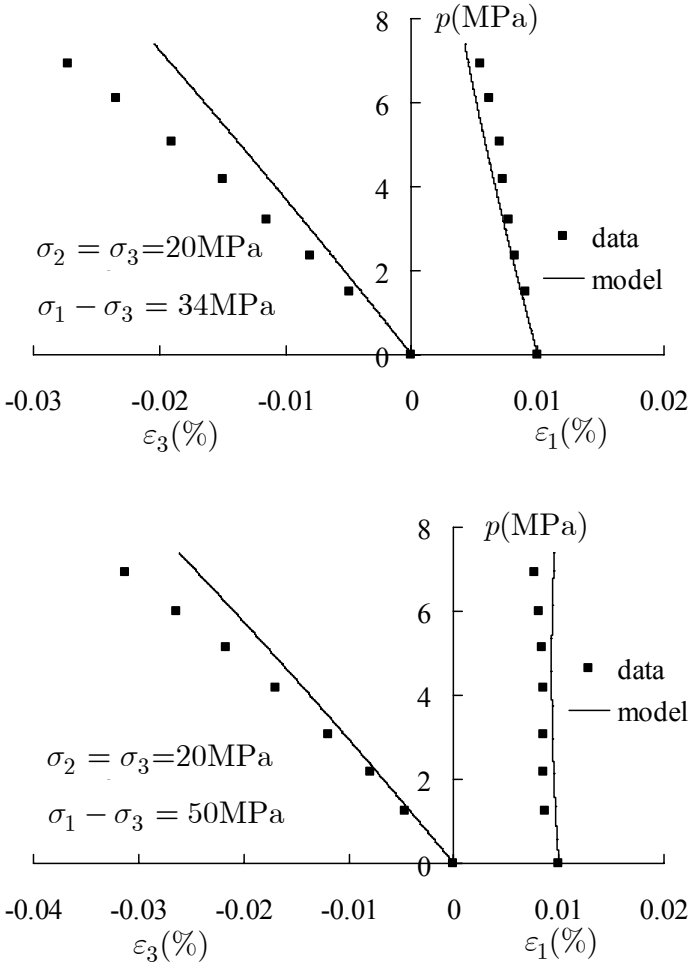

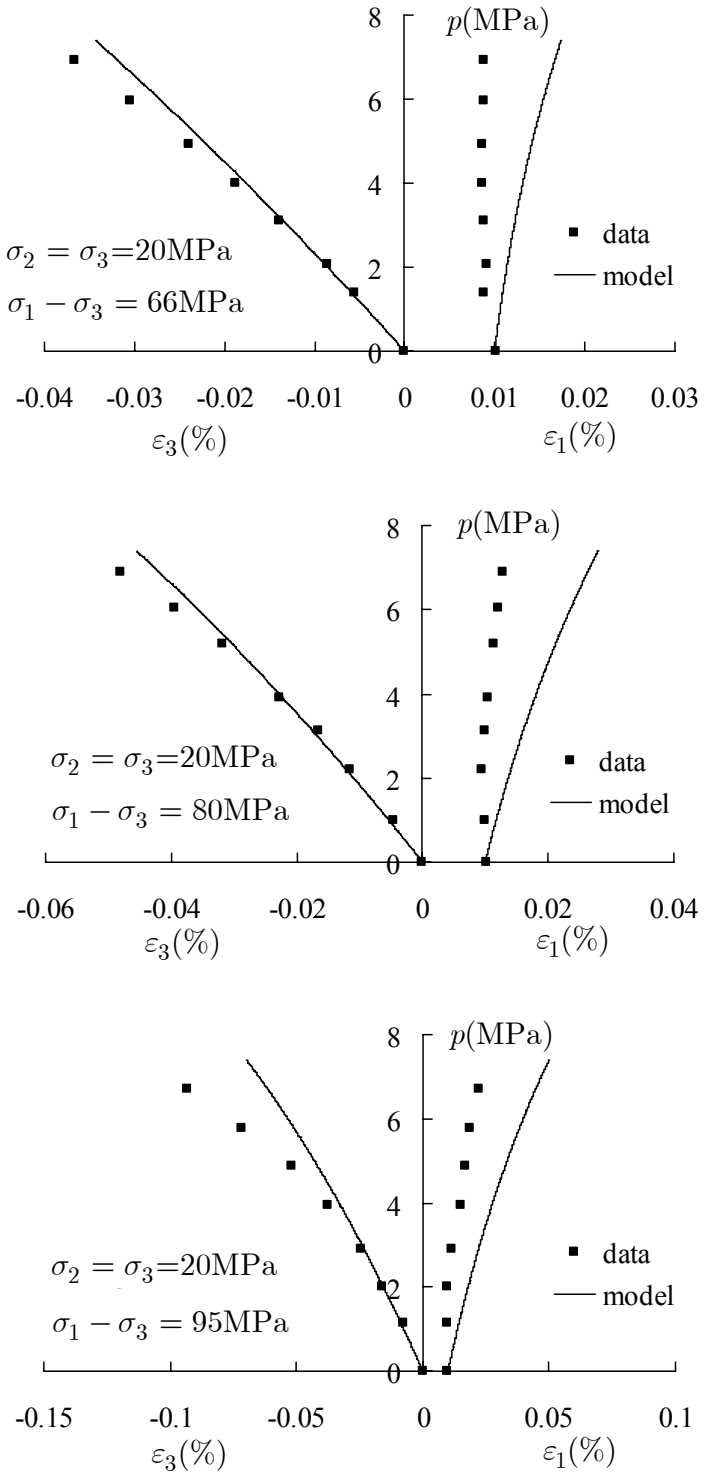

Fig. B.2 *Strain response to pore pressure increment at different deviatoric stress (34, 50, 66, 80 and 95MPa) with confining pressure 20MPa*

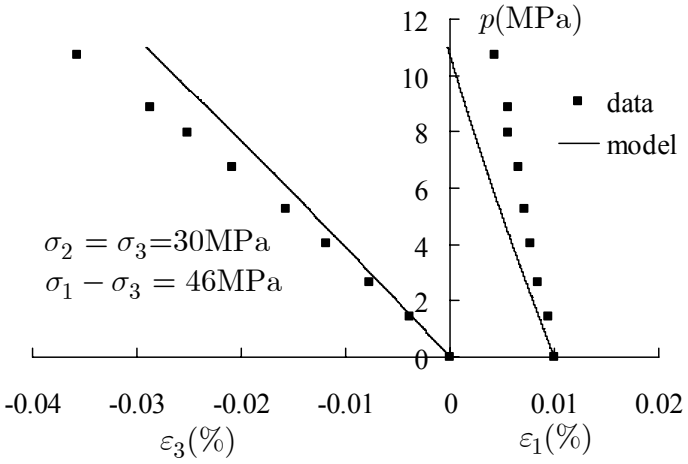

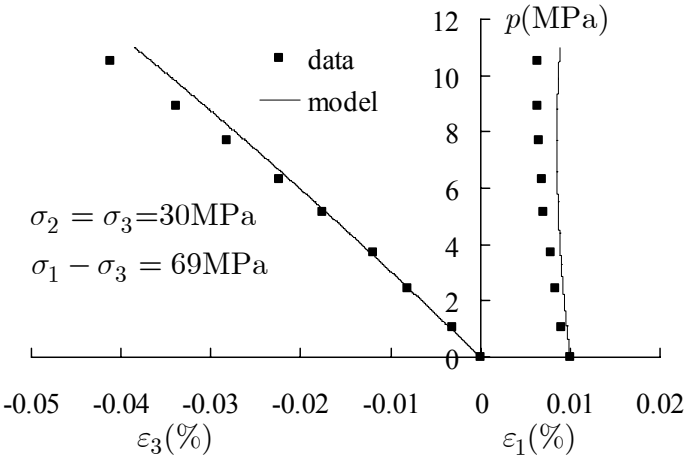

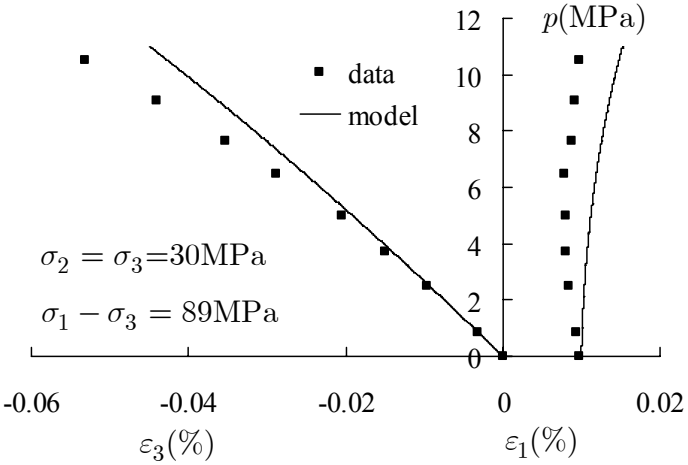

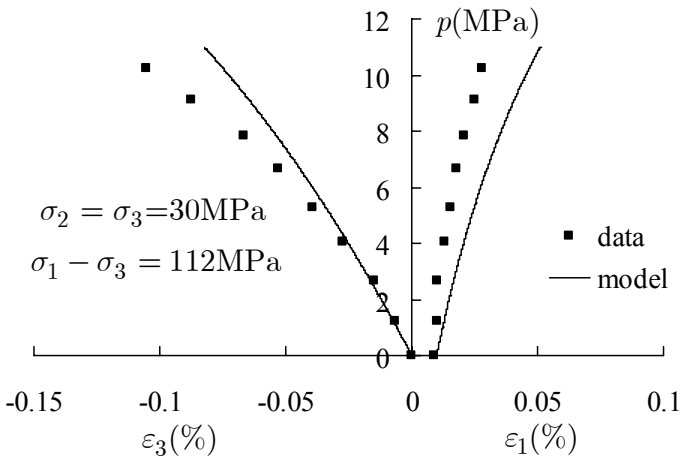

Fig. B.3 *Strain response to pore pressure increment at different deviatoric stress (46, 69, 89 and 112MPa) with confining pressure 30MPa*

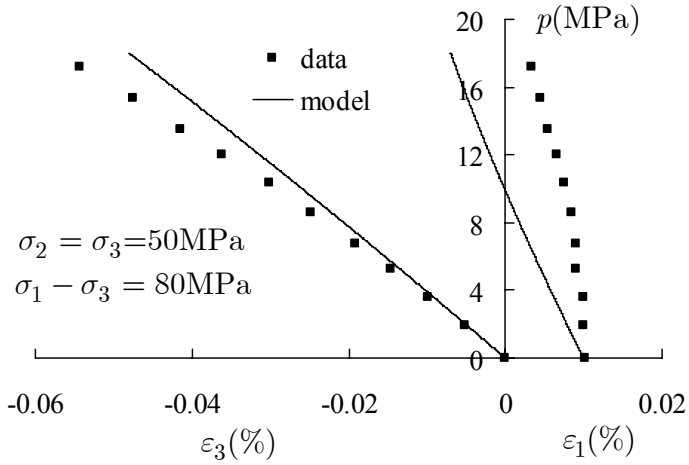

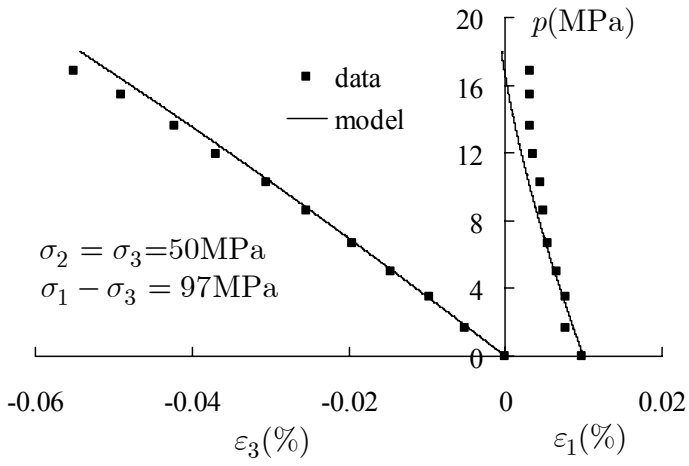

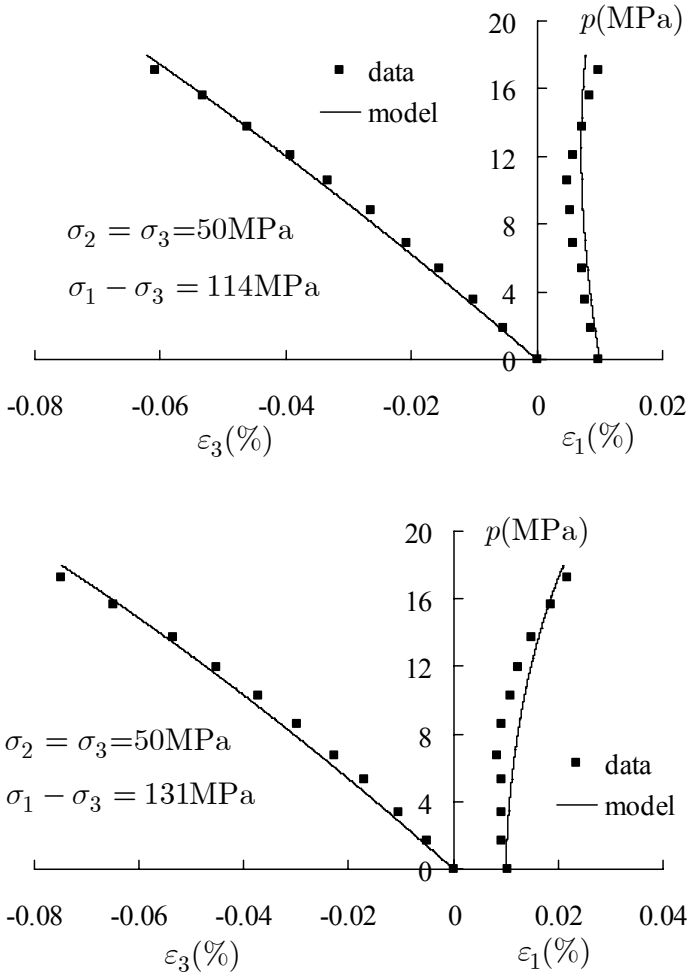

Fig. B.4 *Strain response to pore pressure increment at different deviatoric stress (80, 97, 114 and 131MPa) with confining pressure 40MPa*